Scientific Research

JBiSE

ISSN: 1937-6871

Volume 2 Number 4 August 2009

Journal of Biomedical Science and Engineering

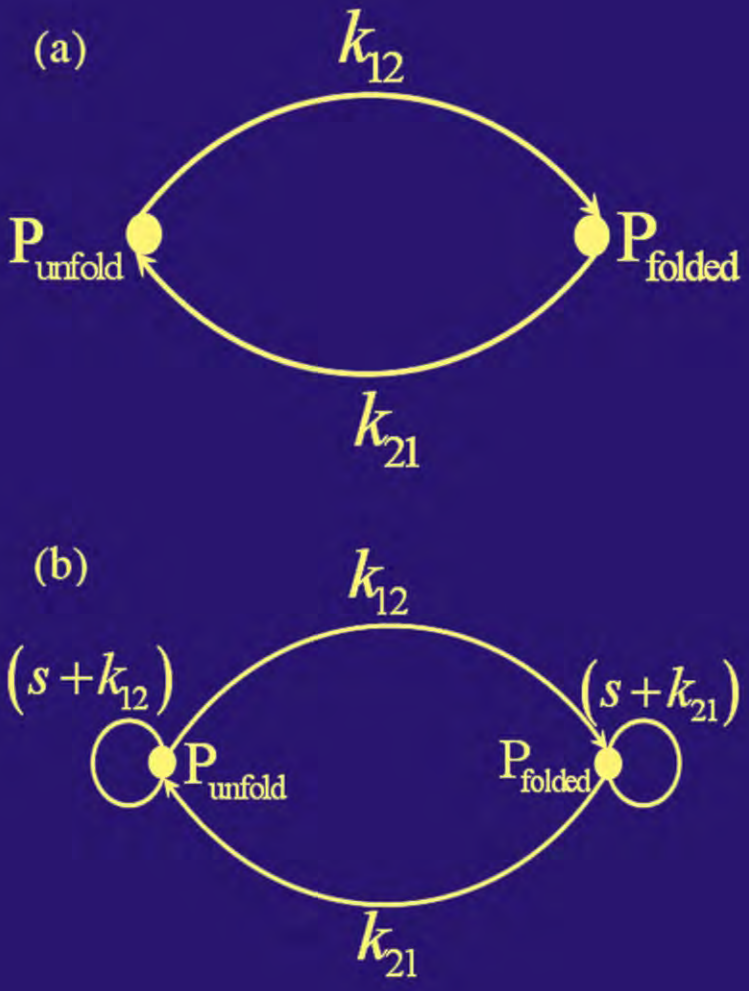

www. scirp. org/journal/jbise

Journal Editorial Board

ISSN 1937-6871 (Print) ISSN 1937-688X (Online)

http://www.scirp.org/journal/jbise

Journal of Biomedical Science and Engineering (JBiSE)
Published Online August 2009 in SciRes (http://www.scirp.org/journal/jbise).

TABLE OF CONTENTS

Volume 2, Number 4, August 2009

The figure on the front cover shows the digraph (panel a) and the phase digraph (panel b) introduced for studying the two-state protein folding mechanism. See the article published in JBiSE, 2009, Vol. 2, No. 3, 136−143. (Courtesy of Kuo-Chen Chou.)

Journal of Biomedical Science and Engineering (JBiSE)

SUBSCRIPTIONS

The ***Journal of Biomedical Science and Engineering*** (Online at Scientific Research Publishing, www.scirp.org) is published monthly by Scientific Research Publishing, Inc., USA.
E-mail: jbise@scirp.org

Subscription Rates: Volume 2 2009

Printed: $50 per copy.

Electronic: freely available at www.scirp.org.

To subscribe, please contact Journals Subscriptions Department at jbise@scirp.org.

Sample Copies: If you are interested in obtaining a free sample copy, please contact Scientific Research Publishing, Inc at jbise@scirp.org.

SERVICES

Advertisements

Contact the Advertisement Sales Department at jbise@scirp.org.

Reprints (a minimum of 100 copies per order)

Contact the Reprints Co-ordinator, Scientific Research Publishing, Inc., USA.
E-mail: jbise@scirp.org

PRODUCTION INFORMATION

For manuscripts that have been accepted for publication, please contact:
E-mail: jbise@scirp.org

News and Announcement

We are pleased to announce that two of the Editorial Board Members of **JBiSE**, Kuo-Chen Chou and Hong-Bin Shen, have been identified by Science Watch (http://sciencewatch.com/ana/fea/09maraprFea/) as the authors with the highest numbers of Hot Papers published over the preceding two years (2007 and 2008). Among the 13 authors listed in the table of **"**Scientists with Multiple Hot Papers" by Science Watch, Professor Dr. Kuo-Chen Chou of Gordon Life Science institute and Shanghai Jiaotong University ranks No.1 with 17 hot papers, and Associated Professor Hong-Bin Shen of Shanghai Jiaotong University ranks No.4 with 13 hot papers.

Meanwhile, the review article by Kuo-Chen Chou and Hong-Bin Shen, entitled "Recent Progresses in Protein Sub-cellular Location Prediction" published in Analytical Biochemistry, has been identified by Science Watch as the New Hot Paper in the field of Biology & Biochemistry (http://sciencewatch.com/dr/nhp/2009/09marnhp/09marnhpChou/).

For more information about the hot research and hot papers, go to visit the web-sites at http://www.sciencenet.cn/htmlnews/2009/3/216833.html; http://sciencewatch.com/ana/fea/pdf/09maraprFea.pdf; and http://sciencewatch.com/dr/nhp/2009/pdf/09marnhpChou.pdf.

Please join us to send our sincere and warm congratulations to our fellow board members, Kuo-Chen Chou and Hong-Bin Shen, for their prominent contributions in science. Meanwhile, we hope this announcement can attract more researchers to submit their best papers to **JBiSE**, the journal that publishes the highest quality of research and review articles in all important aspects of biology, medicine, engineering, and their intersection.

We would also like to take this opportunity to announce that, owing to the large number of manuscripts that we are receiving, **JBiSE** will increase publication frequency from bi-monthly to monthly in 2009.

JBiSE Editorial Office

J. Biomedical Science and Engineering, 2009, 2, 210-215 **JBiSE**
doi: 10.4236/jbise.2009.24034 Published Online August 2009 (http://www.SciRP.org/journal/jbise/).

Changes in cerebral perfusion detected by dynamic susceptibility contrast magnetic resonance imaging: normal volunteers examined during normal breathing and hyperventilation

Ronnie Wirestam[1*], Christian Engvall[2], Erik Ryding[3], Stig Holtås[4], Freddy Ståhlberg[1,4], Peter Reinstrup[2]

[1]Department of Medical Radiation Physics, Lund University, Lund, Sweden; [2]Department of Anaesthesiology & Intensive Care, Lund University Hospital, Lund, Sweden; [3]Department of Clinical Neurophysiology, Lund University Hospital, Lund, Sweden; [4]Department of Diagnostic Radiology, Lund University, Lund, Sweden.
Email: Ronnie.Wirestam@med.lu.se

Received 3 March 2009; revised 2 April 2009; accepted 24 April 2009.

ABSTRACT

Global cerebral perfusion parameters were measured using dynamic susceptibility contrast magnetic resonance imaging (DSC-MRI) in eight healthy volunteers examined during normal breathing and spontaneous hyperventilation. DSC-MRI-based cerebral blood flow (CBF) decreased during hyperventilation in all volunteers (average decrease 29%), and the corresponding global CBF estimates were 73±19ml/(min100g) during normal breathing and 52±7.9ml/(min100g) during hyperventilation (mean ±SD, n=8). Furthermore, the hypocapnic conditions induced by hyperventilation resulted in a prolongation of the global mean transit time (MTT) by on average 14%. The observed CBF estimates appeared to be systematically overestimated, in accordance with previously published DSC-MRI results, but reduced to more reasonable levels when a previously retrieved calibration factor was applied.

Keywords: Magnetic Resonance Imaging; Perfusion; Cerebral Blood Flow; Mean Transit Time; Hypocapnia

1. INTRODUCTION

The use of dynamic susceptibility contrast magnetic resonance imaging (DSC-MRI) for assessment of perfusion-related parameters is promising [1,2], but the concept shows a number of methodological complications. For example, accurate registration of the arterial input function (AIF), i.e. the concentration-versus-time curve in an appropriate tissue-feeding artery, is hampered by arterial signal saturation [3] and local geometrical distortion [4] at peak concentration, as well as by partial-volume effects [5]. Furthermore, the T2* relaxivities of the paramagnetic contrast agent are, most likely, different in arterial and tissue environments, and the non-linear relationship in whole blood between transversal relaxation-rate change ($\Delta R2^*$) and contrast-agent concentration needs to be considered when gradient-echo pulse sequences are used [6]. Attempts to achieve absolute quantification of perfusion parameters by standard DSC-MRI have typically been characterized by overestimated absolute values of cerebral blood volume (CBV) and cerebral blood flow (CBF) [1,3,7,8,9], and these observations are attributed, at least in part, to a correspondingly underestimated arterial concentration time integral. Hence, most existing implementations of DSC-MRI provide perfusion parameters only in relative terms.

Reproducible absolute quantification of CBF is indeed desirable, for example, in the follow-up of tumour or stroke therapy, for determining tissue at risk in acute ischaemic stroke and when a global change in CBF can be expected. The potential of DSC-MRI for absolute or semi-absolute CBF quantification is not yet fully established, and additional information is warranted. Hence, in order to further investigate the usefulness of DSC-MRI for absolute quantification as well as for detection of controlled changes in perfusion, estimates of global CBF and mean transit time (MTT) were acquired in a group of normal volunteers examined during normal breathing and spontaneous hyperventilation. The primary aim of this study was to test the capability of DSC-MRI to detect and quantify changes in global cerebral perfusion caused by spontaneous hyperventilation.

2. METHODS

2.1. Subjects and Experimental Procedure

Eight healthy volunteers (mean age 33 years) were in-

*Corresponding author.

cluded in the study (**Table 1**). Each subject was examined by DSC-MRI during normal breathing and hyperventilation on different occasions. The time interval between the two DSC-MRI experiments ranged from 3 to 35 days (mean time interval 16.4 days), and every second subject started with the normocapnic conditions. Hypocapnia was induced by spontaneous hyperventilation under external guidance. During the DSC-MRI experiments, end-tidal pCO_2 ($ETCO_2$) was monitored and the subjects were at rest in the supine position, breathing normal air with addition of extra O_2 to a total level of 50%, with their eyes open and supplied with earplugs.

The study was approved by the local ethics committee, and written informed consent was obtained from each volunteer.

2.2. DSC-MRI Experiment

DSC-MRI was performed using a 1.5 T MRI whole-body unit (Siemens Magnetom Vision, Siemens Medical Systems, Erlangen, Germany). At each DSC-MRI experiment, the subject received 0.2 mmol/kg bodyweight of a gadobutrol MRI contrast agent (Gadovist 1.0, Schering AG, Germany), administered into a peripheral arm vein at an injection rate of 3 ml/s and followed by a saline flush.

The first passage of the contrast-agent bolus through the brain was tracked using dynamic gradient-echo echo-planar imaging (GRE-EPI) during approximately 75 s at a temporal resolution of 1.65 s. Ten slices with a slice thickness of 8 mm were recorded and the imaging parameters were as follows: Echo time 54ms, matrix size 128×128 and field of view 250×250 mm^2.

2.3. Post-Processing and Data Analysis

Estimates of CBF in ml/(min100g) were calculated according to (1):

$$CBF = k_H \frac{\int_0^\infty C(t)dt \cdot \max[R(t)]}{\int_0^\infty C_{artery}(t)dt \cdot \int_0^\infty R(t)dt} \quad (1)$$

The tracer concentrations in tissue (C) and in artery (C_{artery}) were calculated (in arbitrary units) using the relationship $C(t) \propto -\ln[S(t)/S_0]$, where S(t) is the signal at time t and S_0 is the baseline signal observed before arrival of the contrast-agent bolus [1,2]. The constant $k_H = (1-H_{large})/[\rho(1-H_{small})]$ was set to 0.705 ml/g in the present study [1]. H_{large} and H_{small} are the haematocrit values in large and small vessels, respectively, and ρ is the brain density. R(t) is the tissue residue function, obtained by deconvolution of the measured tissue concentration time curve with the AIF, and max [R(t)] is the peak value of this function. Deconvolution was performed using a singular value decomposition algorithm.

The area under the AIF curve, i.e. the time integral of the arterial concentration $C_{artery}(t)$, was determined from the same arterial locations in both the normal and the hyperventilation case. A correction for the combined consequences of partial-volume effects, arterial signal saturation and signal displacement (due to local geometrical distortion) at peak concentration was applied. The employed correction resembled the approach described by Knutsson *et al.* [9], although in the present study a large brain-feeding artery (the internal carotid artery), rather than the superior sagittal sinus, was used for the AIF time-integral rescaling.

The rescaling procedure was based on the combined concentration-versus-time information from the large brain-feeding artery (showing distorted curve shape at peak concentration due to partial-volume effects, signal saturation and/or local geometric distortions) and a smaller artery used as the AIF in the deconvolution procedure (assumed to show a reasonable curve shape but suffering from an underestimated area under curve). The concentration curve from the smaller artery (in practice obtained from pixels very close to the middle cerebral artery or its branches) was rescaled, with retained shape, to fit the flanks and baseline of the distorted curve from the large artery. The time integral of the rescaled small-artery curve was used in (1) as an approximation to the true concentration time integral of the large

Table 1. Volunteer data (sex, age, $ETCO_2$ levels) and observed whole-brain average DSC-MRI CBF estimates.

Volunteer no.	Sex	Age [years]	$ETCO_2$ [kPa]		CBF [ml/(min 100g)]	
			Normocapnia	Hypocapnia	Normocapnia	Hypocapnia
1	M	40	6.0	4.6	106	49.0
2	M	39	5.6	4.1	79.7	61.8
3	M	35	5.0	3.7	70.1	53.6
4	M	31	5.7	2.7	84.1	61.9
5	M	31	5.8	3.1	63.0	48.1
6	M	30	5.8	4.4	52.4	46.6
7	M	30	5.6	4.0	84	58.1
8	M	29	5.3	3.6	47.5	39.9

brain-feeding artery.

The retrieval of R(t) by deconvolution also allows for calculation of the mean transit time using Zierler's area-to-height relationship [1,10,11]:

$$MTT = \frac{\int_0^\infty R(t)dt}{\max[R(t)]} \quad (2)$$

Parametric CBF and MTT maps were calculated, in absolute terms, using (1) and (2), respectively. For CBF as well as MTT, whole-brain average estimates were calculated as the mean of all brain-tissue voxel values in the 10 slices obtained by DSC-MRI. Large-vessel contributions were eliminated by excluding all pixels with values exceeding 2.5 times the average CBF value of the entire volume [12]. Spurious MTT values were similarly removed by excluding a small number of pixels with values below 0.2 times the mean MTT value and above 2.5 times the mean MTT value of the entire volume.

2.4. Statistical Analysis

A Wilcoxon matched-pairs signed-ranks test was applied to determine whether or not the $ETCO_2$, CBF and MTT values observed during normal breathing were significantly different from those observed during hyperventilation. The CBF-versus-$ETCO_2$ and MTT-versus-$ETCO_2$ relationships were evaluated by linear-regression analyses.

3. RESULTS

In all 8 volunteers, the DSC-MRI-based CBF estimates decreased when the subject was hyperventilating (**Table 1** & **Figure 1a**), and the mean CBF decrease during hyperventilation was 29%. Similarly, in all 8 subjects a longer MTT was observed during hyperventilation (**Figure 1b**), with a mean MTT increase of 14%.

Average whole-brain CBF and MTT estimates at normocapnic and hypocapnic conditions, together with the corresponding $ETCO_2$ levels, are given in **Table 2** (mean ±SD, n=8). The statistical analysis showed that $ETCO_2$ levels as well as CBF and MTT estimates differed significantly between normal-breathing conditions and hyperventilation ($p<0.01$).

The obtained relationship between CBF and $ETCO_2$ is displayed in **Figure 2**, indicating that CBF increased with $ETCO_2$. **Figure 3** shows MTT versus $ETCO_2$ and the trendline suggests a slight decrease in MTT when $ETCO_2$ increases. The significant prolongation of MTT observed during hyperventilation implies, according to the central volume theorem (MTT=CBV/CBF), that the relative decrease in CBF, induced by hyperventilation, was larger than the corresponding relative decrease in CBV.

4. DISCUSSION

It is indeed encouraging that the expected decrease in CBF during hyperventilation could be detected in all of the volunteers. Analysis of the results from the whole population showed that the CBF estimates obtained during hyperventilation were significantly different from those seen during normal breathing conditions ($p<0.01$), and the observed average CBF decrease of 29% is in quite reasonable agreement with previous studies [13,14]. The observed CO_2 reactivity of CBF during hypocapnia, corresponding to approximately 2.1% of reduction in global CBF per mmHg change in $ETCO_2$, is not at all unreasonable, and the current estimate is in excellent agreement with previous findings by Fortune *et al.* [13] and Reinstrup *et al.* [15]. Other investigators have observed a somewhat higher CO_2 reactivity [e.g. 14,16], corresponding to approximately 3% reduction in CBF per mmHg change in $ETCO_2$, but the characteristics of previously investigated populations may have differed with regard to, for example, sex, age and state of health, and some previous studies were limited to grey matter.

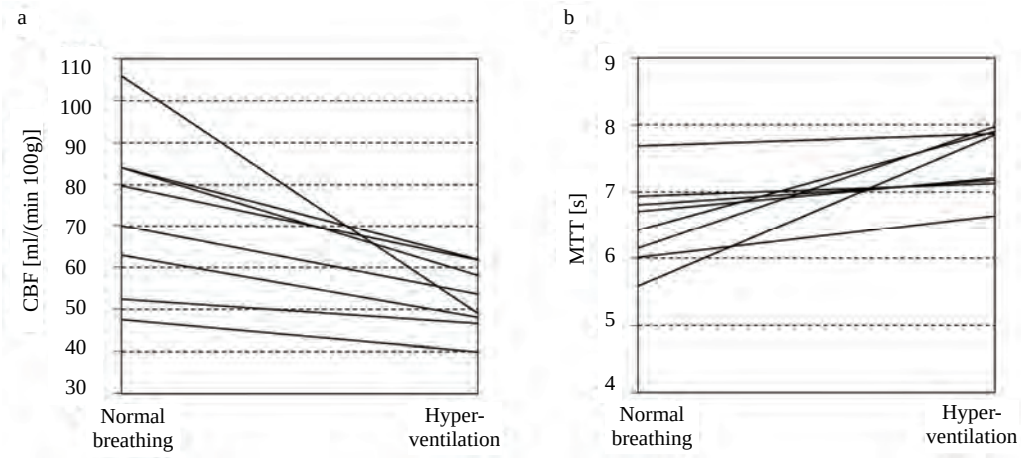

Figure 1. Individual estimates of (a) cerebral blood flow (CBF) and (b) mean transit time (MTT), measured by DSC-MRI in eight normal male subjects during normal breathing and hyperventilation.

Table 2. Whole-brain average DSC-MRI CBF and MTT estimates and the corresponding $ETCO_2$ levels during normal breathing and hyperventilation (mean±SD, n=8).

	$ETCO_2$ [kPa]	CBF [ml/(min 100g)]	MTT[s]
Normal breathing	5.6 ± 0.32	73 ± 19	6.5 ± 0.65
Hyperventilation	3.8 ± 0.64	52 ± 7.9	7.5 ± 0.49
Relative change[%]	-33	-29	+14
Wilcoxon test p-value	0.008	0.008	0.008

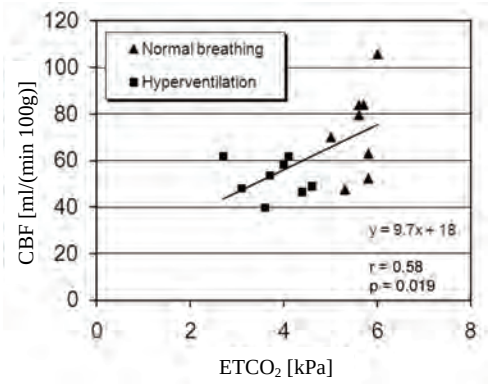

Figure 2. Estimates of cerebral blood flow (CBF) obtained during normal breathing and hyperventilation as a function of end-tidal pCO_2 ($ETCO_2$).

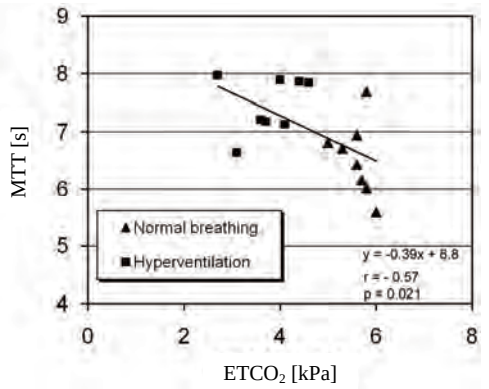

Figure 3. Estimates of mean transit time (MTT) obtained during normal breathing and hyperventilation as a function of end-tidal pCO_2 ($ETCO_2$).

The observed prolongation of the MTT during hyperventilation is related to a decreased vascular blood velocity during hypocapnia [14], and this effect manifests itself as a well-documented smaller relative decrease in CBV than in CBF during the hypocapnic conditions induced by hyperventilation [13,14]. Ito *et al.* [17] addressed this topic by investigating the relative importance of the arterial, capillary and venous blood-volume fractions in hypocapnia. The authors concluded that changes in human CBV during hypocapnia are caused by changes in the arterial blood-volume component without changes in the venous and capillary blood volume [17].

The absolute global CBF values obtained from the present experiments were somewhat high, in accordance with previous experimental DSC-MRI investigations [1,3,7,8,9] and theoretical predictions [6]. Partial-volume effects and local geometric distortions at peak concentration [3,4] can be problematic, but these effects were most likely reduced by the applied correction of the arterial concentration time integral. Hence, the remaining CBF overestimation is probably related to the fundamental problem with DSC-MRI in that the response to a given contrast-agent concentration differs between large vessels and the capillary environment [6]. In spite of the applied AIF-area correction, accurate determination of $C_{artery}(t)$ and the associated time integral was difficult in some cases, and the relatively large standard deviations (SDs) seen in the DSC-MRI results might be a reflection of this difficulty. Identification of an appropriate AIF location is another crucial issue in CBF and MTT quantification. It has recently been established that the desired linear relationship between $\Delta R2^*$ and contrast-agent concentration in arteries can indeed be obtained by careful selection of the AIF from pixels not completely located inside the vessel [18]. In the present study, we were aware of the AIF-selection guidelines provided by Bleeker *et al.* for single-shot EPI [18], and tried, as far as possible, to consider them in the AIF identification procedure.

Even if DSC-MRI turns out to provide inherently overestimated CBF estimates they may still be useful, provided that DSC-MRI results consistently can be shown to exhibit a high degree of linear correlation with a reference CBF technique, for example, Xe-133 SPECT [9] or positron emission tomography (PET) [7]. The possibility to rescale DSC-MRI-based perfusion estimates by application of an appropriate calibration factor, based on such comparative studies, has been suggested, although it has been pointed out that the retrieval of a universal conversion factor, applicable to a variety of DSC-MRI implementations, may be challenging [7].

A CBV calibration factor, applicable to the current DSC-MRI setup, has previously been obtained, in the same group of volunteers as examined in the present study, using SPECT imaging of Tc-99m-labelled erythrocytes as a reference CBV method [19]. This calibration factor can theoretically be used also to appropriately correct corresponding DSC-MRI-based CBF values, since CBF=CBV/MTT (according to the central volume theorem), provided that MTT values can be correctly estimated. The global MTT estimates observed in the present study (mean value 6.5 s at normoventilation)

were quite reasonable, and in accordance with previously published PET results from normal subjects. For example, Kaneko *et al*. [20] observed MTT values of 6.1 s in grey matter and 8.1 s in white matter, and the large study by Leenders *et al*. [21] showed CBV-to-CBF ratios of 5.7 s in insular grey matter and 7.3 s in white matter. Application of the calibration factor to the present data resulted in a corrected whole-brain average CBF of approximately 42 ml/(min100g). Literature values of normal global CBF in humans at rest vary over a considerable range [22,23], but are typically between 40 and 50ml/(min100g) for the adult population. For example, Knutsson *et al*. [9] obtained a whole-brain average CBF of 40ml/(min100g) (in elderly normal subjects) by Xe-133 SPECT, Slosman *et al*. [24] observed a global CBF of 43ml/(min100g) in male volunteers (age interval 29-38 years), also by use of Xe-133 SPECT, Dörfler *et al*. [22] reported a global CBF estimate of 48ml/(min100g) based on extracranial sonography and Matthew *et al*. [25] observed 40 ml/(min100g) using $H_2{}^{15}O$ PET. Finally, Yonas *et al*. [26] employed stable xenon computed tomography (Xe-CT) and extracted regional CBF values of 92ml/(min100g) in the highest-flow compartments, 54ml/(min 100g) in mixed-cortical regions (calculated from linear-regression equations and corresponding to the age of 33 years) and an age-independent white-matter regional CBF of 20ml/(min100g).

In conclusion, DSC-MRI showed promising results in the detection of controlled perfusion changes, induced by spontaneous hyperventilation, in individual subjects. In accordance with previously reported DSC-MRI experiments, uncorrected absolute CBF values appeared to be overestimated.

5. ACKNOWLEDGEMENTS

This study was supported by the Swedish Research Council (project no. 13514), the Swedish Cancer Society and the Crafoord Foundation, Lund.

REFERENCES

[1] K. A. Rempp, G. Brix, F. Wenz, C. R. Becker , F. Gückel, and W. J. Lorenz, (1994) Quantification of regional cerebral blood flow and volume with dynamic susceptibility contrast-enhanced MR imaging, Radiology, **193**, 637−641.

[2] L. Østergaard, R. M. Weisskoff, D. A. Chesler, C. Gyldensted, and B. R. Rosen, (1996) High resolution measurement of cerebral blood flow using intravascular tracer bolus passages, Part I: Mathematical Approach and Statistical Analysis, Magnetic Resonance in Medicine, **36**, 715−725.

[3] R. Ellinger, C. Kremser, M. F. Schocke, C. Kolbitsch, J. Griebel, S. R. Felber, and F. T.Aichner, (2000) The impact of peak saturation of the arterial input function on quantitative evaluation of dynamic susceptibility contrast-enhanced MR studies, Journal of Computer Assisted Tomography, **24**, 942−948.

[4] M. Rausch, K. Scheffler, M. Rudin, and E. W. Radu, (2000) Analysis of input functions from different arterial branches with gamma variate functions and cluster analysis for quantitative blood volume measurements, Magnetic Resonance Imaging, **18**, 1235−1243.

[5] J. J. Chen, M. R. Smith, and R. Frayne, (2005) The impact of partial-volume effects in dynamic susceptibility contrast magnetic resonance perfusion imaging, Journal of Magnetic Resonance Imaging, **22**, 390−399.

[6] B. F. Kjølby, L. Østergaard, and V. G. Kiselev, (2006) Theoretical model of intravascular paramagnetic tracers effect on tissue relaxation, Magnetic Resonance in Medicine, **56**, 187−197.

[7] C. B. Grandin, A. Bol, A. M. Smith, C. Michel, and G. Cosnard, (2005) Absolute CBF and CBV measurements by MRI bolus tracking before and after acetazolamide challenge: Repeatability and comparison with PET in humans, NeuroImage, **26**, 525−535.

[8] K. E. Sakaie, W. Shin, K. R. Curtin, R. M. McCarthy, T. A. Cashen, T. J. and Carroll, (2005) Method for improving the accuracy of quantitative cerebral perfusion imaging, Journal of Magnetic Resonance Imaging, **21**, 512−519.

[9] L. Knutsson, S. Börjesson, E. M. Larsson, J. Risberg, L. Gustafson, U. Passant, F. Ståhlberg, and R. Wirestam, (2007) Absolute quantification of cerebral blood flow in normal volunteers: Correlation between Xe-133 SPECT and dynamic susceptibility contrast MRI, Journal of Magnetic Resonance Imaging, **26**, 913−920.

[10] P. Meier and K. L. Zierler, (1954) On the theory of indicator-dilution method for measurement of blood flow and volume, Journal of Applied Physiology, **6**, 731−744.

[11] K. L. Zierler, (1965) Equations for measuring blood flow by external monitoring of radioisotopes, Circulation Research, **16**, 309−321.

[12] T. Ernst, L. Chang, L. Itti, and O. Speck, (1999) Correlation of regional cerebral blood flow from perfusion MRI and SPECT in normal subjects, Magnetic Resonance Imaging, **17**, 349–354.

[13] J. B. Fortune, P. J. Feustel, C. deLuna, L. Graca, J. Hasselbarth, and A. M. Kupinski, (1995) Cerebral blood flow and blood volume in response to O_2 and CO_2 changes in normal humans, Journal of Trauma, **39**, 463−472.

[14] H. Ito, I. Kanno, M. Ibaraki, J. Hatazawa, and S. Miura, (2003) Changes in human cerebral blood flow and cerebral blood volume during hypercapnia and hypocapnia measured by positron emission tomography, Journal of Cerebral Blood Flow and Metabolism, **23**, 665−670.

[15] P. Reinstrup, E. Ryding, L. Algotsson, L. Berntman, and T. Uski, (1994) Effects of nitrous oxide on human regional cerebral blood flow and isolated pial arteries, Anesthesiology, **81**, 396–402.

[16] W. D. Obrist, T. W. Langfitt, J. L. Jaggi, J. Cruz, and T. A. Gennarelli, (1984) Cerebral blood flow and metabolism in comatose patients with acute head injury. Relationship to intracranial hypertension, Journal of Neurosurgery, **61**, 241−253.

[17] H. Ito, M. Ibaraki, I. Kanno, H. Fukuda, and S. Miura, (2005) Changes in the arterial fraction of human cerebral blood volume during hypercapnia and hypocapnia

measured by positron emission tomography, Journal of Cerebral Blood Flow and Metabolism, **25**, 852−857.

[18] E. J. W. Bleeker, M. A. van Buchem, and M. J. P. van Osch, (2009) Optimal location for arterial input function measurements near the middle cerebral artery in first-pass perfusion MRI, Journal of Cerebral Blood Flow and Metabolism, **29**, 840−852.

[19] C. Engvall, E. Ryding, R. Wirestam, S. Holtås, K. Ljunggren, T. Ohlsson, and P. Reinstrup, (2008) Human cerebral blood volume (CBV) measured by dynamic susceptibility contrast MRI and ^{99m}Tc-RBC SPECT, Journal of Neurosurgical Anesthesiology, **20**, 41–44.

[20] K. Kaneko, Y. Kuwabara, F. Mihara, T. Yoshiura, M. Nakagawa, A. Tanaka, M. Sasaki, H. Koga, K. Hayashi, and H. Honda, (2004) Validation of the CBF, CBV, and MTT values by perfusion MRI in chronic occlusive cerebrovascular disease: A comparison with ^{15}O-PET, Academic Radiology, 11, 489−497.

[21] K. L. Leenders, D. Perani, A. A. Lammertsma, J. D. Heather, P. Buckingham, M. J. Healy, J. M. Gibbs, R. J. Wise, J. Hatazawa, S. Herold, R. P. Beaney, D. J. Brooks, T. Spinks, C. Rhodes, R. S. Frackowiak, and T. Jones, (1990) Cerebral blood flow, blood volume and oxygen utilization: Normal values and effect of age, Brain, **113**, 27−47.

[22] P. Dörfler, I. Puls, M. Schliesser, M. Mäurer, and G. Becker, (2000) Measurement of cerebral blood flow volume by extracranial sonography, Journal of Cerebral Blood Flow and Metabolism, **20**, 269−271.

[23] N. A. Lassen, (1985) Normal average value of CBF in young adults is 50ml100 g^{-1} min^{-1}, Journal of Cerebral Blood Flow and Metabolism [Editorial], **5**, 347−349.

[24] D. O. Slosman, C. Chicherio, C. Ludwig, L. Genton, S. de Ribaupierre, D. Hans, C. Pichard, E. Mayer, J. M. Annoni, and A. de Ribaupierre, (2001) ^{133}Xe SPECT cerebral blood flow study in a healthy population: Determination of T-scores, Journal of Nuclear Medicine, **42**, 864−870.

[25] E. Matthew, P. Andreason, R. E. Carson, P. Herscovitch, K. Pettigrew, R. Cohen, C. King, C. E. Johanson, and S. M. Paul, (1993) Reproducibility of resting cerebral blood flow measurements with $H_2{}^{15}O$ positron emission tomography in humans, Journal of Cerebral Blood Flow and Metabolism, **13**, 748−754.

[26] H. Yonas, J. M. Darby, E. C. Marks, S. R. Durham, and C. Maxwell, (1991) CBF measured by Xe-CT: Approach to analysis and normal values, Journal of Cerebral Blood Flow and Metabolism, **11**, 716−725.

J. Biomedical Science and Engineering, 2009, 2, 216-226 **JBiSE**
doi: 10.4236/jbise.2009.24035 Published Online August 2009 (http://www.SciRP.org/journal/jbise/).

Effects of extracellular matrix proteins on expansion, proliferation and insulin-producing-cell differentiation of ARIP cells

Gary G. Adams[1], Yu-Xin Cui[2]

[1]Insulin Diabetes Experimental Research Group (IDER), Faculty of Medicine and Health Science, University of Nottingham, Clifton Boulevard, Nottingham, NG7 2UH UK; [2]Department of Physiology, Development and Neuroscience, University of Cambridge, Downing Street, Cambridge, CB2 3EG, UK.
Email: Gary.Adams@nottingham.ac.uk

Received 17 April 2009; revised 25 April 2009; accepted 30 April 2009.

ABSTRACT

Regeneration of transplantable pancreatic islet cells has been considered to be a promising alternative therapy for type 1 diabetes. Research has suggested that adult pancreatic stem and progenitor cells can be derived into insulin-producing cells or cultivated islet-like clusters given appropriate stimulating conditions. In this study we explored the effect of selective extracellular matrix (ECM) proteins on the potential of insulin-producing cell differentiation using ARIP cells, an adult rat pancreatic ductal epithelial cell line, as a model *in vitro*. Quantitative single cell morphology analysis indicated that all the four ECM proteins we have used (type I collagen, laminin, fibronectin and vitronectin) increased the single cell area and diameter of ARIP cells. In addition, serum-free cell cultivation was dependent on cell density and particular components; and serum could be replaced when systematic optimisation could be performed. Surface treated with laminin was shown to be able to enhance overall cell expansion in the presence of defined serum-free medium conditions. Collagen treated surfaces enhanced insulin production in the presence of GLP-1 although the insulin gene expression was however weak accordingly. Our results suggest that selective ECM proteins have effects on single cell morphology, adhesion and proliferation of ARIP cells. These ECM molecules however do not have a potent effect on the insulin-producing cell differentiation potential of ARIP cells even combining with GLP-1.

Keywords: Extracellular Matrix; Proliferation; Differentiation; ARIP Cells; Incretin GLP-1

1. INTRODUCTION

The pluripotent cells that develop into pancreatic β-cells are initially derived from pancreatic ductal epithelium. Ductal cell proliferation is subsequently followed by the budding of endocrine cells but little is known about the intrinsic and extrinsic factors which surround differentiation.

Although a number of studies have been carried out to discover the factors that may be responsible for β-cell proliferation and differentiation, no conclusive evidence is forthcoming [2,34,35,40,45]. Some of the known contributory factors reported to be involved in β-cell acquisition *in vitro,* include islet neogenesis- associated protein (INGAP), nicotinamide, retinoic acid, glycogen like-peptide (GLP-1) and the pancreatic regenerating gene (Reg) [6, 8,25, 29,30,33,41,43].

ARIP cells, an adult rat pancreatic ductal epithelial cell line, are derived from an azaserine induced rat non-tumourigenic pancreatic carcinoma [17]. ARIP cells express ductal cell markers and carbonic anhydrase under basal cultivation conditions. GLP-1, a peptide which is originally produced from small intestine, has been demonstrated to induce the insulin-producing cell differentiation of ARIP cells; and this effect may be accompanied by the overexpression of PDX-1, a transcription factor which is crucial for pancreatic embryogenesis and insulin secretion [15]. Thus, it can be speculated that ARIP cell is a useful in vitro model with which to study the mechanism of the insulin-producing cell regeneration/neogenesis mediated by corresponding stimuli. On the other hand, cell-ECM and cell-cell interaction is believed an important cellular process in regulating cellular proliferation and differentiation. Particularly, extracellular matrix (ECM) and soluble factors may be involved in the facilitation or induction of cell differentiation, although the exact signalling pathway is not well known [17,19,26]. For instance, a previous study has proved that omitting serum is essential for insulin-producing

cell differentiation, as medium containing serum is found to decrease insulin production and inhibit cyst development, whilst, a Matrigel™ overlay procedure is found to be vital to encourage the formation of three-dimensional structure from primarily isolated pancreatic ductal cells [13]. It is suggested that ECM adhesion molecules reorganize cytoskeletal architecture and mediate expression of genes responsible for cell differentiation regulation by binding with specific cell surface integrins, and triggering certain downstream signal transduction, [9,20]. Within the pancreas, integrin distribution is distinctive on the surfaces of different pancreatic cell types. Thus, by manipulating the interaction of ECM integrin, it may provide a promising approach to inducing insulin-producing cell differentiation. Laminin is found, for example, to promote β-cell differentiation during cell cultivation [18].

We hypothesised, therefore, that in the presence of certain serum-free media conditions and ECM proteins, ARIP cells could provide an appropriate model for pancreatic insulin-producing differentiation. Herein, we report the use of ARIP cells to explore the possibility of insulin-producing cell acquisition in vitro. Single cell cytogeometry analysis was carried out to find out whether major ECM proteins are capable of modulating ARIP cell morphology in the first instance. Subsequently, ATP-luciferase based assay was performed to see if cell proliferation is dependent on seeding density and particular serum-free media components, when compared with medium containing foetal calf serum (FCS). Surface coverage of ARIP cells was estimated to determine the potential effect of ECM-protein-coated surfaces in the presence of defined serum-free medium. ARIP cells were eventually encouraged to differentiate into insulin-producing cells given ECM proteins, GLP-1 and serum-free medium conditions.

2. MATERIALS AND METHOD

2.1. Reagents

All chemical reagents and media components were obtained from Sigma (UK) unless mentioned otherwise.

2.2. Tissue Culture

ARIP cells were obtained from ATCC (USA) and maintained in F12K medium supplemented with 10% FCS, 100 μg/ml streptomycin and 100 units/ml penicillin at 37 ˚C in a humidified, 5% CO2 atmosphere. For experimental use, ARIP cells were passaged from tissue culture flasks using a 0.25% trypsin/0.02% EDTA solution. In order to determine the optimal serum-free tissue culture conditions, F12K medium was supplemented with 1 g/L ITS supplement (containing 5 mg/L insulin + 5 mg/L transferrin + 5 mg/L selenium), 2 g/L BSA, 10 mM nicotinamide, 10ng/ml keratinocyte growth factor (KGF) and 10nM Glucagon-Like Peptide-1 (GLP-1) together or separately.

2.3. Surface Coating and Cell Treatment

Multiwell plates with tissue culture (TC) surface (Nunc, Denmark) were coated with Collagen Type I (CN. Upstate, USA), Fibronectin (FN), Laminin (LN) and Vitronectin (VN) respectively according to product instructions. The concentrations of the four ECM proteins were 0.1 μg/cm^2, 1 μg/cm^2 and 10μg/cm^2 (not for VN) respectively. Following surface treatment, plates were washed for 5 min in PBS and blocked with 1% bovine serum albumin (BSA) in PBS for 1 h at 37°C. ARIP cells with 80% confluence were disattached with trypsin/EDTA and resuspended in F12K containing 10% FCS. Cells were spun down at 250 xg for 5 min and resuspended in serum-free F12K. Cells were seeded at a density of 3000 cells/cm^2 and cultured for 6 hours at 37°C in a humidified, 5% CO2 atmosphere.

2.4. Single Cell Morphology Analysis

The cultured cells were stained with 2uM Calcein AM (Invitrogen, UK), a membranepermeant fluorescence viable cell indicator, for 45 minutes at room temperature. Images were captured from 4 random areas surrounding each centre of a well using an inverted fluorescent Leica DM IRB microscope at X200 magnification.

Fluorescence images were subsequently analysed using a highly standardised macro program language, QUIPS written in the Leica Qwin imaging software ((Leica, Bensheim, Germany). Briefly, the image analysis program was delicately designed to identify half maximal colour intensity so as to recognise the body of the single cell but not any background automatically. The intensity threshold was manually altered to reach the cell membrane. A binary editing function enabled the manual removal of artefacts that may have contributed to a false measurement. Once the area of choice had been accepted, single cell features (e.g. area, perimeter, number and roundness) were measured simultaneously according to the calibration of microscopic lens.

2.5. ATP Luminescence Assay

The determination of cell proliferation was carried out on the basis of a luminometric ATP measurement by means of the ATPlite™-M Luminescence Assay System (PerkinElmer, USA) according to the manufacturer's instruction. Luminescence was measured using a LUCY 1 luminometer (Anthos Labtech Instruments, Austria). Standard curves for individual culture of mammalian cell number were performed to confirm both linearity and sensitivity of the method.

2.6. Surface Coverage Measurement

Similar to the surface coating procedures described above, multiwell plates with tissue culture surface was

coated with CN (10μg/cm^2), LN (10μg/cm^2), CN 50%+ LN 50%, Matrigel matrix (BD Biosciences, UK), Poly L-Lysine (PLL; 0.01% solution), PLL followed by CN, PLL followed by LN, PLL followed by CN 50%+ LN 50%, PLL followed by Matrigel, respectively. ARIP cells at a concentration of 2.5X104 cells/cm^2 were cultured on the above surfaces with F12K medium containing 10% FCS for 4 hours, and sequentially with Serum-free F12K medium supplemented with 2g/l BSA, 1g/l ITS supplement, 10mM nicotinamide and P/S. Images were captured from the centre region of each well with the magnification of X100. Cell surface coverage analysis was similar to the measurement of single cell morphology mentioned above.

2.7. Measurement of Insulin Content by Enzyme-Linked Immunosorbent Assay (ELISA)

Cultured cells were washed three times for 10 min each in prewarmed fresh Krebs-Ringerbicarbonate buffer (KRBB; 115 mM NaCl, 24 mM NaHCO3, 5 mM KCl, 1 mM MgCl2, 2.5 mM CaCl2, 10 mM HEPES, pH 7.4) with 0.1% BSA. Cells were then lysed directly by adding 0.5 ml CelLyticTM-M mammalian cell lysis/ extraction reagent. After incubated for 15 min on a shaker, cell lysate was collected and centrifuged for 15 min at 1200 xg to pellet the cellular debris. Theprotein-containing supernatant was transferred to a chilled test tube and stored at –80°C until being assayed for the presence of insulin using an Ultra Sensitive Rat Insulin ELISA Kit (Crystal Chem Inc, USA) according to the manufacturer's instruction.

2.8. Measurement of Insulin Release Stimulated by Glucose

Cells were washed three times with KRBB buffer. After pre-incubation with fresh KRBB buffer for another 30 minutes at 37 ºC, cells were subjected to 5.5 mM and then 16.7 mM glucose within the KRBB buffer for 1 hour. The amount of insulin released in supernatant was determined by rat insulin ELISA as mentioned above.

2.9. Quantification of Cellular DNA Content

Cultured cells in 96-well plates were washed with PBS and treated with 0.02% SDS in salinesodium citrate buffer at 37°C for 1h. Equal volume of 2μg/ml Hoechst 33258 working solution was added in the above wells. 100 μl of the above mixture was transferred to a fresh 96-well assay plate. Measurement of fluorescence was performed with a plate reader (Dynex technologies, UK) at excitation λ 360 nm and emission λ 460 nm. Deoxyribonucleic acid sodium salt from calf thymus (Sigma, UK) was used as a DNA standard.

2.10. Data Analysis

The differences at various time points and experimental conditions were analysed by one-way ANOVA at 95% significance level for multiple comparisons using SPSS 11.5 (SPSS Inc., USA).

3. RESULTS

3.1. Single Cell Morphology on ECM Protein-Coated Surfaces

The first step in this research was to establish that the chosen blocking agent, 1% BSA, could decrease single cell area and perimeter when coated on to tissue culture treated plastic surfaces. **Figure 1** confirmed the blocking action of BSA. Subsequently, effects of the four ECM protein-coated surfaces at a range of concentrations were compared. These ECM protein-coated surfaces altered both single cell features ($P<0.01$) when compared with BSA-coated surfaces. The treatment effects on both single cell area and single cell perimeter were in the order of CN>FN>LN>VN. For single cell area, among CN groups, there was a significant difference between the coating concentrations of 1 μg/cm^2 and 0.1ug/cm^2 ($P<0.01$); and the single cell area difference between them was approximately 200 μm^2. No difference was found between 10 μg/cm^2 and 1 μg/cm^2 of CN groups. Among FN groups, the three coating concentrations showed similar results. Among LN groups, 10 μg/cm^2 of LN-coated surface resulted in higher single cell area compared with the other two lower concentrations ($P<0.01$); no difference was found between 0.1 ug/cm^2 and 1 ug/cm^2. Among VN groups, the results of 0.1 ug/cm^2 and 1 ug/cm^2 concentrations were similar. The feature of single cell perimeter produced similar patterns of treatment effects on single cell area. When single cell roundness was estimated, surfaces coated with three concentrations of CN increased this feature, and 10 μg/cm^2 of CN-coated surface appeared to induce the highest ($P<0.01$ vs BSA group).

Morphologically, on the four ECM protein-coated surfaces, ARIP cells showed increased cell membrane spreading and cell protuberance (**Figure 2**). It appeared that the effect of CN, FN and LN was stronger than VN when they were used to coat tissue culture polystyrene surface. These results indicated that four types of ECM protein-coated surfaces could expand the morphological structures of single ARIP cell in vitro.

In a follow-up experiment, ARIP cells at a density of 1.5×104 cells/cm^2 were cultured under the equivalent surface-coated conditions described above and in serum-free medium for 96 hours. Results showed that the viability of cells decreased severely, and there were just a few viable cells left surrounded by large amounts of cellular debris (data not shown). It appeared difficult for cells to reach confluence. As a control, cells in medium

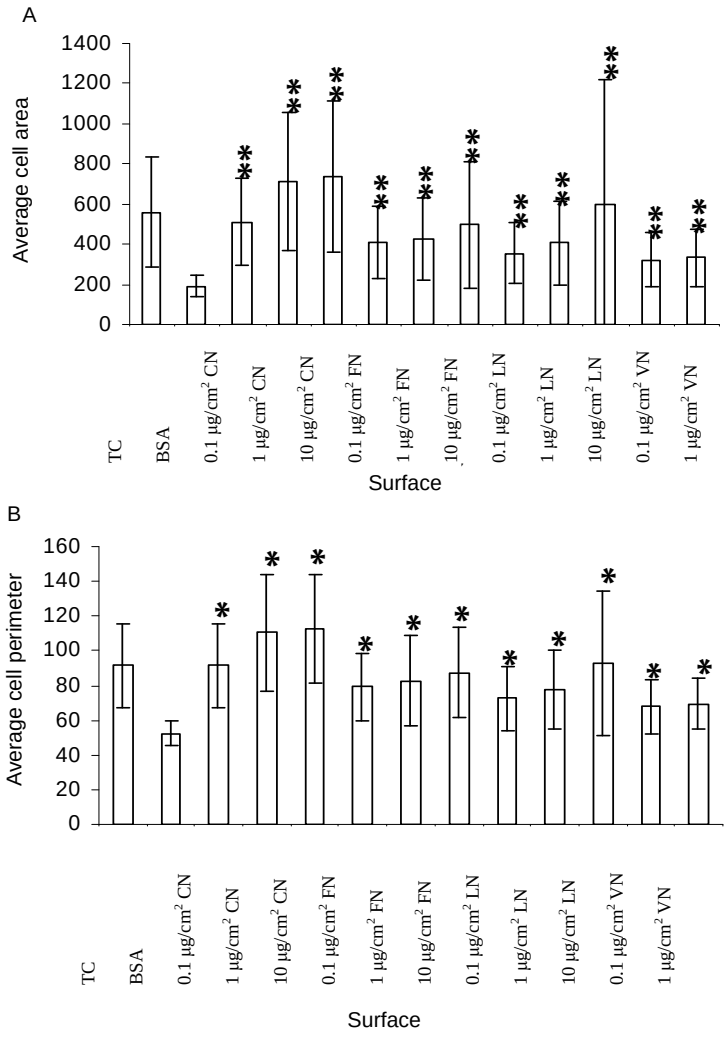

Figure 1. Effect of ECM protein-coated surfaces on the single cell area (A) and perimeter (B) of ARIP cells. ARIP cells were seeded on surfaces as indicated at a density of 3000 cells/cm^2 and cultured for 6 hours in F12K medium respectively. Each bar was given as means±SD. Significant differences are indicated as **P<0.01 vs. BSA.

containing 10% FCS showed normal growth. Therefore, for the long-term culture, it was not possible to maintain growth of ARIP cells on the ECM-protein coated surfaces in absolute serum-free medium without providing any extra essential component.

3.2. Growth of ARIP Cells in Defined Serum-free Medium

In order to provide a suitable serum-free culture environment for ARIP cells without using FCS, this work investigated the possibility to defining and optimising serum-free medium with known functional supplements including ITS, BSA, nicotinamide, KGF and GLP-1. As shown in **Figure 3**, when ARIP cells were cultured at a low seeding density (1.5×104 cells/cm^2), and cultured over 96 hours, there were significant differences in cell proliferation between normal culture medium containing 10% FCS (named as FCS group) and all serum-free cultivation groups (P<0.01). This suggested that it was difficult to establish cell proliferation within serum-free media if the cell density was too low. At a higher density studied (3×104 cells/cm^2), none of the serum freegroups supported cell proliferation as sufficiently as FCS group. However, cell proliferation in the FI F12K medium supplemented with BSA, ITS and nicotinamide (named as FI) or F12K medium supplemented with BSA, ITS, nicotinamide and KGF (named as FII) appeared to behigher than other serum-free groups. The addition of KGF in FII group did not show any additiveeffect. At the highest density studied, 6×104 cells/cm^2, after tissue culture for 96 hours, there was no difference among FCS, FI and FII groups, suggesting that FI and FII provided a tissue

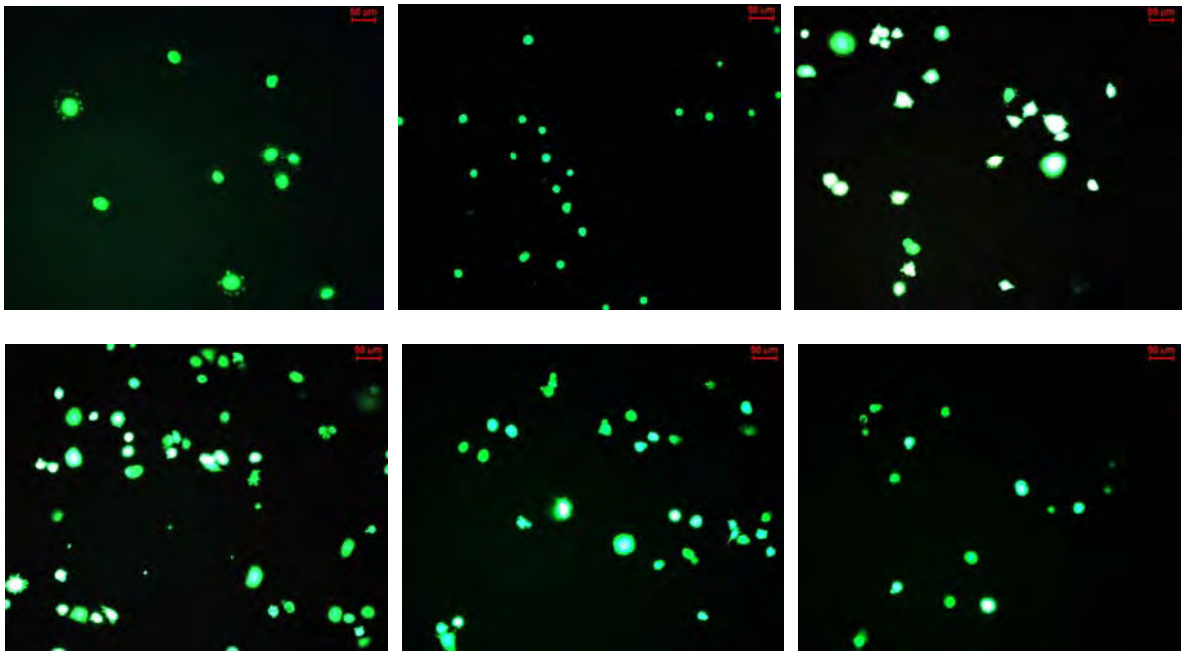

Figure 2. Morphology of ARIP cells cultured on different surfaces with F12K medium plus P/S for 6 hours. Magnification: X200. Cells were stained with 2uM of Calcein AM. A. TC surface. B. 1% BSA surface. C. 10μg/cm^2 CN surface. D. 10μg/cm^2 FN surface. E. 10μg/cm^2 LN surface. F. 10μg/cm^2 VN surface. The scale bar was 50 μm.

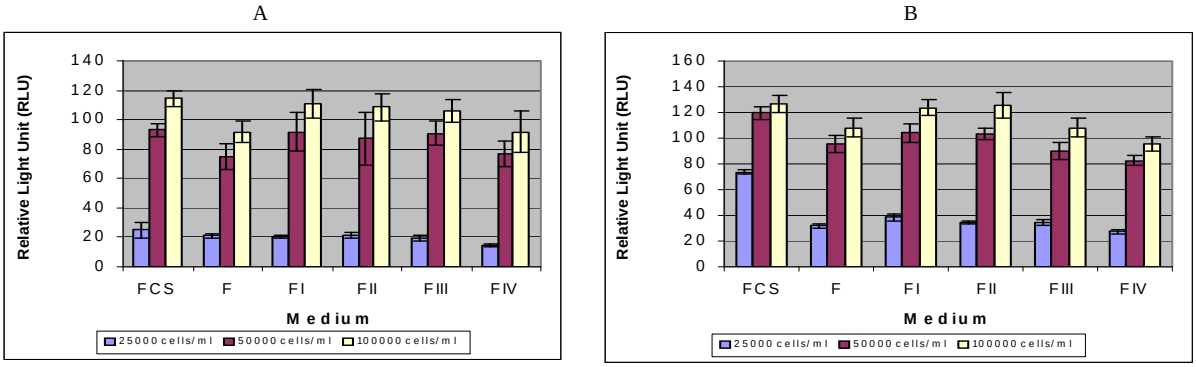

Figure 3. Relative light unit (RLU) by ATP assay which quantitatively indicates relative number of ARIP cells. FCS: F12K+10% FCS; F: F12K; FI: F12K+BSA+ITS+nicotinamide; FII: FI+ 10ng/ml KGF; FIII: FI+10nM GLP-1; FIV: FI+KGF+GLP-1. Each value was give as mean±SD from 6 observations. A. 48 hours. B. 96 hours. Significant differences are indicated as * P<0.05; **P<0.01 and ***P<0.001vs. FCS.

culture environment equivalent to culture medium containing FCS. The group of F12K medium supplemented with 10nM GLP-1 (named as FIII) did not improve cell proliferation even compared with the group of absolute serum-free medium (F group). Moreover, in the group of serum-free medium supplemented with both KGF and GLP-1 (named as FIV), ARIP cells showed the lowest proliferation rate compared with other serum-free culture conditions. These results implied that GLP-1 might play an inhibitive role in proliferation of ARIP cells especially in the presence of KGF. Overall, during the 96-hour period studied, reproduction or proliferation of ARIP cells under serum-free conditions was density-dependent. The supplements of BSA, ITS and nicotinamide together were found to maintain cell proliferation at equivalent levels to FCS.

3.3. Estimation of Cell Coverage in the Presence of ECM Protein-Coated Surfaces and Defined Serum-Free Medium

This study investigated the overall cell growth of ARIP cells in the presence of ECM proteins and defined serum-free medium by estimating the surface coverage of culture at three time points (4, 48 and 96 hours). As shown in **Figure 3**, after monolayer culture for 96 hours, the surfaces treated with CN and LN produced cell cov

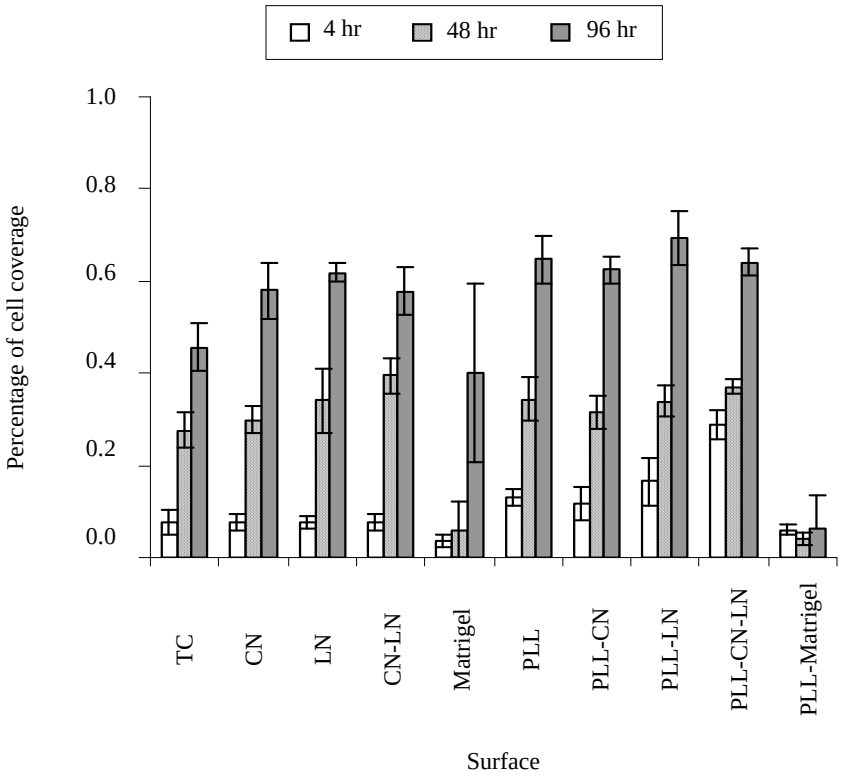

Figure 4. Surface coverage of ARIP cells. Cells were cultured in F12K supplemented with BSA, ITS, nicotinamide and P/S. Each value was given as means±SD from 3 individual observations. TC: Tissue culture surface. CN: collagen I coated surface. LN: laminin coated surface. CN+LN: 50% collagen I and 50% laminin coated surface. Matrigel: Matrigel coated surface. PLL: 0.01% ploy-l-lysine coated surface. PLL+CN: poly-l-lysine surface was further coated with collagen I. PLL+LN: poly-l-lysine surface was further coated with laminin. PLL+CN+LN: poly-l-lysine surface was further coated with 50% collagen I and 50% laminin. PLL+Matrigel: poly-l-lysine surface was further coated with Matrigel. Significant differences are indicated as * P<0.05; **P<0.01 or **P<0.001.

erage of approximately 60%, while the percentage was approximately 46% on tissue culture surface. Thus, CN and LN coated surfaces improved the cell surface coverage (P<0.05). PLL (0.01%) enhanced cell coverage slightly after culture for 96 hours no matter whether surfaces were coated with ECM proteins. Matrigel inhibited cell coverage either on its own or on PLL pre-coated surface. Moreover, the majority of ARIP cells appeared rounder in morphology and difficult to spread upon Matrigel-coated surfaces. In addition, distribution of ARIP cells on Matrigel-coated surfaces was patchy and uneven (**Figure 3**). In some of the captured images in the Matrigel-coated-surface group, a few of cells could be found. The addition of PLL did not alter the effect of Matrigel.

On the laminin-coated surfaces, the surface coverage increased by approximately 16% in the absence of PLL and 23% in the presence of PLL compared with non-treated tissue culture surface, suggesting the positive role of LN in the overall status of ARIP cells in defined serum-freemedium. The surface treated with CN and LN together appeared to show an effect after 48 hours, but after incubation for 96 hours, it was similar to the surfaces coated with CN or LN separately. Furthermore, the equivalent experiments were repeated using a lower cell density, 3×104 cell/cm^2, and the results also demonstrated that LN significantly promoted cell surface coverage, andMatrigel inhibited cell growth and surface coverage.

3.4. Insulin Production and Gene Expression under Differentiation Conditions

Immunofluorescence was carried out to identify insulin-producing ARIP cells induced by GLP-1. As shown in **Figure 5**, in the presence of 10 nM GLP-1 within serum-free medium, approximately 20-30% of ARIP cells were insulin positive, suggesting that GLP-1 was able to direct insulin-positive cell formation.

In order to investigate whether these insulin-positive cells can produce insulin, the insulin content within ARIP cells was carried out. Meanwhile, total cellular DNA content was applied to normalize insulin content and indicate cell proliferation. As shown in **Figure 5(a)**, after incubation for 72 hours, surfaces coated with ECM proteins studied resulted in large increases in total DNA content. The cell culture upon laminin-coated surface resulted in the highest DNA level, which was approximately 3-fold higher than that upon normal tissue culture plastic surface. Because the total DNA content reflects the cell number in each group, the data indicated that ECM proteins play a role in increasing cell number over the period studied. Furthermore, as shown in **Figure 5(b)**, all the ECM protein-coated surfaces appeared to improve the total insulin content in ARIP cells over a 72-hour period studied. Collagen-coated surface appeared to have the highest impact on insulin production when compared with surfaces coated with either fibronectin or laminin. After insulin production is normalisation by DNA content as shown in **Figure 5(c)**, it appeared that only the collagen-coated surface had a stimulative effect on insulin production given the same size of cell population. The collagen-coated surface showed approximately 1.8-fold higher normalised insulin content in ARIP cells than the uncoated tissue culture surface.

The presence of insulin gene expression in ARIP cells was measured using RT-PCR. As shown in **Figure 6**, despite the strong expression of β-actin as an endogenous control, insulin gene expression was weak in the entire groups studied. It appeared that ARIP cells upon collagen coated surface resulted in slightly higher insulin gene expression. Expressions of the other genes such as PDX-1 were not identified. Experiments were repeated at least three times and similar results were obtained. To ensure the gene primers used in RT-PCR were specific, RNA samples were isolated from RIN-m5F cells, a rat insulin-producing cell line, and used as controls. Results showed that RIN-m5F cells strongly expressed insulin and PDX-1 genes under identical RT-PCR conditions thus confirming the efficacy of the technique employed.

Given the combination conditions including collagen-coated surface, GLP-1 and defined serum-free medium, and after incubation for 72 hours, the ARIP cells were challenged with 5.5 mM and 16.7 mM of glucose. As shown in Figure 7, there appeared to be little difference in insulin secretion response to the two concentrations of glucose.

4. DISCUSSION

The work demonstrates that tissue culture polystyrene surfaces coated with different types of ECM proteins have effects on the morphological features of single ARIP cell. These changes can be detected by 5 hours.

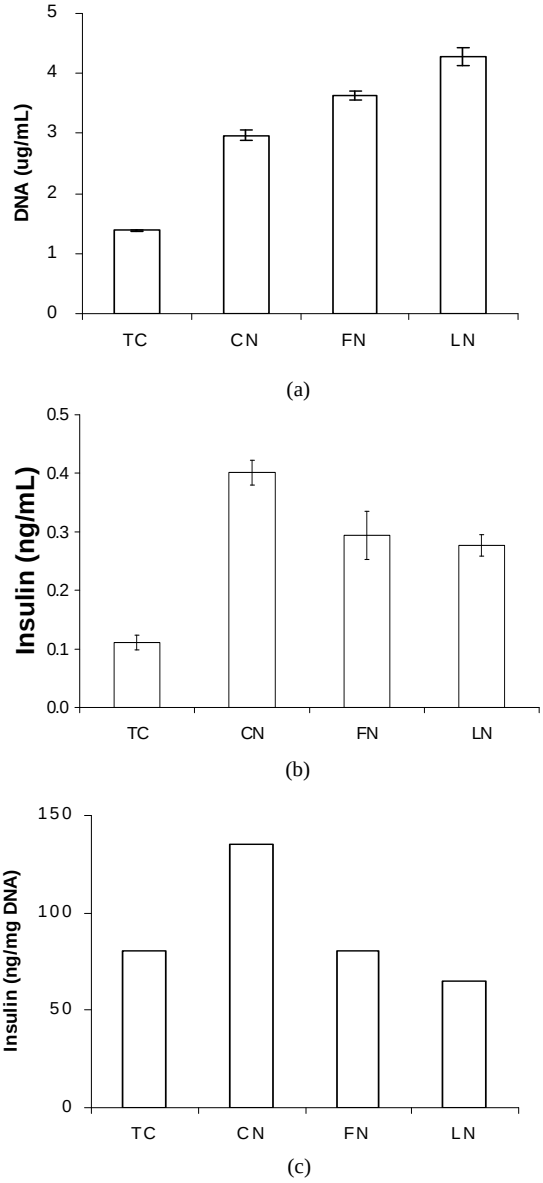

Figure 5. Insulin released by ARIP cells with response to ECM -protein-treated surfaces. Cells were cultured for 48 hours in F12K medium supplemented with ITS, BSA nicotinamide and GLP-1. TC: TC surface. CN: 10μg/cm^2 CN coated surface. FN: 10μg/cm^2 FN coated surface, LN: 10μg/cm^2 LN coated surface. Cell density: 5x104 cells/cm^2. Each value was given as mean±SD from 3 individual observations.

Their treatment effects on both single cell area and single cell perimeter were in the order of collagen Type I >fibronectin>laminin>vitronectin. Of the four ECM proteins studied, collagen-coated surface achieves the highest level, for example, the increase of single cell area is 2.7-3.8 fold compared with the BSA-coated surface as a control. Previous studies have identified the tripeptide RGD is located in all the four ECM protein types, and the RGD domain in the ECM proteins serves as a cell

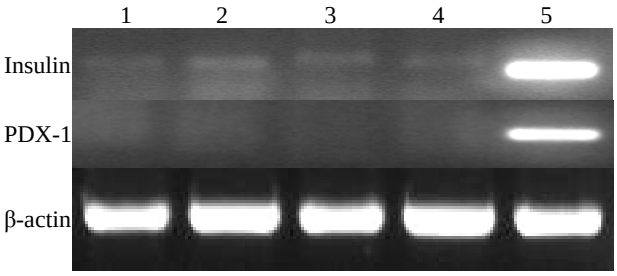

Figure 6. Expression of insulin and PDX-1 genes in ARIP cells following incubation for 72 hours in defined serum-free medium plus 10 nM GLP-1 and upon surfaces indicated. Lanes from 1 to 4 are RT-PCR products from ARIP cells. Lane 1:TC surface. Lane 2: collagen I coated surface. Lane 3: fibronectin coated surface. Lane 4: laminin coated surface. Lane 5:gene expression in RIN-m5F cells (an insulin-producing cell line from insulinoma) and used to validate the RT-PCR assay of each gene.

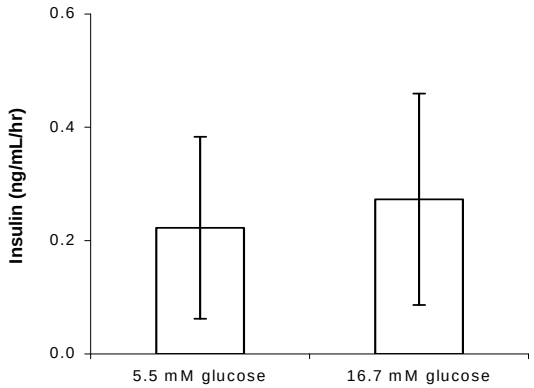

Figure 7. Insulin secretion in ARIP cells with response to glucose stimulation. Cells were cultivated for 72 hours in defined serum-free medium plus 10 nM GLP-1 and upon collagen coated surface. Each value was given as mean ± SD from 5 individual observations.

recognition site and plays a role in cell spreading through its binding to integrins [35]. However, as these four ECM proteins bind to different integrin patterns, this may explain their different effects on ARIP cells. Vitronectin has the weakest effects according to our data, it may be possible that vitronectin mainly binds to αvβ3 and αvβ5 integrins, which are not as effective or abundant as the other integrins [31].

Because without FCS, serum-free medium is not able to maintain the survival of ARIP cells upon ECM-protein coated surfaces, the work presents an optimal serum-free culture environment for the purpose of using ECM proteins effectively. Moreover, as proliferation of ARIP cells is density-dependent. The initial seeding density of cells should be high enough (e.g. 6×10^4 cells/cm^2) so as to maintain cells under serum-free medium conditions. This sufficient cell density may encourage cells interact effectively, thus enhancing survival of the total population. The impact of KGF on proliferation appears to be minimal when ARIP cells are cultured under serum-free conditions. However, KGF has been identified as an important growth factor of epithelial cells [31,43]. A previous study also suggests that KGF has a potential to induce pancreatic ductal cell proliferation in vivo [45]. The reason KGF doesn't not play a role in ARIP cells proliferation may be because ARIP are distinctive from primary pancreatic epithelium in terms of their origin and cellular characteristics. For example, the pancreatic regenerating gene proteins are mitogenic to primary cultures of ductal cells, but compared with their effects on the primary cultured ductal cells, these proteins were 100-fold less potent on ARIP cells [46].

Our results show that GLP-1 inhibits the proliferation of ARIP cells. This may be the result of transdifferentiation of pancreatic ductal cells induced by GLP-1 [4,5,15]. A previous study also provides evidence that GLP-1 promotes islet-cell neogenesis from pancreatic ductal cells in a type 2 diabetic rodent model [30]. Due to the inhibitory effect of GLP-1 on ductal cell proliferation, GLP-1 should be supplied at differentiation but not proliferation stage.

Surface coverage pattern of adhesive cells is determined by total cell number, individual cell features and surface properties in theory, thus it can reflect the dynamics of the overall cell performance under particular tissue culture conditions [1,12]. The ECM provides a backbone to influence the attachment of other proteins or influence cell adhesion directly via embedded cell signalling. Therefore, the coverage of monolayer cells on ECM protein-coated surfaces can indicate the overall patterns of cell status as consequence of adhesion, migration, proliferation and differentiation. Our results demonstrates that when monolayer ARIP cells are cultured for 4 days in optimised serum-free medium, surface coated with laminin has a significant supportive effect on coverage of ARIP cells. Because laminin has been demonstrated to improve the insulin accumulation and preservation of pancreatic endocrine cells [17,18,19], it can be employed when cells with pancreatic ductal characteristics are differentiated into an insulin-producing phenotype.

Collagen-coated surface appeared to increase the percentage of cell coverage especially in the presence of poly-L-lysine. A previous study has indicated that Collagen is useful for the culture of adult primary pancreatic epithelial cells from the main duct [27]. However, in embryonic pancreatic epithelia, laminin but not collagen has been demonstrated to induce duct formation [23]. Therefore, the exact signalling pathways of collagen and laminin for cell differentiation should be further investigated.

Poly-lysine can enhance electrostatic interaction between negatively-charged ions of the cell membrane and positively-charged surface ions of attachment factors on tissue culture plastic surface. When adsorbed to the culture surface, it may increase the number of positively charged sites available for cell binding. It has been known to be useful for enhancing effects of surface coating with ECM proteins. Our results confirm that Poly-L-lysine can improve the percentage of cell coverage on culture surfaces coated with selective ECM proteins.

In the presence of defined serum-free medium, Matrigel-coated surface inhibits the coverage of ARIP cells significantly. Indeed this inhibition can be detected even after 4 hours. In order to avoid the potential effects of growth factors in Matrigel, growth factor-reduced Matrigel has also been used, however, the inhibitive effect induced by Matrigel cannot disappear. Matrigel has been found important to promote the formation of islet-like clusters from primary pancreatic ductal epithelial cells [3]. It is possible that Matrigel induces the differentiation of pancreatic ductal cells leading to a decreased proliferation. However, due to the complex formulation of Matrigel, the exact signalling pathway needs to be further investigated.

In the presence of GLP-1, ARIP cells show different morphological structures and a loss of their typical cobblestone-like morphology. This morphological change may be due to the regulation of metabolism activities or induced differentiation. GLP-1 has been reported to induce insulin-producing cell differentiation from pancreatic acinar AR42J and ductal ARIP cells [15,47]. For example, exposure of rat AR42J cells to GLP-1 over 2 days result in an initial increase in levels of cyclic adenosine monophosphate and cellular proliferation, followed by cessation of proliferation and expression of the islet-associated hormones, insulin, glucagon, and somatostatin, in up to 50% of cells [47]. Furthermore, GLP-1 treatment also induces expression of glucose transporter 2 and glucokinase genes, in association with the capacity to secrete insulin in a glucose-dependent manner [47]. Therefore, the morphological change found here may be associated with transdifferentiation of ARIP cells. Interestingly, defined serum-fee medium also resulted in a slight change in morphology of ARIP cells. As nicotinamide has been considered capable of stimulating insulin-producing cell differentiation in other progenitor cell types [7,29], this may partly explain the morphological change of ARIP cells in defined serum-free medium. Immunofluorescence data in this study indicate that 20-30% of ARIP cells can obtain an insulin-positive phenotype after exposure to GLP-1. The insulin content of ARIP cells in the presence of GLP-1 can also be detected. Thus, it confirms that GLP-1 has the capability of converting ARIP cells into insulin-producing cells to some extent. The combination of the defined serum-free medium and GLP-1 leads to the maximum insulin production rate. This is as expected, because the defined serum-free medium is able to sustain the maximum growth of ARIP cells in a serum-free environment.

After the treatment with GLP-1 and/or defined serum-free medium, the gene expression of insulin in ARIP cells is observed at a low level. This indicates that the insulin content observed by ELISA is not from potential contamination or uptake that has been described in a previous study on the insulin-producing cell differentiation of embryonic stem cells [37]. The result obtained here appears similar to a previous study, which demonstrates the weak expression of insulin gene in GLP-1-induced ARIP cells by northern blot analysis [15]. However, no insulin gene expression was detected by another similar study [21]. Moreover, the expression of other relevant genes such as PDX-1 is not detected here. Therefore, although the insulin gene, not normally present in ARIP cells, is expressed, it is difficult to relate this study to the observations by other relevant studies.

In addition, although the role of GLP-1 in insulin-producing cell formation is confirmed, it remains unclear as to how GLP-1 triggers the insulin production in ARIP cells. Previous studies suggests that the initial step of GLP-1 action requires identification and binding of the peptide to the GLP-1 receptor, which is in the super-family of G protein-coupled receptors [41]. Activation of the GLP-1 receptor results in the stimulation of adenylyl cyclase, leading to an increase in intracellular cyclic adenosine monophosphate (cAMP) and the cAMP-dependent protein kinase A (PKA) activation in the pancreatic tissue [10,11,14,22]. However, the gene expression of GLP-1 receptor remains controversial as described in previous studies [15,21]. It is also reported that the action of GLP-1 depends on the expression of PDX-1. However, PDX-1 gene expression is not detected in this study, which is consistent with two of the previous studies [21,36]. Relevant studies on other adult non-β cells may provide additional clues. For example, the PDX-1 expression in the duodenal tissue is stronger than in intestinal epithelial cells, but GLP-1 could induce insulin production in intestinal epithelial cells but not in duodenum cells [38].

On the other hand, GLP-1 has been suggested to up-regulate expression of some other transcription factors such as Neurogenin 3 but not PDX-1 during insulin expression [38]. A study using adult hepatic progenitor cells has shown that the acute insulin secretion of non-PDX-1- expressing cells can be enhanced by GLP-1 in a time-dependent manner, though the effect of GLP-1 is strengthened in the presence of PDX-1 [25]. Indeed, there is no sufficient evidence to show that GLP-1 increases the PDX-1 gene expression during insulin producing cell conversion from other adult cell types. Taken

together, during the induction of insulin-producing-cell generation using adult progenitor cells, the role of GLP-1 may be enhanced by PDX-1 gene expression, but the exact signalling pathway of GLP-1 remains unclear.

5. CONCLUSIONS

In the presence of GLP-1 and defined serum-free medium, the total amount of insulin content in ARIP cells significantly increases upon the surfaces coated with ECM proteins including collagen, fibronectin and laminin. Meanwhile, comparison of total DNA content indicates that ECM-protein coated surfaces play a role in cell duplication, possibly through improved single cell spreading. After normalisation by DNA content, only collagen-coated surface appears to stimulate the insulin production given the same cell population size. The data obtained from gene expression also show that the insulin gene expression in ARIP cells upon collagen-coated surface appears slightly stronger. To date, there is still no sufficient information to determine how important ECM proteins are to insulin-producing cell formation from other cell types. Therefore, more experiments need to be carried out before the roles of ECM proteins can be fully illustrated. In particular, the distribution and activition of integrins may be important in revealing the profound function of these proteins.

6. ACKNOWLEDGEMENTS

This work was funded by the EPSRC. We thank Professor Kevin Shakesheff, Dr Sue Chan, Dr Richard Pearson and Mr Darryl Jackson for their critical advice and technical assistance.

REFERENCES

[1] B. T. M. Baharloo and D. Brunette, (2005) Substratum roughness alters the growth, area, and focal adhesions of epithelial cells, and their proximity to titanium surfaces, J Biomed Mater Res A, **74**, 12−22.

[2] S. B. Weir, L. A. Baxter, G. T. Schuppin, and F. E. Smith, (1993) A second pathway for regeneration of adult exocrine and endocrine pancreas: A possible recapitulation of embryonic development, Diabetes, **42**, 1715−1720.

[3] S. T. B. Weir, M. Weir, G. C. Tatarkiewicz, K. Song, K. H. Sharma, and A. O'Neil, (2000) In vitro cultivation of human islets from expanded ductal tissue, Proc Natl Acad Sci, **97**, 7999−8004.

[4] A. H. Bulotta, H. Anastasi, E. Bertolotto, C. Boros, L. G. Di Mario, U. Perfetti, R. Silver, K. Yao, F. Zenilman, M. E. Chen, and T. H. Magnuson, (2002) Cultured pancreatic ductal cells undergo cell cycle re-distribution and beta-cell-like differentiation in response to glucagon-like peptide-1, J Mol Endocrinol, **29**, 347−360.

[5] A. P. Bulotta, H. R. Hui, and L. G. Boros, (2003) GLP-1 stimulates glucose-derived de novo fatty acid synthesis and chain elongation during cell differentiation and insulin release, J. Lipid Res, **44**, 1559−1565.

[6] L. A. Chen, M. C. Alam, T. Miyaura, C. Sestak, A. O'Neil, J. Unger, and C. B. Newgard, (1992) Factors regulating islet regeneration in the post-insulinoma NEDH rat, Adv Exp.Med Biol, **321**, 71−80, 81−74.

[7] L. B. Chen, X. B. Jiang, and L. Yang, (2004) Differentiation of rat marrow mesenchymal stem cells into pancreatic islet beta-cells, World J Gastroenterol, **10**, 3016−3020.

[8] B. S. Chertow, N. Q. Goking, and H. K. Driscoll, (1997) Effects of all-trans-retinoic acid (ATRA) and retinoic acid receptor (RAR) expression on secretion, growth, and apoptosis of insulin-secreting RINm5F cells, Pancreas, **15**, 122−31.

[9] E. A. Clark and J. S. Brugge, (1995) Integrins and signal transduction pathways: The road taken, Science, **268**, 233−239.

[10] W. G. R. Ding, E. Rorsman, P. Buschard, and J. K. Gromada, (1997) Glucagon-like peptide I and glucose- dependent insulinotropic polypeptide stimulate Ca2+ induced secretion in rat alpha-cells by a protein kinase A-mediated mechanism, Diabetes, **46**, 792−800.

[11] H. C. S. Fehmann, M. and Goke, B. (1994) Interaction of glucagon-like peptide-I (7-37) and somatostatin-14 on signal transduction and proinsulin gene expression in beta TC-1 cells, Metabolism, **43**, 787−792.

[12] P. Feugier, R. A. Black, J. A. Hunt, and T. V. How, (2005) Attachment, morphology and adherence of human endothelial cells to vascular prosthesis materials under the action of shear stress, Biomaterials, **26**, 1457−1466.

[13] R. U. Gao, J. Pulkkinen, M. A. Lundin, K. Korsgren, and T. Otonkoski, (2007) Characterization of endocrine progenitor cells and critical factors for their differentiation in human adult pancreatic cell culture, Diabetes, **52**, 2003−2015.

[14] D. H. Gefel, G. K. Mojsov, S. Habener, and G. C. Weir, (1990) Glucagon-like peptide-I analogs: effects on insulin secretion and adenosine 3',5'-monophosphate formation, Endocrinology, **126**, 2164−2168.

[15] H. Hui, C. Wright, and R. Perfetti, (2001) Glucagon-like peptide 1 induces differentiation of islet duodenal homeobox-1-positive pancreatic ductal cells into insulin-secreting cells, Diabetes, **50**, 785−96.

[16] N. W. Jessop, (1980) Characteristics of two rat pancreatic exocrine cell lines derived from transplantable tumors, In vitro, **16**, 212.

[17] F. X. Jiang, (2005) Laminin-1 and epidermal growth factor family members costimulate fetal pancreas cell proliferation and colony formation, Differentiation, **73**, 45−49.

[18] F. X. C. Jiang, D. S. DeAizpurua, and L. C. Harrison, (1999) Laminin-1 promotes differentiation of fetal mouse pancreatic beta-cells, Diabetes, **48**, 722−730.

[19] F. X. Jiang and L. C. Harrison, (2001) Regulation of laminin 1-induced pancreatic beta-cell differentiation by alpha6 integrin and alpha-dystroglycan, Mol Med, **7**, 107−114.

[20] C. Q. Lin, (1993) Multi-faceted regulation of cell differentiation by extracellular matrix, Faseb, **7**, 737−743.

[21] H. K. G. Liu, B. D. Gault, V. A. McCluskey, J. T. McClenaghan, N. H. O'Harte, and P. R. Flatt, (2004) N-acetyl-GLP-1: A DPP IV-resistant analogue of glucagon-like peptide-1 (GLP-1) with improved effects on

pancreatic beta-cell-associated gene expression, Cell Biol Int., **28**, 69−73.

[22] M. W. Lu, M. B. Leng, and A. E. Boyd, (1993 The role of the free cytosolic calcium level in beta-cell signal transduction by gastric inhibitory polypeptide and glucagonlike peptide I (7-37), Endocrinology, **132**, 94−100.

[23] T. S. C. Maldonado, C. A. Kadison, A. S. Alkasab, S. L. Longaker, and G. K. Gittes, (2000) Basement membrane exposure defines a critical window of competence for pancreatic duct differentiation from undifferentiated pancreatic precursor cells, Pancreas, **21**, 93−96.

[24] C. Miyaura, L. Chen, M. Appel, T. Alam, L. Inman, S. Hughes, D. Milburn, J. L. Unger, and C. B. Newgard, (1991) Expression of reg/PSP, a pancreatic exocrine gene: relationshipto changes in islet beta-cell mass, Mol Endocrinol, **5**, 226−234.

[25] N. S. N. Nagata, T. Mitaka, T. Katakai, T. Yamato, E. Miyazaki, J. Tabata, Y. Sugai, and A. Shimizu, (2004) In vitro induction of adult hepatic progenitor cells into insulinproducing cells, Biochem Biophys Res Commun, **318**, 625−630.

[26] C. O. Welsh, (2001) Long-term culture in matrigel enhances the insulin secretion of fetal porcine islet-like cell clusters in vitro, Pancreas, **22**, 157−163.

[27] D. S. Oda, C. E. Nguyen, T. D. Swenson, and S. P. Lee, (1998) Culture of human main pancreatic duct epithelial cells, In Vitro Cell Dev Biol Anim, **34**, 211−216.

[28] T. Otonkoski, G. M. Beattie, M. I. Mally, C. Ricordi, and A. Hayek, (1993) Nicotinamide is a potent inducer of endocrine differentiation in cultured human fetal pancreatic cells, J Clin Invest, **92**, 1459−1466.

[29] T. Otonkoski, J. Ustinov, M. A. Huotari, E. Kallio, and P. Hayry, (1997) Nicotinamide and sodium butyrate for the induction of fetal porcine beta-cell differentiation prior to transplantation, Transplant Proc,**29**, 2045.

[30] R. A. H. Perfetti, (2004) The role of GLP-1 in the life and death of pancreatic beta cells, Horm Metab Res, **36**, 804−810.

[31] K. A. S. D. Preissner, (1998) Role of vitrGonectin and its receptors in haemostasis and vascular remodeling, Thromb Res, **89**, 1−21.

[32] R. P. Rafaeloff, G. L. Barlow, S. W. Qin, X. F. Yan, B. Rosenberg, L. Duguid, and A. I. Vinik, (1997) Cloning and sequencing of the pancreatic islet neogenesis associated protein (INGAP) gene and its expression in islet neogenesis in hamsters, J Clin Invest, **99**, 2100−2109.

[33] L. Rosenberg, (1995) In vivo cell transformation: neogenesis of beta cells from pancreatic ductal cells, Cell Transplant, **4**, 371−383.

[34] L. Rosenberg, R. Rafaeloff, , D. Kakugawa, Y. Pittenger, A. I. G. Vinik, and W. P. Duguid, (1996) Induction of islet cell differentiation and new islet formation in the hamster-further support for a ductular origin, Pancreas, **13**, 38−46.

[35] E. A. P. Ruoslahti, (1987) New perspectives in cell adhesion: RGD and integrins, Science, **238**, 491−497.

[36] K. A. Y. F. Silver, (2001) ARIP cells as a model for pancreatic beta cell growth and development, Pancreas, **22**, 141−147.

[37] S. E. Sipione, A. Lyon, J. G. Korbutt, and R. C. Bleackley, (2004) Insulin expressing cells from differentiated embryonic stem cells are not beta cells, Diabetologia.

[38] A. N. H. Suzuki and H. Taniguchi, (2003) Glucagon-like peptide 1 (1-37) converts intestinal epithelial cells into insulin-producing cells, Proc Natl Acad Sci U S A, **100**, 5034−5039.

[39] G. L. Teitelman and D. J. Reis, (1987) Differentiation of prospective mouse pancreatic islet cells during development in vitro and during regeneration, Dev Biol, **120**, 425−433.

[40] K. Terazono, H. Yamamoto, S. Takasawa, K. Shiga, Y. Yonemura, Y. Tochino, and H. Okamoto, (1988) A novel gene activated in regenerating islets, J Biol Chem, **263**, 2111−2114.

[41] B. Thorens, (1992) Expression cloning of the pancreatic beta cell receptor for the gluco-incretin hormone glucagon-like peptide 1, Proc Natl Acad Sci U S A, **89**, 8641−8645.

[42] B. E. A. O. Tuch, (1990) Maturation of insulinogenic response to glucose in human fetal pancreas with retinoic acid, Horm Metab Res Suppl, **25**, 233−238.

[43] T. R. Y. Ulich, E. S. Cardiff, R. Yin, S. Bikhazi, N. Biltz, R. Morris, and G. F. Pierce, (1994) Keratinocyte growth factor is a growth factor for mammary epithelium in vivo: The mammary epithelium of lactating rats is resistant to the proliferative action of keratinocyte growth factor, Am J Pathol, **144**, 862−868.

[44] R. N. K. Wang, and L. Bouwens, (1995) Ductto islet-cell differentiation and islet growth in the pancreas of duct-ligated adult rats, Diabetologia, **38**, 1405−1411.

[45] E. S. Y. Yi, S. Harclerode, D. L. Bedoya, A. Bikhazi, N. B. Housley, R. M. Aukerman, S. L.Morris, C. F. Pierce, and T. R. Ulich, (1994) Keratinocyte growth factor induces pancreatic ductal epithelial proliferation, Am J Pathol, **145**, 80−85.

[46] M. E. C. Zenilman and T. H. Magnuson, (1998) Effect of reg protein on rat pancreatic ductal cells, Pancreas, **17**, 256−261.

[47] J. W. Zhou, X. Pineyro, and J. M. Egan, (1999) Glucagon-like peptide 1 and exendin-4 convert pancreatic AR42J cells into glucagon and insulin-producing cells, Diabetes, **48**, 2358−2366.

J. Biomedical Science and Engineering, 2009, 2, 227-238 **JBiSE**
doi: 10.4236/jbise.2009.24036 Published Online August 2009 (http://www.SciRP.org/journal/jbise/).

Frequency sensitivity of nanosecond pulse EMF on regrowth and hsp70 levels in transected planaria

Ash Madkan[1*], Avary Lin-Ye[1], Spiro P. Pantazatos[2], Matthew S. Geddis[3], Martin Blank[2], Reba Goodman[1]

[1]Department of Pathology and Cell Biology, Columbia University College of Physicians and Surgeons, New York, USA; [2]Department of Physiology and Molecular Biophysics, Columbia University College of Physicians and Surgeons, New York, USA; [3]Department of Science, Borough of Manhattan Community College-CUNY, New York, USA.
Email: rmg5@columbia.edu

Received 30 June 2009; revised 10 July 2009; accepted 15 July 2009

ABSTRACT

Purpose: To study the effect of time varying/ pulsing electromagnetic fields (PEMF) on biological systems by measuring regrowth and the induction of elevated levels of the stress protein hsp70 in the regenerative model Planaria Dugesia dorotocethala. Objective: The outcomes of studies using electromagnetic fields (EMF) are dependent on pulse design, field strength (mG), frequency (Hz), duration and magnetic field/rise time (dB/ dt). Standardization of effective pulse design is necessary to avoid continuing confusion in the investigation of pulsing electromagnetic field (PEMF) technology. Information from studies on hsp70 protein induction and regrowth in transected Planaria provides information on EMF efficacy for potential clinical application in the treatment of ischemia reperfusion injury and the eventual inclusion of EMF prophylaxis prior to surgery. Materials and methods: Planaria were transected equidistant between the tip of the head and the tip of the tail. Individual head and tail portions from the same worm were placed in pond water and exposed to 8, 16 or 72 Hertz PEMF for one hour daily post transection under carefully controlled exposure conditions. Regrowth of heads and tails was measured in PEMF-exposed and sham control. Protein lysates from PEMF-exposed and sham control transected heads and tails were analyzed for hsp70 levels by Western blot analyses. Conclusion: The degree of regrowth and hsp70 levels in transected heads and tails exposed to nanosecond PEMF exposures at 8, 16 or 72 Hz was frequency dependent. There are currently several views on the interaction mechanism involved in regrowth. Here we discuss two: in one [7,8] we propose a direct effect on the DNA of the PEMF consensus sequence, nCTCTn, referred to as electromagnetic field response elements (EMRE) in the promoter region of the stress response gene HSP70. In the second mechanism [28] it is proposed that EMF induce vibrations of proteins through a series of quantized low frequency phonon signals.

Keywords: Planaria; Nanosecond EM Pulse; hsp70 Protein; Regrowth

1. INTRODUCTION

Electromagnetic fields (EMF) of less than 1 Gauss strength have been shown to induce a variety of specific effects in cells and tissues over a wide frequency range of the EM spectrum [7,8]. Nanosecond pulsing electromagnetic field (PEMF) technology has assumed increasingly greater importance in clinical treatments [15,29,70]. As a measure of efficacy, we used the regenerative model Planaria, to test three nanosecond PEMF devices on regrowth of transected heads and tails and the induction of the stress response protein hsp70 [42,43,44,45].

Previously we showed that ELF-EMF induce elevated hsp70 protein levels through the responsiveness of a specific consensus DNA sequence EMRE (electromagnetic field response element, nCTCTn) on the heat shock 70 (HSP70) promoter [41,42,43,44,45]. This DNA domain is upstream from the heat shock domain. Furthermore, ELF-EMF induction of the hsp70 protein protects cells and limits the effects of subsequent stress, including sudden changes in temperature [12,30].

The degree of electromagnetic field-effects on biological systems is known to be dependent on a number of criteria in the waveform pattern of the exposure system used; these include frequency, duration, wave shape, and relative orientation of the fields [6,29,32,33,39,40]. In some cases pulsed fields have demonstrated increased efficacy over static designs [19,21] in both medical and experimental settings.

Abbreviations: Extremely low frequency (ELF), electromagnetic fields (EMF); nanosecond pulsing electromagnetic field (PEMF), heat shock protein (hsp), heat shock gene (HSP), frequency (Hz), Gauss (G), magnetic field/rise time (dB/dt); mitogen-activated protein kinase (MAPK).

To examine the effects of PEMF on regrowth following transcetion and the induction of hsp70 protein in transected heads and tails, Planaria, a Platyhelminth, were used as a model organism because of its recognized ability to regenerate [55]. Previous studies showed that EM sinusoidal fields enhance the first three to six days of regeneration in Planaria and during this time specific proteins in the MAPKinase cascade are activated [26]. Planarians regenerate through a well defined stem cell system by restimulating mechanisms that guide the patterning of body structures during embryonic development [1,2,3,13,14,56,57,58,59]. Planaria are typically able to regenerate into a full worm from any body part within 14-16 days [55,32,33] thus providing a sensitive model for examining how electromagnetic fields interact with specific stages of regeneration.

The potential application of the upregulation of the HSP70 gene by both ELF-EMF and nanosecond PEMF in clinical practice would include trauma, surgery, peripheral nerve damage, orthopedic fracture, and vascular graft support, among others. Regardless of pulse design, EMF technology has been shown to be effective in bone healing [5], wound repair [11] and neural regeneration [31,36,48,49,51,63,64,65,66]. In terms of clinical application, EMF-induction of elevated levels of hsp70 protein also confers protection against hypoxia [61] and aid myocardial function and survival [20,22]. Given these results, we are particularly interested in the translational significance of effect vs. efficacy which is not usually reported by designers or investigators of EMF devices. More precise description of EM pulse and sine wave parameters, including the specific EM output sector, will provide consistency and "scientific basis" in reporting findings.

2. MATERIALS AND METHODS

Planaria. Dugesia dorotocethala (Carolina Biological Supply Company; cat. # 132950) were shipped overnight and allowed to 'recover' for at least 24 hours in fresh oxygenated pond water (Carolina Biological Supply Co, NC, USA). Planaria were maintained in near darkness at 22 to 24^{o}C (Precision Scientific incubator; Fisher Scientific, NJ, USA) throughout the experiments.

2.1. Experimental Protocol

Planaria Dugesia dorotocethala were transected equidistant between the tip of the head and the tip of the tail (**Figure 1**). The following is the experimental protocol used in these experiments:

1) Following transection (0 time) head and tail portions were exposed to 8, 16 or 72Hz nanopulse for one hour twice a day. Measurements of regrowth were performed from 0 time to at least three day intervals (n = > 10 experiments).
2) Following transection, heads and tails were exposed to 8, 16 or 72 Hz up to 180 minutes. Samples were removed at 20 minute intervals for protein extraction and hsp70 analyses (n = >10).
3) Following transection, heads and tails were exposed to 8, 16 or 72 Hz fields for one hour twice per day over a 12 day time period. Ten head and tail samples were removed daily and prepared for hsp70 analyses. Experiments were repeated at least three times.

Exposure protocol. In the experiments described here, Planaria Dugesia dorotocethala were transected equidistant between the tip of the tail and the head **(Figure 2).** Each head and tail portion was photographed using a Nikon digital camera mounted on a Wilde dissecting microscope. Images were stored in a database for subsequent measurements using ImageJ (see section on Quantitation). Head and tail portions were placed in

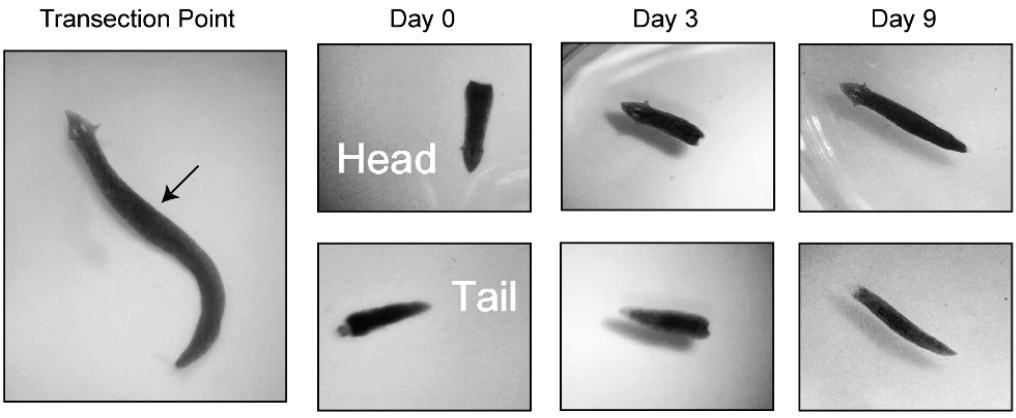

Figure 1. Transection of Planaria. The image in the left panel shows an intact sham exposed planaria with head facing up. The arrow indicates the transection point. The adjacent panels show representative images of heads and tails from transected Planaria at days 0, 3, and 9. The images have been enlarged 16X to show detail.

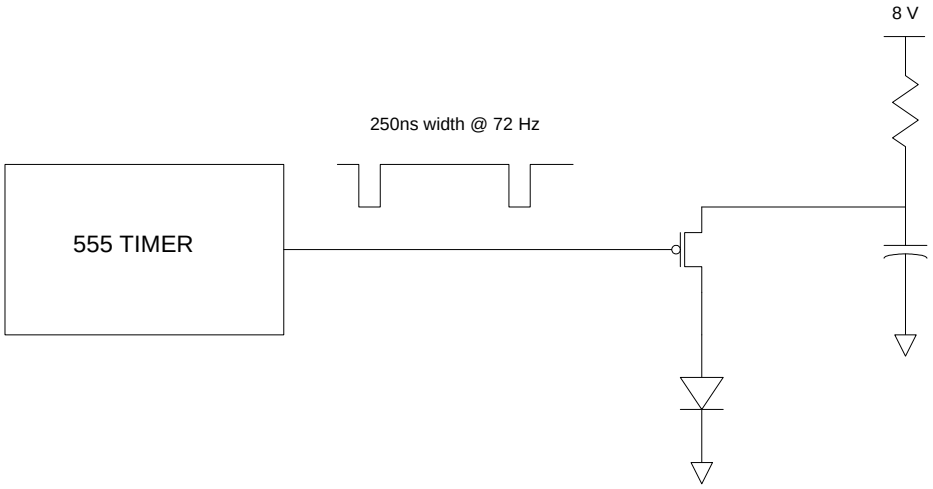

Figure 2. EM Probe Device. This device is designed to generate fast magnetic field pulses of low duty cycle in the near field region. The pulse length is about 250ns driven by a storage capacitor and a MOFSET switch that produces a 10A current in a field generating circuit element. The circuit element is just the single loop of the capacitor and switch circuit and does not contain any additional coil or turns of a conductor to enhance the magnetic field strength. The compact single loop design minimizes inductance and increases the speed of the circuit allowing a fast rise pulse producing a maximum magnetic field of the order of one Gauss at about 1cm from the device. The field is concentrated in a region of a few cm^3 and falls off rapidly outside that region. The fast rise and fall of the current and magnetic field pulse implies a broad spectrum of Fourier components contain within the repeated pulse of the waveform. For the pulse rise time of about 10ns and a pulse frequency of 72Hz, those components extend from the fundamental frequency at 72Hz at the low end to at least 20MHz at the high frequency end. The particular distribution of frequencies is determined by the usual methods of Fourier analysis from the exact pulse shape. This wide range of frequency offer resonant interactions with the biological mechanisms of the organism being treated over a very wide range and could include molecular, cellular and multicellular level interactions.

separate Petri dishes (Falcon 351007 60 x 15mm; Fisher Scientific, NJ, USA) containing pond water approximately 0.6cm deep. Dishes were numbered so that heads and tails of the same worm could be identified for measurements. Dishes were placed on a firm base and the PEMF devices were attached to the dishes so that the entire area of the dish was exposed to a uniform field for one hour a day. All exposures took place within an incubator with the temperature maintained at 22-24^{o} C and monitored with a thermocouple probe (sensitivity +/- 0.01^{o}C; Physitemp, model BAT12, Hackensack, NJ, USA). Growth was assessed at three-day intervals from day 0 (immediately following transection and the onset of PEMF exposure) to day 12 post-transection. In a series of separate experiments, pigmented eye spot development was monitored at 12 hour intervals in transected tails exposed to PEMF and sham control immediately following transection.

The nanosecond PEMF device (**EM-PROBE Technologies)** in **Figure 1** generates a near field fast magnetic pulse of 250 nanosecond (ns) duration, which is driven by a circuit containing a storage capacitor and a switch that produces a 10 A current in a field-generating circuit element. The single loop circuit does not contain any additional coils of a conductor to enhance the magnetic field strength, and allows a rapid dB/dt pulse design producing a magnetic field of 1 Gauss approximately 1 cm from the device. The pulse begins with a peak strength of 1.4-1.7 Gauss that deteriorates to zero in about 200ns. At 72Hz this means that there is an active field for 0.00072% of the time. At 16 Hz there is an active field for 0.00016% of the time. At 7.8Hz there is an active field for 0.000078% of the time. The particular distribution of frequencies is determined by Fourier analysis from the exact pulse shape. This wide range of frequencies offers resonant interactions with the biological mechanisms of the organism being treated. The entire output circuit is optimized for rapid response by minimizing inductance. The wide range of frequencies offers resonant interactions with the biological mechanisms of the organism being treated over a wide range and might include molecular, cellular and multicellular interactions.

Shielding: Both active (experimental) and sham- exposed (control) samples were enclosed in 30cm high, 15cm diameter cylindrical Mu metal containers (0.040" thickness) (Amuneal Corp. Philadelphia, PA). Detailed measurements of background magnetic fields in the incubator, harmonic distortion, DC magnetic fields and mean static magnetic fields in the incubators were previously determined [35].

Protein lysates. In a separate series of experiments, protein was extracted at defined time periods from the transected heads and tails, both experimental and sham, to determine effect of PEMF on hsp70 levels. Lysates were prepared from the heads and the tails of exposed and sham exposed Planaria for analyses of hsp70 [41, 42,

45]. Protein concentrations were determined by the Bradford assay (Bio-Rad Redmond, WA, USA).

Western blot. Lysed samples containing 30µg of protein were subjected to sodium dodecyl sulfate gel electrophoresis (Fisher Scientific, NJ, USA) on 10% polyacrylamide gels using appropriate molecular weight markers (Santa Cruz Biotechnology Inc, Santa Cruz, CA, USA) and the polypeptides were transferred to polyvinylidene fluoride membrane for immunoblotting. Blots were probed with anti-hsp70 antibody (1:10,000). The blots were then stripped using SuperSignal West Pico Stable Peroxide Solution (Pierce, prod # 1859674, Fisher Scientific, NJ, USA) and SuperSignal West Pico Luminol Enhancer Solution (Pierce prod # 1859675, from Fisher Scientific, NJ, USA) and reprobed with anti-actin (1:1000) to confirm equivalent loading. Visualization was by the enhanced chemiluminescent detection system (Fisher Scientific, NJ, USA) as previously described [43].

Antibodies. The antibody to hsp70 was kindly provided by Dr. Richard Morimoto, Northwestern University.

Statistical analysis: For determination of regrowth, multiple high-resolution digital pictures of Planaria heads and tails were taken at three day intervals and the rate of regrowth quantified using ImageJ v1.38 (http://rsb.info.nih.gov/ij). Length measurements were calibrated in millimeters and transposed to an Excel spreadsheet for statistical analysis. Lengths were normalized to the 0-time. Length differences over each 3-day interval were then subjected to 2-sample t-tests to assess significant differences in mean growth between the control and exposed conditions for both heads and tails. An additional analysis was conducted in SAS v9.1 (www.sas.com) to assess the significance of an interaction effect, i.e., whether the exposure had greater effect on either heads or tails. For this a 'mixed effects' analysis was performed which modeled the average length at 3-day intervals as a linear sum of the fixed effects of exposure (experimental vs. control), worm portion (heads vs. tails) and their interaction.

For quantification of the hsp70 and beta-actin levels the films from Western blot were scanned and saved as digital images (**Figure 3**). The densities of the bands were quantified using the histogram function in ImageJ and values transposed to Excel for statistical analysis (2 sample t-tests). A minimum of three replications of each assay were conducted.

2.2 Western Blots Quantitation of Hsp70 and β-actin Bands

Images from films were scanned into a computer and analyzed with Image J v1.37 (NIH). The analyze function for gels was used to plot the spatial signal density for each lane of hsp70 (see **Figure 2**). The same was done for the β-actin controls (not shown). **Figure 2** plots the mean hsp70/-actin ratios for PEMF and Control conditions. These values were imported into a Microsoft Excel spreadsheet where the signal value of hsp70 was divided by the value of the-actin signal in the same lane in order to normalize against variable loading volumes. -actin is a housekeeping gene and unaffected by EMF or PEMF. Statistical analyses were also conducted in Excel using the Data Analysis toolbox.

3. RESULTS

The extraordinary ability of Planaria to regenerate after injury is attributed to the presence of totipotent neoblasts capable of differentiating into all of the tissue types [1, 4]. Perhaps most impressive is their ability to regenerate the nervous system. When transected the tail region forms a new head complete with bilateral optic nerves and eyes, a two-lobed brain, and a pair of ventral nerve cords (VNC) [2,13,14].

3.1. PEMF Accelerates Rate of Regrowth of Transected Planaria

To assess the efficacy of the nanosecond PEMFs on Planaria regeneration, the length of ELF-EMF-exposed and sham control heads and tails were measured at three-day intervals starting immediately following transection (**Figure 4 A,B,C**). The heads and tails of all transected Planaria (experimental and control) regrew to normal viable worms. The initial experiments used PEMF at 72Hz.to measure regrowth of transected heads and tails. As previously demonstrated using ELF-EMF [26], accelerated tail regrowth was significant at days 3 and 6 post transaction (p=0.05). In contrast to the effect of exposure to72 Hz PEMF, 8Hz PEMF exposure on the tail portion showed the greatest response to any of the

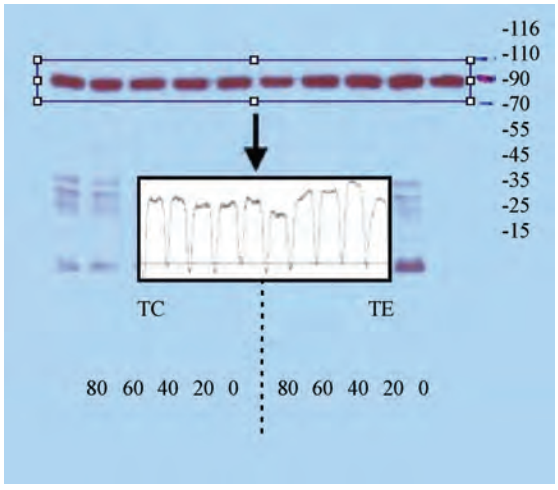

Figure 3. Images from films were scanned into computer and analyzed with Image J v1.37 (NIH). The 'analyze function for gels' was used to plot the spatial signal density for each lane of hsp70. The same was done for the β-actin controls (not shown). These values were imported into a Microsoft Excel spreadsheet where the signal value of hsp70 was divided by the value of the β-actin signal in the same lane in order to normalize against variable loading volumes. β-actin is a so-called 'housekeeping gene' and unaffected by EMF or EMP. Statistical analyses were also conducted in Excel using the Data Analysis toolbox.

frequencies to which the transected heads and tails were exposed. The sham control samples in general showed very little change in length over this time period **(Figure 3B)**. A reduced response to the 16Hz PEMF **(Figure 3C)** was measured in both transected heads and tails when compared with 72 and 8Hz **(Figure 3A, B)**.

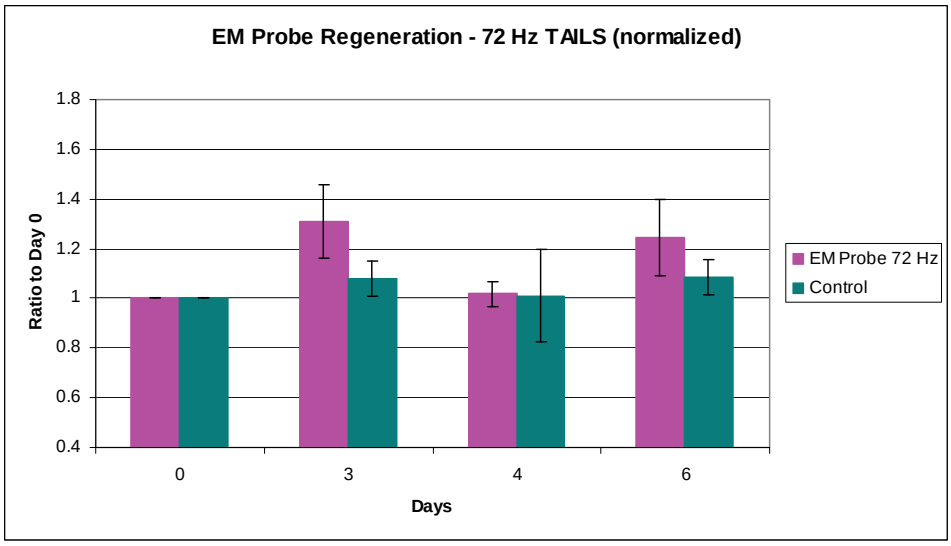

Figure 4A. Regeneration of heads and tails following transection of Planaria. Histograms showing the mean length of control and PEMF-exposed heads and tails immediately post-transection (0 time), and 3 to 9 days post-transection. (A) Mean length ± 2 standard error of the mean (SEM) of exposed heads (HE, n=48) and sham exposed heads (HC, n=27) at each time. (B) Mean length ± 2SEM of exposed tails (TE, n=20) and sham exposed tails (TC, n=12) at each time. The asterisks indicate a significant statistical difference in the rate of regeneration between exposed and sham exposed heads and tails assessed by 2-sample t-tests of mean difference in length.
A. Exposure to 72Hz accelerated tail regrowth was significant at days 3 and 6. post-transection [data normalized against day zero (n=3)]. The effect of the 72Hz EM probe is `statistically significant (p=0.05) at three and six days on the tail portion. The heads and tails of all transected Planaria (experimental and control) regrew to normal viable worms by 20 days. There was little or no measureable effect on regrowth in head portion.

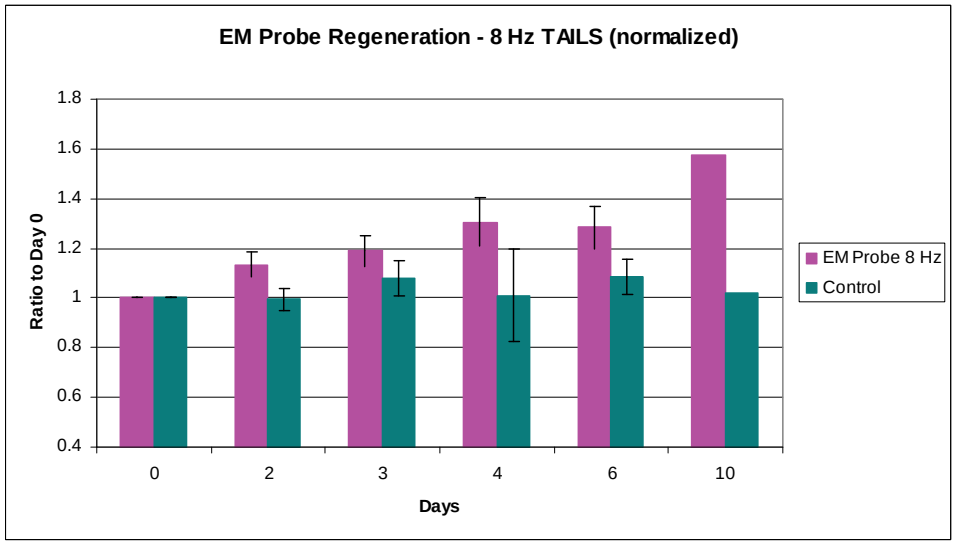

Figure 4B. In contrast to the effect of exposure to 72 Hz PEMF, transected tails exposed to the 8Hz EM probe show a steady increase in length. The effect of 8Hz PEMF on the tail portion showed the greatest response to any of the frequencies to which the transected heads and tails were exposed. The sham control samples and the head exposed samples showed very little change in length over this time period.

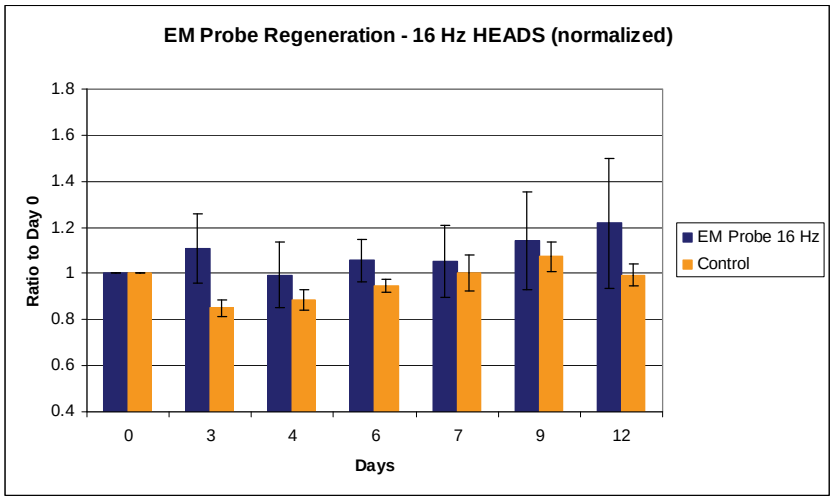

Figure 4C. A reduced response to the 16Hz PEMF was measured in both transected heads and tails when compared with 72 and 8Hz.

Of particular interest was the general trend of the responsiveness of the tail to the three frequencies tested as compared to the head portions **(Figure 4 A, B, C**). The third day after transection has been shown to be the time of maximal ELF-EMF-stimulated growth of the tail [26]. During normal regeneration this is the developmental stage when the neural networks are actively forming [13, 14] and the ventral nerve cords (VNC) are extending from the head into the newly formed tail.

3.2. PEMF Activation of Hsp70 Associated with Injury and Repair

A significant elevation in hsp70 levels was evident in tail portions that were exposed to the nanosecond PEMF using all three frequencies at 0, 20, 40, 60 and 80 minutes (**Figure 5**). We also looked at potential differences in induction of hsp70 protein, comparing all separate PEMF exposures to the sham control. Tails that were exposed to 16Hz EM-Probe fields showed the highest hsp70 production (p= .000007.91).

In terms regrowth, the 8Hz tails shows the quickest response to PEMF (**Figure 4B**). The 72Hz also shows a noted difference between exposed and unexposed worms (**Figure 4A**). The 16Hz was too inconsistent in order to draw any conclusions (data not shown).

We believe the accelerated regrowth above is consistent with the role of hsp70 as a chaperone that monitors the folding of proteins during repair. PEMF induction of the HSP70 gene may result from events triggered by the activation of ERK that utilize a unique consensus sequence (electromagnetic field response element; EMRE) upstream from the heat shock consensus sequence [8, 9,10].

The increase paralleled the accelerated regeneration noted above and is consistent with the role of hsp70 as a chaperone that monitors the folding of proteins during repair. Induction of the HSP70 gene may result from events triggered by the activation of ERK that utilize a unique consensus sequence (electromagnetic field response element; EMRE) upstream from the heat shock consensus sequence [42,47]. Stress response protein hsp70 levels are elevated after exposure to PEMF [43, 44,45]. We next examined the effect of nanosecond PEMF at 8, 16 and 72 Hz exposures on levels of this protein. Earlier studied had shown that hsp70 levels (**Figure 5A,B**) depicts mean hsp70/-actin ratios and 95% CI for both 16Hz and 72Hz exposure conditions on heads and tails respectively vs. their control counterparts. With both frequencies we observed a spike in hsp70 levels at 40 minutes which concurs with our previous data [41,45] and as previously noted the hsp70 levels return to normal levels by 120 minutes. [Mean hsp70/-actin ratios for 16Hz EMP Heads (n=14), 16Hz EMP Tails (n=14), 72Hz EMP Tails (n=17) and 72Hz EMP Heads (n=13).] As expected, measurements of hsp70 during regrowth showed little to no effect of exposures.

4. DISCUSSION

In the experiments reported here we examined nanosecond PEMF, rapid dB/dt using 8, 16 and 72Hz EM probe devices on induction of hsp70 levels and Planarian head and tail regrowth post-transection. Our data show that the induction of elevated hsp70 levels and regrowth following transection are frequency specific; tail portions that regenerate nervous system, brain and eyes, are more responsive to the EM probe device than head portions. The effectiveness of time varying electromagnetic fields on biological systems has been shown to be dependent on pulse design; frequency, duration, magnetic field/rise time (dB/dt) [29,30]. Measurements of EMF induced

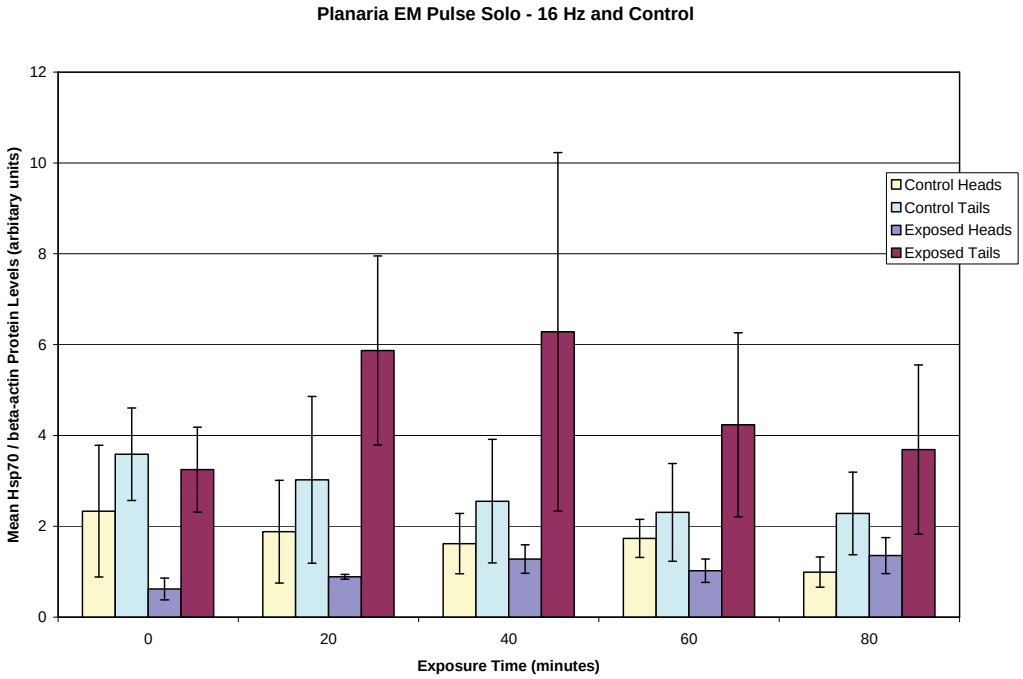

Figure 5A. Histogram showing a quantitative analysis of hsp70 protein levels from regenerating heads, tails, and sham controls. The relative protein levels are expressed in arbitrary units based on the intensity of the hsp70 protein band from the Western blots. The PEMF exposed tails show an obvious spike between 20 and 40 minutes. Mean hsp70/β-actin ratios for 16 Hz PEMF heads (n=14), 16 Hz PEMF tails (n=14), 72 Hz PEMF tails (n=17) and 72 Hz PEMF heads (n=13). The control groups for each sample had a sample size equal to that of its corresponding PEMF group. Error bars represent 95% confidence intervals (± 2*Standard Error).]

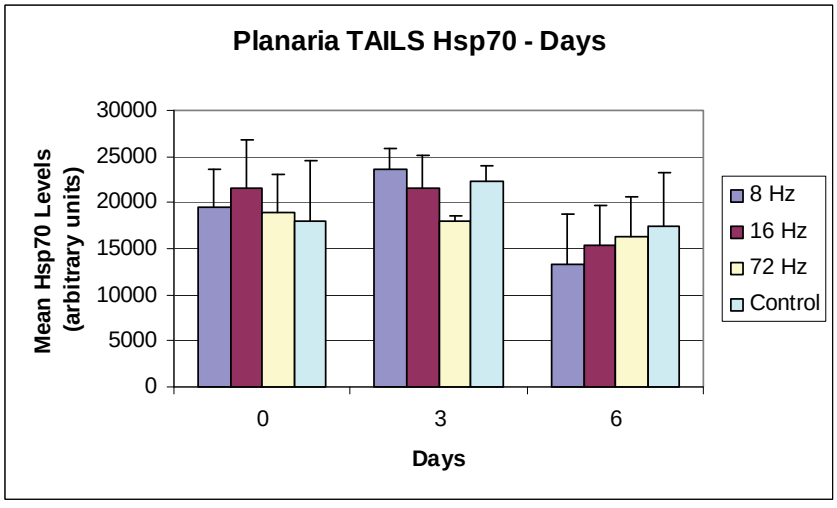

Figure 5B. Histogram showing a quantitative analysis of hsp70 protein levels from regenerating heads, tails, and sham controls.[Mean hsp70/β-actin ratios for 16 Hz EMP heads (n=14), 16 Hz PEMF tails (n=14), 72 Hz PEMF tails (n=17) and 72 Hz PEMF heads (n=13)]. The control groups for each sample had a sample size equal to that of its corresponding EMP group. Error bars represent 95% confidence intervals (± 2*Standard Error).]

hsp70 levels and induction of post-transected re-growth were used as markers for repair efficacy in this study. Standardization of effective pulse design is necessary to avoid continuing confusion in the investigation of puls-

ing electromagnetic field (PEMF) technology. The data from hsp70 protein induction and regrowth in Planaria, a regeneration model, as a measure of EMF efficacy, suggest excellent opportunity for clinical use in treatment of ischemia reperfusion injury and the inclusion of EMF prophylaxis prior to surgery. Our focus in these experiments was on: (a) regrowth of head and tail portions following transection, (b) immediacy of hsp70 induction during regeneration of heads and tails, (c) levels of hsp70 elevation during regeneration of heads and tails and (d) duration of hsp70 elevation. We have shown that the tail portion of the transected Planaria is more sensitive to different frequencies both in the induction of hsp70 levels and in regrowth. Furthermore, these changes in tail metabolism occur at different times depending upon the frequency used in the exposure.

4.1. Interaction Mechanisms

How weak electromagnetic (EM) fields interact with DNA to stimulate protein synthesis remains unknown; EMF interaction with cells and tissues has been examined in a variety of *in vivo* and *in vitro* systems including enzyme reactions [10], *Drosophila* [25,27,72], yeast [71] cultured cells [23,24,53] and on regeneration in Planaria [26]. Currently no definitive mechanism exists to explain how EMF interact with DNA and proteins in cells and tissues, although several theories have been proposed including cyclotron resonance [40], and a modification of this idea [6,37].

There is some evidence that EM fields can affect DNA, both directly and indirectly [9]. We have shown a unique DNA sequence in a specific domain on the HSP70 promoter that is sensitive to EM field exposures and this observation has contributed to the understanding, in part, of how ELF-EMF affects biological systems. There are specific regions on the promoters of some genes, HSP70 and c-*myc* for example, that contain this consensus sequence and when this sequence is transfected into promoter of reporter genes, these genes become sensitive to EMF, whereas before they were not. [41,42,43,44,45]. EM fields initiate up regulation of the HSP70 gene, increase mRNA transcripts and hsp70 protein levels. The responsiveness is dependent on the number of copies of the nCTCTn consensus sequence. [42]. Electromagnetically, responsive elements act as 'sensors'. This is an HSF-1 dependent process as shown by electrophoretic mobility shift assays (EMSA) of protein extracts from HL60 cells exposed to EMF. HSF1-DNA binding activity was demonstrated by a supershifted band. The magnetic field-inducible heat shock element-binding activity is HSE sequence-specific and contains HSF1 [45].

Because of the demonstrated effect of EMF on electron transfer reactions, it has been proposed that displacement of electrons in the H-bonds that hold DNA together can lead to DNA chain separation, thus initiating transcription [7,8]. The resultant charging due to electron displacement on the dynamics of DNA chain separation suggests that electron transfer could favor separation of base pairs e.g. nCTCTn, with the EM field sensitive DNA sequence acting as the first order iterative mechanism. In the case of Planaria the DNA in the totipotent stem cells created by the injury may be responding directly to the EM fields. It has been shown that DNA-mediated charge transport and the oxidative damage that results are extremely sensitive to variations in the sequence and conformational-adaptive response leading to stacking of the intervening bases [18,62]. Protein-binding to DNA, for example, through one or more of the MAPKinase cascades, modulates long-range charge transport negatively and positively depending upon the specific protein DNA interactions in play [52,54,68,69].

A possible mechanism for EMF initiation of protein synthesis is by acting on the de-localized π electrons in the base pairs that hold the DNA strands together. This is one way in which the effect of EMF in ELF range can be due to the resulting current. The charging of molecular complexes has been shown to lead to their disaggregation [10], so local charging would be expected to cause the DNA strands to disaggregate. A possible sequence of steps may start with EMF displacing electrons and charging DNA segments, followed by disaggregation of DNA strands as a result of the charging.

The properties of the CTCT bases suggest that they may be involved in the first step in a molecular mechanism for EMF activation of protein synthesis. They have low electron affinities, so electrons would be more easily displaced by the EMF. Also, the CTCT are pyrimidines, and when the H-bonds split between CTCT and the GAGA (purines) bases on the complementary chain, the smaller area that results would require less energy, and make the disaggregation more favorable [7].

Two recent studies of molecular properties of DNA add support to this proposed mechanism of DNA disaggregation. One paper compared the lifetimes of excitation induced by ultraviolet (UV) light in different DNA structures [60]. Apparently, the induced fluorescence had significantly longer lifetimes in DNA chains composed of A and G bases than in chains with C and T bases. The critical non-thermal stress protein sequences, the CTCT pyrimidines, were found to have the shortest UV stimulated fluorescence lifetimes. Their conjugate GAGA purines were found to have lifetimes that are approximately an order of magnitude longer.

Fluorescence lifetimes are measured in the picosecond time range, a relevant time scale for molecular rearrangements. Since the fluorescence lifetimes relate to the properties of the excited molecule and not to what caused the excitation, the measured UV excitation life-

times in the picosecond range also applied to lifetimes of perturbations due to EMF. Therefore, the studies suggest that the conjugate segments on the DNA strands will retain energy for significantly different lengths of time. The shorter lasting perturbation is evidence of more rapid dissipation of energy through collisions and a greater likelihood of reaching a breaking point, while the rest of the chain is a being held in place by the conjugate strand.

A second paper [46] on the flexibility of the double DNA helix found that stretching fluctuations were much larger than expected and extended over two turns of the DNA helix (over 10 base pairs). The double helix is apparently much more flexible than would be expected from the multiple H-bond links between the two strands, and mechanical stresses are probably more easily transmitted along the strand. The flexibility of the DNA double helix would make the local unraveling of the two strands proceed more easily once it starts.

These recently described properties of the DNA double helix support the idea that CTCT sequences are likely to play a greater role in DNA strand separation leading to initiation of transcription. Similar responses can occur with other base sequences, but they would require greater energy and are less likely to occur at lower frequencies. At higher frequencies, electron movements are apt to be induced all along the DNA strands.

Another approach to mechanism has been proposed by Gordon [28]. According to this model DNA function is controlled by acoustic signals (phonons), which can be enhanced via stochastic summation, i.e use of background. 'noise' if required, to complete the signal at the necessary strength [28]. This idea proposes that protein iterative activities account for enzyme activation, channel completion, and other functions necessary for cell homeostasis, and have been an integral part of electromagnetic responsive elements nCTCTn. Thus the suggestion that paramagnetic/diamagnetic transduction (damping) is a first order mechanism in this dynamic centered around the Schrodinger equation [to create a binary phonon signal series is extant in the literature [28]. According to this theory, beta sub-units direct protein conformational adaptation in response to acoustic signal series to complete an EM driven control circuit capable of directing oxidation-reduction reactions (Ubbink *et al*. [67]. An alternate mechanism to variations on cyclotron resonance has been suggested by [16,17]. Gordon [28] and Panagopolus [50] suggest that EM fields may act as classical "forcers" in a resonance system with paramagnetic/diamagnetic oscillators that "damp" the EM field via transduction into a normal mode or elementary phonon compatible with the intrinsic design and length of the protein. This hypothesis suggests that displacement of electrons in the H-bonds that hold DNA together leading to DNA chain separation and initiating transcription are *reflections* of a phonon resonance/iterative process.

4.2. Signaling Proteins

How does all this work? In the case of Planaria the DNA in the totipotent stem cells created by the injury may be responding directly to the EM fields. DNA-mediated charge transport and the oxidative damage that results are extremely sensitive to variations in the sequence and conformational-adaptive response leading to stacking of the intervening bases [18]. Protein binding to DNA, for example, through one or more of the MAPKinase cascades, may modulates long-range charge transport negatively and positively depending upon the specific protein /DNA interactions in play [52,54].

Increased activation of the MAP-Kinase signaling pathways and the specific protein binding activities that normally occurs prior to upregulation of gene expression are increased by EMF [26,34,38,72]. Protein transcription factors in the p38 MAPK pathway are reported to be involved during both ELF and RF exposures [38]. Increased phosphorylation of specific transcription factors entering the nucleus, bind to specific regions of the recognition sites on the promoter and are essential for the initiation of transcription.

4.3. Potential Biomedical Applications

EM field exposures to induce hsp70 expression offer non-invasive methods to provide cytoprotection before, during and following surgical procedures or in areas of highly predictable trauma, e.g. combat, contact sports. In terms of potential biomedical applications of EM fields, it is intriguing to consider the data presented here together with our previous reports on cytoprotection and potential for gene therapy using a known specific DNA sequence that is responsive to EM fields, e.g. NGF, HSP70.

The stimulation of repair is a documented biological effect of EM fields [5]. However, some of the variability in results obtained may possibly be related to different responses to repair in different tissues, the exposure protocols employed and specific pulse parameters [29]. With modern lightweight designs prophylactic applications are technologically feasible, and could result in more rapid repair. Re-exposure at specific intervals would maintain the increased levels and provide increased protection.

Treatment with EM fields has been shown to protect and enhance injury repair in ischemia reperfusion injury [22] and enhanced regeneration of injured sciatic nerve, in both examples, *after* EM field exposure was discontinued [36]. Post-EM field exposure (60Hz, 80mG sine wave) of as little as 40 minutes, induces elevated hsp70 levels that were found to remain elevated for more than

3 hours and remained capable of re-stimulation to the same or higher levels using a higher or lower field strength [8,23,24]. Gordon [28,29] suggests that paramagnetic/diamagnetic dynamics in natively responsive elements generate quantum signal series that control conformational adaptation of proteins including DNA, enzymes and membrane proteins. He notes that identification of electromagnetic response elements in DNA was an important first insight and has proposed that DNA and especially promoter areas are highly responsive to these signal series. Dennis and Goodwin [19] examined PEMF technologies to define pulse bioefficacy and reported dB/dt or "rise time" as the critical determinant within the PEMF technologies they examined. They went on to note, "rectangular pulses with rapid dB/dt were up to four times more bio-effective in stimulating classes of genes associated with tissue restoration following trauma compared to DC, sine wave or millisecond designs". Our findings tend to corroborate that assessment, but also note the importance of specific frequencies within the parameters of our study.

4.4. Summary and Conclusions

In the experiments reported here, the flatworm Planaria *Dugesia dorotocethala* was used as a model system to assess whether frequencies that are multiples of eight induced regrowth and levels of stress response proteins (hsp70) quicker and with longer duration of effect when compared to a sinusoidal signal. There is good evidence, as previously suggested by Dennis and Goodwin [19] that the critical design determinant in pulsed electromagnetic field technologies in terms of bioefficacy is the dB/dt or "rise time" in such designs and that rise time bioefficacy could be based upon electromagnetically responsive elements present in proteins, which would imbue the protein with highly sophisticated abilities to select harmonics necessary for homeostasis. The significance of effect vs. efficacy is largely avoided among designers and investigators of PEMF devices. The failure to address this question has resulted in highly variable results and criticism that PEMF technology lacks "scientific basis". This paper is the first in an attempt to discuss and evaluate specific frequencies in the ELF-EMF range.

5. ACKNOWLEDGEMENT

Dedicated in loving memory to Abraham J Kremer and Glen A Gordon. We are grateful to Janet Wilson of Carolina Biologicals and Eve Vagg, Department of Photography and Illustration for their dedicated help.

REFERENCES

[1] K. Agata, (2003) Regeneration and gene regulation in planarians, Curr Opin Genet Dev, **13**, 492−496.

[2] K. Agata, Y. Soejima, K. Kato, C. Kobayashi, Y. Umesono, and K. Watanabe, (1998) Structure of the planarian central nervous system (CNS) revealed by neuronal cell markers, Zool Sci, **15**, 433−440.

[3] K. Agata and Y. Umesono, (2008) Brain regeneration from pluripotent stem cells in planarian, Phil. Trans. R. Soc. B, **363**, 2071−2078.

[4] A. Albertini, P. Zucchini, G. Noera, R. Cadossi, C. P. Napoleone, and A. Pierangeli, (1999) Protective effect of low frequency low energy pulsing electromagnetic fields on acute experimental myocardial infarcts in rats.

[5] J. Baguna and R. Romero, (1981) Quantitative analysis of cell types during growth, regrowth and regeneration in the planarians digesia mediterranea and dugesia tigrina, Hydrobiologia, **84**, 181−194.

[6] C. A. L. Bassett, (1995) Bioelectromagnetics in the service of medicine, Adv Chem, **250**, 261−276.

[7] J. P. Blanchard and C. F. Blackman, (1994) Clarification and amplication of an ion parametric resonance model for magnetic field interaction with cells, Bioelectromagnetics, **14**, 273−286.

[8] M. Blank and R. Goodman, (2007) A mechanism for stimulation of biosynthesis by electromagnetic fields: Charge transfer in DNA and base pair separation, J Cell Physiol doi10. 1002/jcp. 21198.

[9] M. Blank and R. Goodman, (2004) Initial interaction in electromagnetic field-induced biosynthesis, J Cell Physiol, **199**, 359−363.

[10] M. Blank and R. Goodman, (1997) Do electromagnetic fields interact directly with DNA? Bioelectromagnetics, **18**, 111−115.

[11] M. Blank and L. Soo, (2001) Electromagnetic acceleration of electron transfer reactions, J Cell Biochem, **81**, 278−283.

[12] D. J. Canaday and R. C. Lee, (1991) Scientific basis for clinical applications of electric fields in soft tissue repair, In Electromagnetics in Medicine. (C. Brighton and S. Pollack, Eds.), San Francsico Press, San Francisco, CA, 275−292.

[13] S. Carmody, X. L. Wu, H. Lin, M. Blank, H. Skopicki, and R. Goodman, (2000) Cytoprotection by electromagnetic field-induced hsp70: A model for clinical application, J Cell Biochem, **79**, 453−459.

[14] F. Cebria, T. Kudome, M. Nakazawa, K. Mineta, K. Ikeo, T. Gojobori, and K. Agata, (2002a) The expression of neural-specific genes reveals the structural and molecular complexity of the planarian central nervous system, Mech Dev, **116**, 199−204.

[15] F. Cebria, M. Nakazawa, K. Mineta, K. Ikeo, T. Gojobori, and K. Agata, (2002b) Dissecting planarian central nervous system regeneration by the expression of neural-specific genes, Dev Growth Differ, **44**, 135−146.

[16] K. Chang and W. R. Chang, (2003) Pulsed electromagnetic fields prevent osteoporosis in ovariectomized fe-

male rat model: A prostaglandin E2 associated process, Bioelectromagnetics, **24**, 189−198.

[17] K. C. Chou, (1988) Review: Low frequency collective motion in biomacromolecules and its biological functions, Biophysical Chemistry, **30**, 3−48.

[18] K. C. Chou, (1984) Low frequency vibration of DNA molecules, Biochemical Journal, **221**, 27−31.

[19] P. J. Dandliker, R. E. Holmlin, and J. K. Barton, (1997) Oxidative thymine repair in the DNA helix, Science, **275**, 1465−1468.

[20] R. Dennis and T. Goodwin, (2003) Physiological and molecular genetics effects of time-varying electromagnetic fields on human neuronal cells, NASA Technical Paper TP-2003−212054.

[21] A. L. DiCarlo, J. M. Farrell, and T. A Litovitz, (1999) Myocardial protection conferred by electromagnetic fields, Circulation, **99**, 813−816.

[22] C. Eichwald and J. Wallaczek, (1996) Activation dependent and biphasic electromagneetic field effects: Model based on cooperative enzyme kinetics in cellular signaling, Bioelectromagnetics, **17(6)**, 427−35.

[23] I. George, M. S. Geddis, Z. Lill, H. Lin, T. Gomez, M. Blank, M. C. Oz, and R. Goodman, (2008) Myocardial function improved by electromagnetic field induction of stress protein hsp70. J Cell Physiol DOI: 10. 1002/jcp 21461.

[24] R. Goodman and M. Blank, (2002) Insights into electromagnetic interaction mechanisms, J Cell Physiol, **192**, 16−22.

[25] R. Goodman and M. Blank, (1998) Magnetic field stress induces expression of hsp70, Cell Stress/Chaperones 3, 79−88.

[26] R. Goodman and A. S. Henderson, (1988) Exposure of salivary gland cells to low-frequency electromagnetic fields alters polypeptide synthesis, Proc Natl Acad Sci U S A, **85**, 3928−3932.

[27] R. Goodman, Y. A. Lin, M. Geddis, S. Hodge, S. Pantazatos, M. Blank, and R. Ambron, (2009) Electromagnetic fields activate the ERK cascade, increase hsp70 protein levels and promote regeneration in Planaria, International Journal of Radiation Biology, In Press.

[28] R. Goodman, D. Weisbrot, A. Uluc, and A. Henderson, (1992) Transcription in Drosophila melanogaster salivary gland cells is altered following exposure to low frequency electromagnetic fields: Analysis of chromosome 3R, Bioelectromagnetics, **13**, 111−118.

[29] G. Gordon, (2008) Extrinsic electromagnetic fields, low frequency (phonon) vibrations and control of cell function: A non-linear resonance system, J Biomed Sci and Engineering, **1**, 152−156.

[30] G. Gordon, (2007) Designed electromagnetic pulsed therapy: Clinical applications, J Cell Physiol, **212**, 579−582.

[31] L. Han, H. Lin, M. Head, M. Jin, M. Blank, and R. Goodman, (1998) Application of magnetic field-induced heat shock protein 70 for presurgical cytoprotection, J Cell Biochem, **71**, 577−583.

[32] H. Ito and C. A. Bassett, (1983) Effect of weak, pulsing electromagnetic fields on neural regeneration in the rat, Clin Orthop Relat Res, **181**, 283−290.

[33] K. A. Jenrow, C. H. Smith, and A. R. Liboff, (1996) Weak extremely low frequency magnetic field-induced regeneration anomalies in the planarian dugesia tigrina, Bioelectromagnetics, **17**, 467−474.

[34] K. A. Jenrow, C. H. Smith, and A. R. Liboff, (1995) Weak extremely low frequency magnetic fields and regeneration in the planarian dugesia tigrina, Bioelectromagnetics, **16**, 106−112.

[35] M. Jin, M. Blank, and R. Goodman, (2000) ERK1/2 phosphorylation, induced by electromagnetic fields, diminishes during neoplastic transformation, J Cell Biochem, **78**, 371−379.

[36] M. Jin, H. Lin, L. Han, M. Opler, S. Maurer, M. Blank, and R. Goodman, (1997) Biological and technical variables in *c-myc* expression in HL60 cells exposed to 60Hz electromagnetic fields, Bioelectrochem Bioenerg, **44**, 111− 120.

[37] M. Kanje, A. Rusovan, B. Sisken, and G. Lundborg, (1993) Pretreatment of rats with pulsed electromagnetic fields enhances regeneration of the sciatic nerve, Bioelectromagnetics, **14**, 353−359.

[38] V. V. Lednev, (1991) Possible mechanism for influence of magnetic fields on biological systems, Bioelectromagnetics, **12**, 71−75.

[39] D. Leszczynski, S. Joenvaara, J. Reivinen, and R. Kuokka, (2002) Non-thermal activation of the hsp27/ p38MAPK stress pathway by mobile phone radiation in human endothelial cells: molecular mechanism for cancer-and blood-brain barrier-related effects, Differentiation, **70**, 120−129.

[40] A. Liboff, (2004) Toward and electromagnetic paradigm for biology and medicine, Journal of Alternative and Complementary Medicine, **1**, 41−47.

[41] A. Liboff, (1985) Geomagnetic cyclotron resonance in membrane transport, J Biol Physics, **13**, 99−102.

[42] H. Lin, M. Blank, M. Head, and R. Goodman, (1999) A magnetic field-responsive domain in the human HSP70 promoter, J Cell Biochem, **75**, 170−176.

[43] H. Lin, M. Blank, K. R. Haseroth, and R. Goodman, (2001) Regulating genes with electromagnetic response elements, J Cell Biochem, **81**, 143−148.

[44] H. Lin, L. Han, M. Blank, M. Head, and R. Goodman, (1998a) Magnetic field activation of protein-DNA binding, J Cell Biochem, **70**, 297−303.

[45] H. Lin, M. Head, M. Blank, L. Han, M. Jin, R. Goodman, (1998b) Myc-mediated transactivation of HSP70 expression following exposure to magnetic fields, J Cell Biochem, **69**, 181−188.

[46] H. Lin, M. Opler, M. Head, M. Blank, and R. Goodman, (1997) Electromagnetic field exposure induces rapid, transitory heat shock factor activation in human cells, J Cell Biochem, **66**, 482–488.

[47] R. S. M. Fenn, R. Das, and P. A. B. Harbury, (2009) Re-measuring the double helix, Science, **322**, 449.

[48] R. I. Morimoto, (1998) Regulation of the heat shock transcriptional response: Cross talk between a family of heat shock factors, molecular chaperones and negative regulators, Genes & Development.

[49] W. J. O'Brien, H. M. Murray, and M. G. Orgel, (1984) Effects of pulsing electromagnet fields on nerve regeneration: Correlation of electrophysiologic and histochemical parameters in adult guinea pigs, J Bioelectricity, **3**, 33–40.

[50] M. G. Orgel, W. J. O'Brien, and H. M. Murray, (1984) Pulsing electromagnetic field therapy in nerve regeneration: an experimental study in the cat, Plast Reconstr Surg, **73**, 173–183.

[51] D. J. Panagopoulos, A. Karabarbounis, and L. H. Margaritis, (2002) Mechanism of action of electromagnetic fields on cells, Biochem Biophys Res Com, **298**, 95–102.

[52] A. R. Raji and R. E. Bowden, (1983) Effects of high-peak pulsed electromagnetic field on the degeneration and regeneration of the common peroneal nerve in rats, J Bone Joint Surg Br, **65**, 478–492.

[53] S. Rajski and J. K. Barton, (2001) How different DNA-binding proteins affect long-range-oxidated damage to DNA, Biochemistry, **40**, 5556–5564.

[54] S. Rao and A. S. Henderson, (1996) Regulation of c-fos is affected by electromagnetic fields, J Cell Biochem, **63**, 358–365.

[55] M. Ratner, (1999) Electronic motion in DNA, Nature, **397**, 480–481.

[56] E. Salo and J. Baguna, (1984) Regeneration and pattern formation in planarians, J Embryol, Exp Morphol, **83**, 63–80.

[57] A. S. Alvarado, (2006) Planarian regeneration: Its ending is its beginning, Cell, **124**, 241–245.

[58] A. A. Sanchez, P. A. Newmark, S. M. Robb, and R. Juste, (2002) The Schmidtea mediterranea database as a molecular resource for studying platyhelminths, stem cells and regeneration, Development, **129**, 5659–5665.

[59] A. A. Sanchez and Newmark, (1999) Double-stranded RNA specifically disrupts gene expression during planarian regeneration, Proceedings of the National Academy of Sciences, USA; Developmental Biology, **96(9)**, 5049–5054.

[60] A. A. Sanchez and P. A. Newmark, (1998) The use of planarians to dissect the molecular basis of metazoan regeneration, Wound Rep Reg, **6**, 413–420.

[61] N. Schwalb and F. Temps, (2008) Base sequence and higher-order structure induce the complex excited-state dynamics in DNA, Science, **322**, 243–245.

[62] J. M. Shallom, A. L. Di Carlo, D. Ko, L. M. Penafiel, A. Nakai, and T. A. Litovitz, (2002) Microwave exposure induces Hsp70 and confers protection against hypoxia in chick embryos, J Cell Biochem, **86**, 490–496.

[63] F. Shao, K. Augustyn, and J. K. Barton, (2005) Sequence dependence of charge transport through DNA domains, J Am Chem Soc, **127**, 17445–17452.

[64] B. F. Sisken, M. Kanje, G. Lundborg, E. Herbst, and W. Kurtz, (1989) Stimulation of rat sciatic nerve regeneration with pulsed electromagnetic fields, Brain Res, **485**, 309–316.

[65] B. F. Sisken, J. Walker, and M. Orgel, (1993) Prospects on clinical applications of electrical stimulation for nerve regeneration, J Cell Biochem, **51**, 404–409.

[66] J. L. Walker, J. M. Evans, P. Meade, P. Resig, and B. F. Sisken, (1994a) Gait-stance duration as a measure of injury and recovery in the rat sciatic nerve model, J Neurosci Methods, **52**, 47–52.

[67] J. L. Walker, J. M. Evans, P. Resig, S. Guarnieri, P. Meade, and B. F. Sisken, (1994b) Enhancement of functional recovery following a crush lesion to the rat sciatic nerve by exposure to pulsed electromagnetic fields, Exp Neurol, **125**, 302–305.

[68] M. Ubbink, M. Ejdeback, B. G. Karlsson, and D. S. Bendall, (1998) The structure of the complex of plastocyanin and cytochrome f, determined by paramagnetic NMR and restrained rigid-body molecular dynamics, Structure, **3**, 323–335.

[69] C. Wan, T. Fiebig, S. O. Kelley, C. R. Treadway, and J. K. Barton, (1999) Femtosecond dynamics of DNA mediated electron transfer, Proc Nat Acad Sci USA, **96**, 6014–6019.

[70] C. Wan, T. Fiebig, O. Schiemann, J. K. Barton, and A. H. Zewail, (2000) Femtosecond direct observation of charge transfer between bases in DNA, Proc Natl Acad Sci USA, **97**, 14052–14055.

[71] R. V. Weber, A. Navarro, J. K. Wu, H. L. Yu, and B. Strauch, (2004) Pulsed magnetic fields applied to a tranferred arterial loop support the rat groin composite flap, Plast Reconstr Surg, **114**, 1185–1189.

[72] D. Weisbrot, O. Khorkova, H. Lin, A. Henderson, and R. Goodman, (1993) The effect of low frequency electric and magnetic fields on gene expression in Saccharomyces cerevisiae, Bioelectrochem Bioenerg, **31**, 167–177.

[73] D. Weisbrot, H. Lin, L. Ye, M. Blank, and R. Goodman, (2003) Effects of mobile phone radiation on growth and development in Drosophila melanogaster, J Cell Biochem, **89**, 48–55.

J. Biomedical Science and Engineering, 2009, 2, 239-244 **JBiSE**
doi: 10.4236/jbise.2009.24037 Published Online August 2009 (http://www.SciRP.org/journal/jbise/).

Detection ischemic episodes from electrocardiogram signal using wavelet transform

Mohammad Karimi Moridani, Majid Pouladian

Biomedical Engineering Department, Science and Research Branch, Islamic Azad University, Tehran, Iran
Email: Karimi.m@srbiau.ac.ir

Received 19 November 2008; revised 16 March 2009; accepted 16 April 2009.

ABSTRACT

In this paper, we propose an algorithm for detection of myocardial ischemic episodes from electrocardiogram (ECG) signal using the wavelet transform technique. The algorithm was tested on data from the European ST-T change database. Results show that this algorithm is effective for distinguishing normal ECGs from ischemic. We developed a method that uses wavelets for extracting ECG patterns that are characteristic for myocardial ischemia.

Keywords: Myocardial Ischemic; Wavelet Transform; ECG

1. INTRODUCTION

The formulation and properties of an electrical impulse through the heart muscle result in time-varying potentials on the surface of the human body, which are known as the ECG signals. The signal represents various activities of the heart [1]. Wavelet Transformation (WT) has shown to be substantially noise-proof in ECG segmentation, and thus very appropriate for ST-T segment extraction (**Figure 1**). An initial downward deflection after the P-wave is termed as, 'Q', the dominant upward deflection is the 'R' and the terminal part is denoted as 'S'. The T-wave represents ventricular recovery or repolarization [1,2].

The ST segment usually merges smoothly and imperceptibly with the T-wave.

Having a simple estimate of whether an ECG recording which includes segments is characteristic for ischemic heart or not, is one of the most interesting topics for cardiologists.

Our aim in this research is to develop an algorithm using WT for identification of myocardial ischemic episodes.

2. METHOD

For ECG parameters estimation, it is desirable that the basis functions (wavelets), be symmetric/antisymmetric Asymmetric basis will enable to detect the extreme of wave's peak [4].

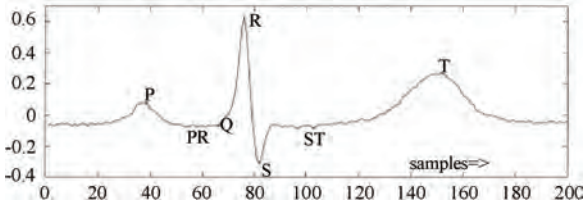

Figure 1. ECG waveform.

In case of antisymmetric basis, the peak of the wave is detected as a zero crossing.

In order to have a computationally simple analysis, the peaks should be detected as zero crossings (which is provided by antisymmetric basis) or local extreme (symmetric basis) [4]. It is also desirable that basis have a minimum number of sign changes. In practice, QRS complex is usually considered to be symmetrical, while T wave is less so. However, it has been shown, PR and ST points can be estimated using biorthogonal wavelets under the assumption of QRS complex and T wave symmetry [2]. Moreover, having as an aim proposed quantitative analysis, it is quite plausible to suppose basic QRS complex and T wave symmetry [4]. Biorthogonal wavelets satisfy both these properties, so they are used for DWT (discrete wavelet transform) decomposition. Hence used in this work. The filter coefficients of both the symmetric low pass (LP) H and the antisymmetric high pass (HP) filters G and K are given in Table 1 [2]. Decomposition and reconstruction filters satisfy further equations:

$$|H(w)|^2 + G(w)K(w) = 1 \quad (1)$$

where, w is frequency

$$H(w) = e^{iw2}(\cos(w/2))^p \quad (2)$$

$$G(w) = 4ie^{iw2}\sin(w/2) \quad (3)$$

$$K(w)=\frac{1-|H(w)|^2}{G(w)} \quad (4)$$

$$i=\sqrt{-1} \quad \text{and p=3,5,7,…}$$

For compact support '*p*' should be as small as possible. Hence, it was chosen to be equal to 3. The filter coefficients corresponding to *p*=3 are given in **Table 1**.

2.1. Parameters Estimation

The parameters of the ECG signal are obtained by the wavelet decomposition dyadic tree. This tree decomposes the signal initially into the smooth (low pass) and detail (high pass) constituents [1]. The low pass component is further decomposed into low pass and high pass. This process is repeated over the desired number of scales. When an ECG signal is passed through each of the wavelet filters whose scales range from 21 to 24, as shown in **Figure 2**, the detailed *d*1, *k*, *d*2 ,*k*, *d*3, *k d*4, *k* and the smooth *s*1, *k*, *s*2, *k*, *s*3, *k*, *s*4, *k* filtered outputs are obtained as shown in **Figure 3**. The following algorithm is suggested for estimating the said ECG parameters [1].

This initial filter is also based upon WT. The denoising procedure is performed in three steps (MATLAB wavelet toolbox) [2]:

1) decomposition with sym8 wavelet at level 5,

2) detailed coefficients threshold- choosing a threshold for each level,

3) reconstruction.

In order to obtain ST and PR points' values, each decomposed ECG is segmented (**Figure 1**). At the first and the second levels, QRS starting, ending and peak point are extracted. Let us denote as n_R -the R peak point, nl, and n, 2 the beginning and ending points of QRS complex respectively [2]. PR point is thus calculated as:

$$PRpo\,\text{int}=n_R-\frac{n_{l2}-n_{l1}}{2} \quad (5)$$

At the fourth level, ST-T characteristic points are obtained: n_T - the T peak point, nt1 and nt2 the beginning and ending points of T wave, respectively [1]. ST point is calculated as:

$$STpo\,\text{int}=n_T-\frac{n_{l2}-n_{l1}}{2} \quad (6)$$

Wavelet decomposition introduces scale-dependent phase delay into signals. For example, each zero crossing point which corresponds to the peak of a symmetric uniphase wave is delayed for exactly $2^{J-1}-1$ points, where represents the scale [1].

Table 1. Filter coefficients of symmetric Low Pass (LP), antisymmetric High Pass (HP) and their reconstruction filters.

H	G	K	L
0.1768	0.3536	0.1768	-0.3536
0.5303	1.0607	-0.5303	1.0607
0.5303	-1.0607	0.5303	1.0607
0.1768	-0.3536	-0.1768	-0.3536

G, decomposition high pass filter coefficients; H, decomposition low pass filter coefficients; K, reconstruction high pass filter coefficients; L, reconstruction low pass filter coefficients.

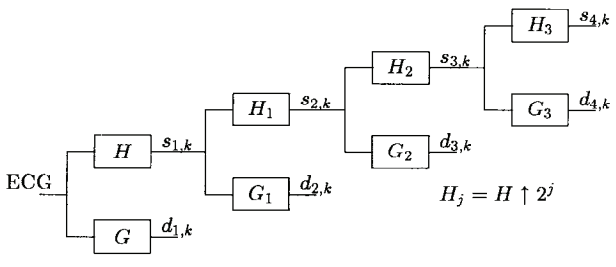

Figure 2. Wavelet decomposition of ECG signal. Decomposition per-formed over 4 scales.

2.2. ST Deviation Analysis

In our analysis, we have used European ST-T change database with ischemic ECG signals sampled at 250 Hz, two hours in duration each. The most elementary differentiate/threshold algorithm has been applied to extract each beat. Obtained signals were decomposed as described in section 2.1 and for each beat/separate signal, an ST deviation value was calculated as [2]:

$$STdeviation = \left|ECGvalue(PRpo\,\text{int})-ECGvalue(STpo\,\text{int})\right| \quad (7)$$

where ECG value(x) denotes an amplitude at the point x of a given ECG.

Cases with specific ECG beats, that is to say with indistinguishable ECG features (thus impossible segmentation), were excluded from further analysis. In this way, an ST deviation value was obtained for each beat that could be analyzed [2]. The final report might include the comment that some beats were excluded from analysis as well as the number of the beats omitted, and therefore suggest a manual observation where required [2].

2.3. QRS Onset and Offset Detection

Some of the existing techniques use a series of bandpass filters to extract *QRS* complexes from the ECG signal, which under severe baseline drift and other high frequency noises, fails to detect the characteristic points to an acceptable accuracy. And some techniques use neural network based adaptive identification algorithms [3,5], which can be used for only a particular type of pattern. The wavelet transform based technique can be used to identify the characteristic points of the ECG signal to a fairly good accuracy, even with the presence of severe high frequency and low frequency noises [6,7,8]. Our aim is to describe an elegant algorithm, which uses

WT to identify the characteristic points of the ECG signal, and identifying the myocardial ischemic episodes.

As an alternative to the normal filtering techniques, which use different narrow-band filters to extract the frequency contents of the signal, wavelet transform technique can be used [3]. In wavelet transform technique, the signal is analyzed at different frequencies with different resolutions. It is called multi resolution analysis (MRA) (**Figure 4**).

The wavelet used in this work is the quadratic spline wavelet [9]. The reasons for choosing this particular wavelet for the analysis purpose are as follows:

It has a very compact support and a generalized linear phase, so there is a determinate relationship between ECG characteristic points and the modulus maxima, or the zero-crossing points of the WTs.

The Fourier transform (FT) of the quadratic spline wavelet is given as:

$$\varphi(w) = iw\left(\frac{\sin\frac{w}{4}}{\frac{w}{4}}\right)^4 \quad (8)$$

The FIR(Finite Impulse Response) filter coefficients that make up the decomposition and reconstruction filter banks and the Lipschitz coefficients for the decomposition algorithm are given in **Tables 2 and 3** [3].

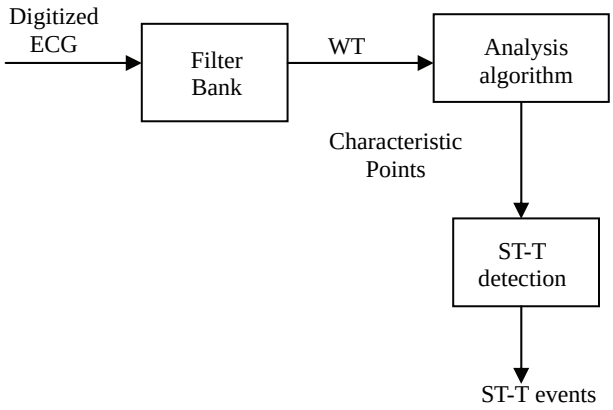

Figure 4. Block diagram of the entire process.

Table 2. FIR filter coefficients for quadratic spline wavelet.

N	*H*	*G*	*K*	*L*
-3			0.0078125	0.0078125
-2			0.054685	0.046875
-1	0.125		0171875	0.1171875
0	0.375	-2.0	-0.171875	0.65625
1	0.375	2.0	-0.054685	0.1171875
2	0.125		-0.0078125	0.046875
3				0.0078125

G, decomposition High Pass filter coefficient; H, decomposition Low Pass filter coefficients; K, reconstruction High Pass filter coefficients; L, reconstruction Low Pass filter coefficients.

Table 3. Normalization coefficients λ_j for the quadratic spline wavelet.

j	λ_j
1	1.5
2	1.12
3	1.03
4	1..01
5	1.00

There is a relation between the characteristic points of the signal and their WT at different levels [10,11,12]. For example, for the wave in **Figure 5**, the wavelet transform at scale 2^1 is given.

The wave's rising edge corresponds to a negative minima and the dropping edge corresponds to a positive maxima. The moduli of these maxima or minima corresponding to the same edge are named as the modulus maxima line. If the uniphase wave is symmetric to its peak, then its peak corresponds to the zero-crossing point of the positive maxima negative minima pair with a delay of exactly $2^{J-1}-1$ points, where *j* represents the scale [3]. After obtaining the wavelet transform coefficients at different scales, the next step is to find out the ECG characteristic points from these coefficients [3].

2.4. T and P Wave Detection

T and *P* waves are normally low frequency, so WT at high scale is used to locate these waves. In this work, WT up to four scales are taken and the scale 2^4 is used to locate *T* and *P* waves.

T wave creates a pair of modulus maxima with a different sign on *W2jf* (*n*) at scale, 2^4 within a time window after the detected *R*-peak [3]. Since the wave is almost symmetric to its peak, the peak of *T*-wave corresponds to the zero crossing point of the modulus maximum pair with a delay of 2^{4-1}-1 points. The peak, onset and offset of the *P*-wave are detected in a way similar to those of the *T* before the detected *R*-wave [3].

2.5. R-peak Detection

For detecting the *R*-peak, the modulus maxima–minima pair is located at lowest scale, which is done by fixing a threshold for detection [13]. So maxima–minima pairs for other scales are located within the neighborhood of these maxima-minima pairs. If the amplitudes of the maxima-minima pairs, compared to those are at lower scale, are consistent or increasing, the corresponding

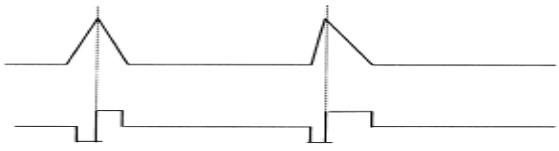

Figure 5. The uniphase wave and its WT at scale 2^1.

modulus maxima-minima pair is treated as one that corresponds to a true *R*-peak [3]. This method reduces the effect of low frequency artifacts and also the high frequency non morphological noise.

2.6. Detection of MI from the ECG Characteristic Point

Different ECG changes related to the evolution of ischemia have been described, including *T*-wave amplitude changes, *ST* deviations and even alterations in the terminal portion of the *QRS* complex [13]. Using global representations for the *ST–T* complex instead of a single point from the *ST* segment could better characterizes ischemia patterns and yield better identification of occluded artery [14,15]. The most important ECG change associated with ischemia is the *ST* segment elevation or depression, with depression being most common. Also, this can be along with *T*-wave amplitude changes or even inversion [3]. So ischemia can be detected using these two measurements. For finding the *ST* depression level, a reference level is found out at first. This is done by drawing a line between two or more *P*-waves where they return to the base line (or starting of *P*-wave). From the characteristic point detection algorithm, we obtain the *P*-wave onset and offset of all the cardiac cycles. *ST*-segment is the segment of ECG between *QRS* offset and *T*-wave onset. The deviation of this segment from the reference line is found out. The amplitude of *T*-wave is also found by measuring the distance between *T*-peak and reference line [3]. Having obtained these two values, we can come to a conclusion, that whether the cardiac cycle contains an ischemic episode or not.

3. INTERPRETING THE DATA

Two or more ST change episodes could be separated by insignificant time gaps or with an unreadable ECG segment. This could lead to the conclusion that these episodes are separate, which is scarcely the case. Since the duration of the episodes are of great importance for making conclusions about myocardial ischemia, it was necessary to alleviate such shortcomings [2]. Thus we applied a low pass filter (Chebyshev Type I filter) to the latter signal; thereby, constructed an envelope which was informative enough [2].

Figure 6 shows typical results from the readings in a patient with myocardial ischemia (manifested through T-and ST-wave change) [2]. High values at vertical axis suggest that a long ischemic episode has occurred (A part, **Figure 6**). Within normal ECGs, we expect that these values gather near zero. B part at **Figure 6** is a direct consequence of final low pass filtering and suggests that a series of shorter, but still significant, ST episodes have occurred with unsubstantial time gaps among them. B parts are not expected with normal ECGs. Negative ordinate values are a co product of LP filtering and bare no practical significance [2]. Beside ECG analyzed in **Figure 6** which we considered to be a mid-case in the terms of number of ST deviations, we selected two more examples in order to demonstrate the efficiency of the algorithm.

Figure 7 presents performance of the algorithm in the case where there were only few ST changes, while **Figure 8**.

In **Figure 7,** we can clearly see that vertical axis values are smaller, compared to those in **Figure 6** or **Figure 8**. Moreover, there are less high-valued ripples, and they occur with significant time gaps. This suggests that analyzed ECG is near normal in the terms of ST change [2].

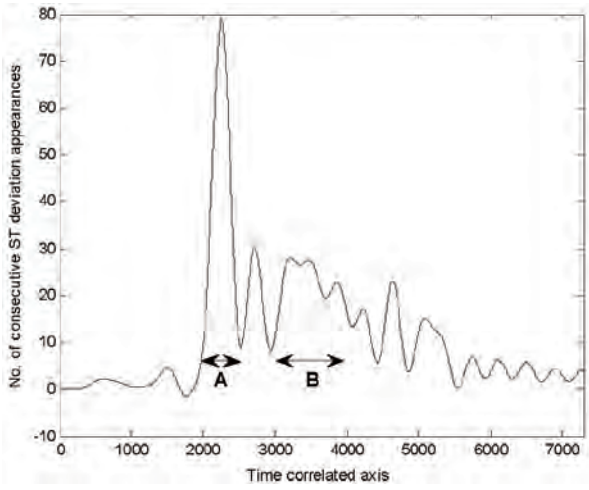

Figure 6. Number of ST deviations correlated with time of consecutive appearances-function's envelope.

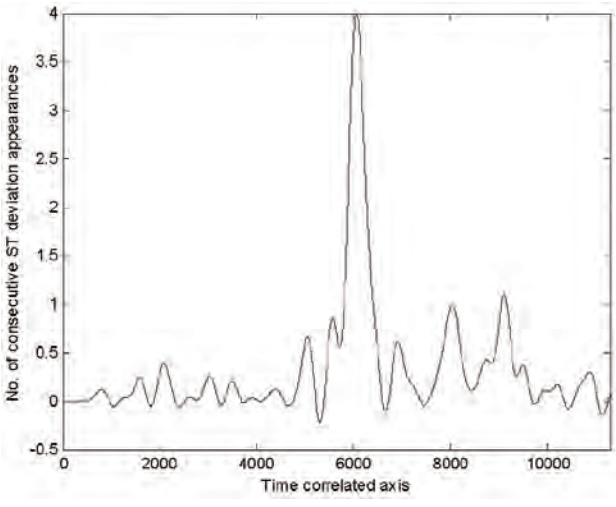

Figure 7. Number of ST deviations correlated with time of consecutive appearances-case with few ST-T deviations. (file e115. dat in has been analyzed) [4].

3.1. Estimating Algorithm's Efficiency

Annotation files provided for ST-T change ECG signals in contain information about ST and T-wave deviations as well as the number of heart beat in that particular ECG at which a change occurred [4]. ST changes are annotated by values '18' and T-wave changes by '19'.

In order to demonstrate similarity which exists between the algorithm's outcome and manually annotated ST-T changes, in **Figure 6** and **Figure 7** we present the manually annotated change/time dependence for the same ECGs analyzed in **Figure 7** and **Figure 8**, respectively [2].

Comparing **Figure 7** and **Figure 9**, as well as **Figure 8** and **Figure 10,** it shows the strong correlation between automatic and manual ECG analysis. Direct relationship exists between the time axes, too, but the algorithm's outcome 'compresses' time axis due to the nature of the constructed array whose envelope is the actual final result [2].

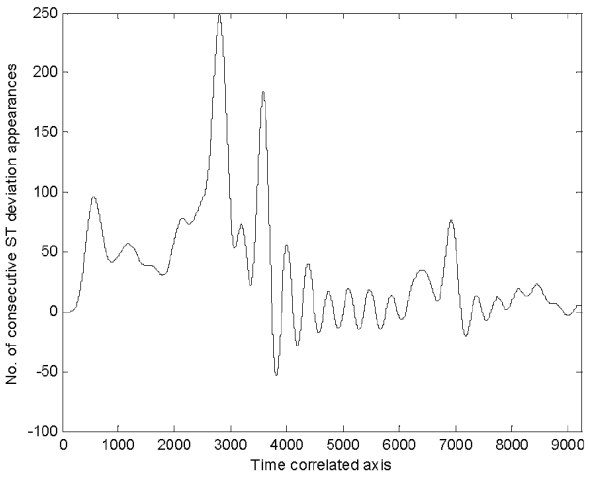

Figure 8. Number of ST deviations correlated with time of consecutive appearances-case with a considerable number of ST-T deviations. (file E121.dat in has been analyzed) [4].

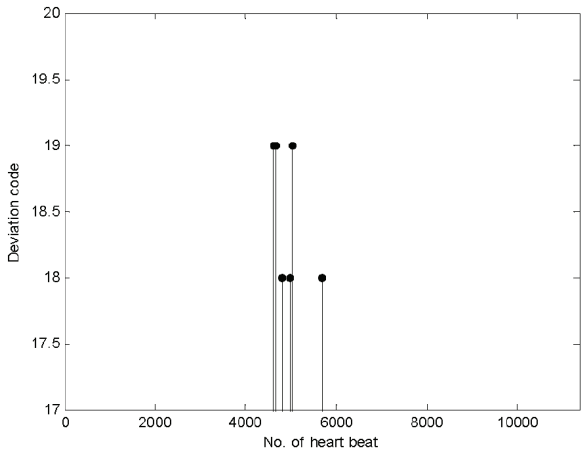

Figure 9. Manually annotated ST-T changes which correspond to **Figure 7**. (file e115.atr in has been used) [4].

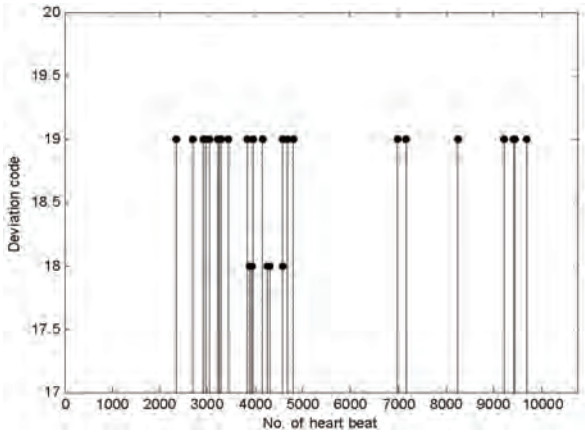

Figure 10. Manually annotated ST-T changes which correspond to **Figure 4**. (file e115.atr in has been used) [4].

After such analysis, a physician can examine those parts of ECG which were annotated for ST changes, if necessary. Performance on annotating ST changes of the proposed algorithm is the same as of, although different wavelet base function had been used [2]. Demonstrated performance has been verified on 10 ECGs from, and confirms already described relationship between ECGs automatically and manually analyzed for the stated purpose [4].

4. RESULT

An array of ST deviations was transformed into an array which correlates number of ST deviations with time of consecutive appearances [2] to show that the algorithm counts the number of consecutive appearances of ST deviations greater than 0. l mV and uses that number as a new array's element. The procedure is repeated for each ST change episode.

ST–T change detection algorithm consists of calculating certain performance indices. They are: *ST* sensitivity (ST_{se}), which is an estimation of the likelihood between detecting an ischemic *ST* episode; *ST* positive predictivity (*ST* + *P*), an estimation of the likelihood that a detection is a true ischemic *ST* episode; ischemic sensitivity (IS_{se}), which is a fraction of true ischemia, and ischemic positive predictivity (*IS* + *P*), which is the fraction of detector annotated ischemia, and is true ischemia [3,16].

5. CONCLUSIONS

In this paper, we proposed an algorithm for the detection of myocardial ischemic episodes from electrocardiogram (ECG) signal using the wavelet transform technique.

The study is mainly aimed to use biorthogonal wavelets to estimate clinically significant parameters of ECG waveforms and find out ST-T segment for detection ischemic episodes. Comparing the measured ST and the normal ST in test ECG provided by European ST data-

base, the algorithm could found the exactly time, that ST shape is changed into an abnormal shape. ST segment is the most important diagnostic parameter to finding myocardial ischemia therefore developed algorithm best coincidence with the database occurs in the determination of the beginning of the ST episodes, and the worst in the calculation of the maximum deviation. Nevertheless, this parameter is just used in the description of ischemia episodes, and its importance is relatively low with respect to the quantification of the number of episodes and their duration.

REFERENCES

[1] N. Sivannarayana, D. C. Reddy, (1999) Biorthogonal wavelet transforms for ECG parameters estimation, 167−174.

[2] N. Milosavljevic and A. Petrovic, (2006) ST segment change detection by means of wavelets, 137−140.

[3] P. Ranjith, P. C. Baby, and P. Joseph, (2003) ECG analysis using wavelet transform: application to myocardial ischemia detection, 44−47.

[4] "European ST-T change database," www. physionet.org.

[5] N. Magaveras, T. Stamkopoulos, C. Pappas, and M. G. Strintzis, (1998) An adaptive backpropagation neural network for real-time ischemia episodes detection: Development and performance analysis using the European ST-T database, IEEE Trans Biomed Eng, **45**, 805−13.

[6] M. Vetterly and J. Kovacevic, (1995) Wavelet and subband coding, First Edition, Upper Saddle River, NJ: Prentice Hall.

[7] M. R. Raghuveer and S. Bopardikar, (1996) Wavelet transforms: Introduction to theory and applications, Second Edition, Boston, MA: Addison Wesley.

[8] (1996) Special issue on wavelets, Proc IEEE, **84(4)**.

[9] S. Mallat and S. Zhong, (1992) Characterization of signals from multiscale edges, IEEE Trans PAMI, **14(7)**.

[10] C. Li, C. Zheng, and C. Tai, (1995) Detection of ECG characteristic points using wavelet transform, IEEE Trans Biomed Eng, **42(1)**, 8−21.

[11] D. P. Golden, R. A. Wolthuis, and G. W. Hoffler, (1973) A spectral analysis of the normal resting electrocardiogram, IEEE Trans Biomed Eng, **20(5)**, 366−72.

[12] S. Mallat, (1991) Zero crossing of a wavelet transform, IEEE Trans Inf Theory, **37(4)**.

[13] P. F. Cohn, (1993) Silent myocardial ischemia and infarction, 8–18, NewYork: Marcel Dekker, 87−97.

[14] F. Jager, G. B. Moody, and R. G. Mark, (1998) Detection of transient ST segment episodes during ambulatory ECG monitoring, Comput Biomed Res, **31(5)**, 305−22.

[15] J. Garcia, L Sornmo, S. Olmos, P. Laguna, (2000) Automatic detection of ST–T complex changes on the ECG using filtered RMS difference series: Application to ambulatory ischemia monitoring, IEEE Trans Biomed Eng; **47(9)**, 1195−201.

[16] F. Jager, G. B. Moody, A. Taddei, R. G. Mark, (1991) Performance measures for algorithms to detect transient ischemic ST segment changes. Computers in Cardiology, Los Alamitos, CA: IEEE Computer Society Press, 372−96.

J. Biomedical Science and Engineering, 2009, 2, 245-253 **JBiSE**
doi: 10.4236/jbise.2009.24038 Published Online August 2009 (http://www.SciRP.org/journal/jbise/).

Preparation and properties of cast polyurethane elastomers with molecularly uniform hard segments based on 2,4-toluene diisocyanate and 3,5-dimethyl-thioltoluenediamine

Xiao-Dong Chen[*1,2], Nan-Qiao Zhou[1], Hai Zhang[2]

[1]National Engineering Research Center of Novel Equipment for Polymer Processing, The Key Laboratory of Polymer Processing Engineering Ministry of Education, South China University of Technology, Guangzhou, 510640, China; [2]GuangZhou SCUT Bestry Technology Joint-stock Co., Ltd., South China University of Technology, Guangzhou, 510640, China
Email: cxdzlgzhnlg2003@163.com

Received 16 December 2008; revised 2 March 2009; accepted 5 March 2009.

ABSTRACT

A series of three cast polyurethane elastomers were prepared from 2,4-toluene diisocyanate (TDI) and 3,5-dimethyl-thioltoluenediamine (D MTDA) chain extender, with polyethylene adipate (PEA), polyoxytetramethylene glycol (PTMG) and polycaprolactone (PCL) soft segments. The polyol molecular weights employed was 2000g/mol. The polyurethane elastomers were characterized by an electronmechanical universal testing machine, an Akron abrasion loss tester, a LX-A Shore durometer, a rebound resilience equipment and a Dynamic- Mechanical analyzer. In addition, fractured surface of the polyurethane elastomers was investigated by a field emission scanning electron microscopy (SEM). The test results showed the PCL based elastomer exhibits the excellent tear and stress-strain properties that polyester based elastomers offer, while retaining superior compression set and resilience similar to polyether based elastomers. The static and dynamic properties of the PCL based elastomer were more suitable for dynamic applications. The SEM micrographs of all polyurethane samples indicated the existing of the microphase separation structure. Particles of the dispersed phase formed by the hard phase and crystalline part of the soft phase grows bigger with the increasing crystallinity of the soft segments. The hard domains are irregular shapes and with the sizes of a few micrometers.

Keywords: Soft Segment; Structure; Cast Polyurethane Elastomer; Properties

1. INTRODUCTION

In the recent decades, polyurethane elastomers have been successfully employed in a growing variety of uses and applications, due to their broad range of outstanding properties [1,2,3,4,5,6,7,8,9,10,11,12]. The polyurethane elastomers are composed of short, alternating polydisperse blocks of soft and hard segments. The soft segments with a low glass transition temperature are formed generally from polyethers or polyesters, generally of molecular weight 400-5000. The rigid, polar hard segments with a high glass transition temperature are based on diisocyanates and low-molecular-weight chain extenders [6,13,14,15,16,17,18,19,20,21,22,23,24,25,26,27].

Because there exists a degree of thermodynamic immiscibility between the hard urethane segments and the soft polyol segments, polyurethane elastomers exhibit microphase separation, which could result in a structure that can be considered as hard segment domains dispersed in a soft segment matrix [6,13,21,25,27,28,29,30, 31,32]. The resultant two-phase micro-domain structure exhibited by polyurethane elastomers is responsible for their superior mechanical properties. Usually, microphase separation is incomplete and the hard and soft segment phases still contain certain amounts of the other segment. The mean domain size increases from 10 to 20 nm as the hard segment content increases and the shapes of hard domains are in the form of spheres 5-20 nm, or long needles 5 nm thick and 50-300 nm long [6,14].

The two-phase micro-domain structure is greatly influenced by the molecular structure of the diisocyanate, polyol, and chain extender [13,14,33,34], by the ratio of hard segment and soft segment components [35], by the average segment length employed (including molecular weight distribution) [13], by the crosslinking density [18], and by the thermal history of the material [36]. Processing conditions, such as temperature, can also

change the domain structure significantly [37]. Some researchers have employed many characterization techniques to understand the relationship between the chemical architecture, morphology, and chemical properties [37,38]. It is well known that the size, shape, and structure of the hard-segment and soft-segment domains play a crucial role in determination of macroscopic properties [34,39]. Therefore, static and dynamic properties of polyurethane elastomers can be tailored by selecting different diisocyanates, polyols and chain extenders, or by simply varying the processing temperature [40].

In this study, a series of polyurethane elastomers based on polyethylene adipate (PEA), polyoxytetramethylene glycol (PTMG) and polycaprolactone (PCL) with molecular weight of 2000 as soft segments and hard segments based on the combination of 2,4-toluene diisocyanate and 3,5-dimethyl-thioltoluenediamine. In addition to general mechanical properties, resistance to thermal degradation, abrasion and dynamic properties were investigated, and the micro-phase structure images of samples were observed and captured by a Field Emission Scanning Electron Microscope (FE-SEM). The relationship between micro-phase structure and macroscopic properties was discussed. These key engineering properties are considered essential and the obtained results will provide foundation for the formula and structure design of the compounds for various applications, especially for high-loading dynamic applications.

2. EXPERIMENTAL

2.1. Materials

PEA was obtained form JingXing Polyurethane Co., Ltd. (WuXi, China). PTMG was produced by Mitsubishi Chemical Co., Ltd, Nippon. PCL was purchased from Dow Chemical, USA. The three polyols should be dehydrated in vacuum at 100~110°C for 2 hours before use and their values were described in detail in **Table 1.** 2,4-toluene diisocyanate, purchased from Qingdao Yutian Chemical Company, was imported in original package and used as received. The chain extender, 3,5-dimethyl-thioltoluenediamine, was purchased Albemarle Company and should be purified by dehydrated in vacuum at 80℃ for 1 night before use. Dibutyltin dilaurate (DBTDL) was acquired from Atofina Chemicals.

2.2. Preparation of Polyurethane Elastomers

Traditionally, polyurethane elastomers can be synthesized via a “one-shot” process or prepolymer method. While the one-shot process is the quickest and easiest of the manufacturing techniques, preparation via the prepolymer method imparts greater control over the chemistry of the reaction, influencing the structure, mechanical properties, reactivity and processability of the finished product [41,42]. In this study, the prepolymer method was used. The first stage involves preparation of a prepolymer from the polyol in excess diisocyanate to produce an isocyanate-terminated molecule. Subsequent reaction of the prepolymer with a diol or diamine chain extender constitutes the second stage, which produces a multi-block copolymer.

2.2.1. First Stage: Preparation of Prepolymer

2,4-toluene diisocyanate (0.83mol, 145g) was added into a 4-necked round bottom-boiling flask equipped with an overhead mechanical stirring unit, a thermometer and a vacuum take-off/nitrogen inlet. A polyol (0.37mol, 740g) was melted in an oven and added to TDI with stirring and reacted at 80 °C for 2 h under a nitrogen atmosphere to give a polyurethane prepolymer as a viscous liquid. And the prepolymer was examined for NCO content by using a standard method of n-butyl amine titration.

Table 1. Specifications of the three polyols.

Polyols	Molecular structure of the polyol	Hydroxyl value, mgKOH/g	Acid value, mgKOH/g	Molecular weight
PEA	HO-[-CH_2-CH_2-OOC-$(CH_2)_4$-COO-]$_n$-CH_2-CH_2-OH	56	≤0.5	2000
PTMG	HO-(-CH_2-CH_2-CH_2-CH_2-O-)$_n$-H	56	≤0.02	2000
PCL	HO-[-$(CH_2)_5$COO-]$_m$-R-[-OOC$(CH_2)_5$-]$_n$-OH	56	≤0.05	2000

Table 2. Mechanical properties of elastomers based on different backbones.

Properties	PEA-TDI	PCL-TDI	PTMG-TDI
100% Modulus, MPa	4.05	3.76	2.3
300% Modulus, MPa	12.15	10.43	3.7
Tensile Strength, MPa	51.15	44.09	29.86
Elongation at break,%	468	438	380
Tear Strength, KN/m	69	61	52
Compression Set, %	5.6	4	4.4
Rebound, %	32	41	44
Hardness, Shore A	77	77	78

2.2.2. Second Stage: Synthesis of Polyurethane

The obtained prepolymer (200g) was heated to 80℃ under vacuum (<2 mm Hg). The chain extender (21g) was added to the prepolymer. The resultant mixture was stirred at high speed for 60 seconds. If time permitting, the mixture should be degassed (for 1-2 min) to remove the air introduced by stirring. Then the mixture was poured into a pre-heated mold (110℃). The bubbles on the surface can be removed by sweeping it with a burner flame or with a stream of hot air, what can make the bubbles expanded and bursted. The mold was cured in a vented oven at 110℃ for 30 minutes. The polymer sheets were demolded and post-cured at an elevated temperature (for 12-16h at 110℃). The parts were stored at ambient temperature for 1 month. During this period, secondary chemical reactions should be completely and the microstructure would become established. This is very important for testing the dynamic properties.

2.3. Characteristics

The tensile strength and elongation at break were determined with an electronmechanical universal testing machine (INSTRON Co. LTD, Model 5566, USA). The abrasion resistance was performed with an Akron abrasion loss tester. The hardness was tested with a LX-A Shore durometer according to standard method (ISO 48-1984). The resilience was measured by a rebound resilience equipment (CJ-6A, ShangHai fourth chemical machine factory). The dynamic mechanical analysis was carried out in an air atmosphere by means of a NETZSCH Instrument, Dynamic-Mechanical Analyzer DMA242, on samples of following sizes: 2.0×5.8×10.0mm. The tests at 10 Hz frequencies, ±2N maximum dynamic stress, ±40μm maximum deformation amplitude and the temperature range of -100～150℃, with a heating rate of 5℃/min were accomplished. Fractographs were observed with a Field emission scanning electron microscopy (FE-SEM, Philips XL30 ESEM-FEG). Samples were prepared by tearing brittle samples (0.5mm thick) at low temperature by immerging in liquefied nitrogen. All samples were coated with a layer of gold or platinum before characterization.

3. RESULTS AND DISCUSSION

3.1. Influence of the Polyol Structure on the Mechanical Properties of Polyurethane Elastomers

Table 2 reports a list of some general mechanical properties of a series of the polyurethane elastomers based on PEA, PTMG and PCL as soft segments and hard segments based on the combination of 2,4-toluene diisocyanate and 3,5-dimethyl-thioltoluenediamine. The PEA based elastomer had better tensile strength and elongation, and much better tear resistance compared to the PTMG based elastomer. However, its compression set and resilience were inferior to the PTMG based elastomer. Interestingly, the PCL based elastomer offered very competitive stress-strain properties and tear resistance when compared with the PEA based elastomer, while significantly improved compression set and resilience over the PEA based elastomer. Its ability to retain elastic properties after prolonged compressive stresses was as good as the PTMG based elastomer, while its resilience performance was close to that of the PTMG based elastomer. From the testing data shown in **Table 2**, it is clear that the PCL based elastomer possesses more balanced properties. It exhibits the excellent tear and stress-strain properties that polyester based elastomers offer, while retaining superior compression set and resilience similar to polyether based elastomers.

3.2. Influence of the Polyol Structure on the Phase Morphology of Polyurethane Elastomers

The SEM method was employed to investigate the morphology of fractured surface of the polyurethane elastomers. As shown in the presented images (**Figures 1−3**), microphase separation can be observed for all polyurethane samples tested. A continuous phase is visible in SEM micrographs, which is created by the amorphous part of the soft phase and the intermediate phase, i.e., the so-called matrix. Particles of the dispersed phase are encapsulated in that matrix. They are formed by the hard phase and the crystalline part of the soft phase. Three principal thermodynamic factors contribute to the formation of that phase structure: mobility of hard segments, viscosity of the system, and interactions between hard segments [14].

The hard phase and the crystalline part of the soft phase form the so-called domains with irregular shapes and with the sizes of a few micrometers. The size of the domains is mainly dependent on its content of rigid segments and the crystallinity of soft phase, which is clearly visible for the three samples. The soft phase is amorphous in some cases (**Figure 2**). A small number of tiny particles composed of rigid segments can be observed in the fractured surface only. Crystallization of the soft phase causes the domains bigger in case of the PEA based elastomer (**Figure 1**) and PCL based elastomer (**Figure 3**). The particle size of the dispersed phase grows bigger with the increasing crystallinity of the soft segments. At the same time, the intermediate phase interface of the PCL based elastomer is much smoother than that of the PEA based elastomer due to its lower degree of crystallinity and less regular arrangement of soft segments. It should be noticed that there are some scratches and cracks in the surface of the PCL based elastomer (**Figure 3**). We obtained an explanation that the PCL based elastomer had been exposed under

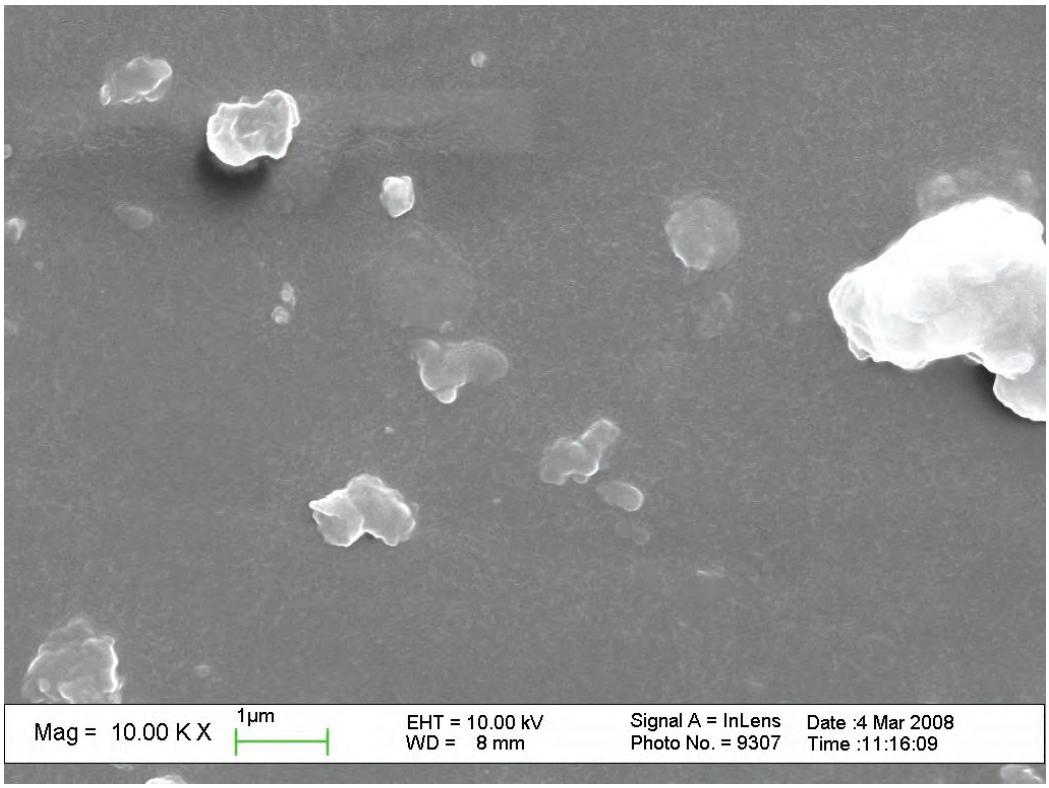

Figure 1. Scanning electron micrograph of the PEA based elastomer.

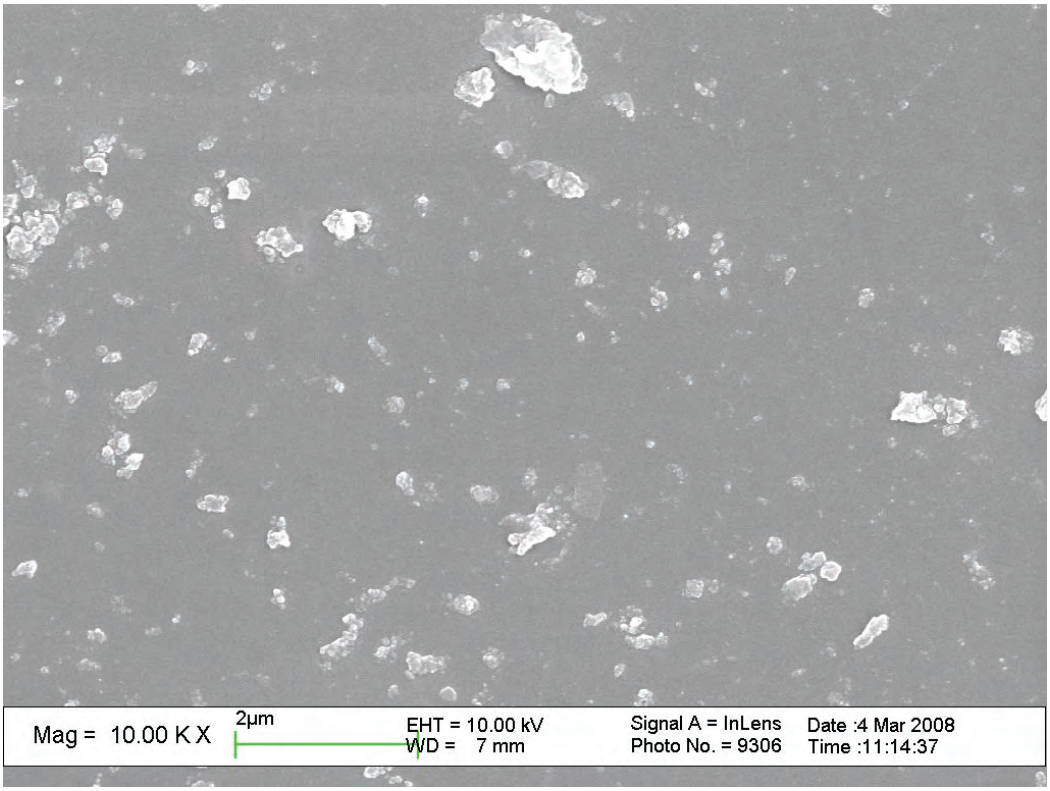

Figure 2. Scanning electron micrograph of the PTMG based elastomer

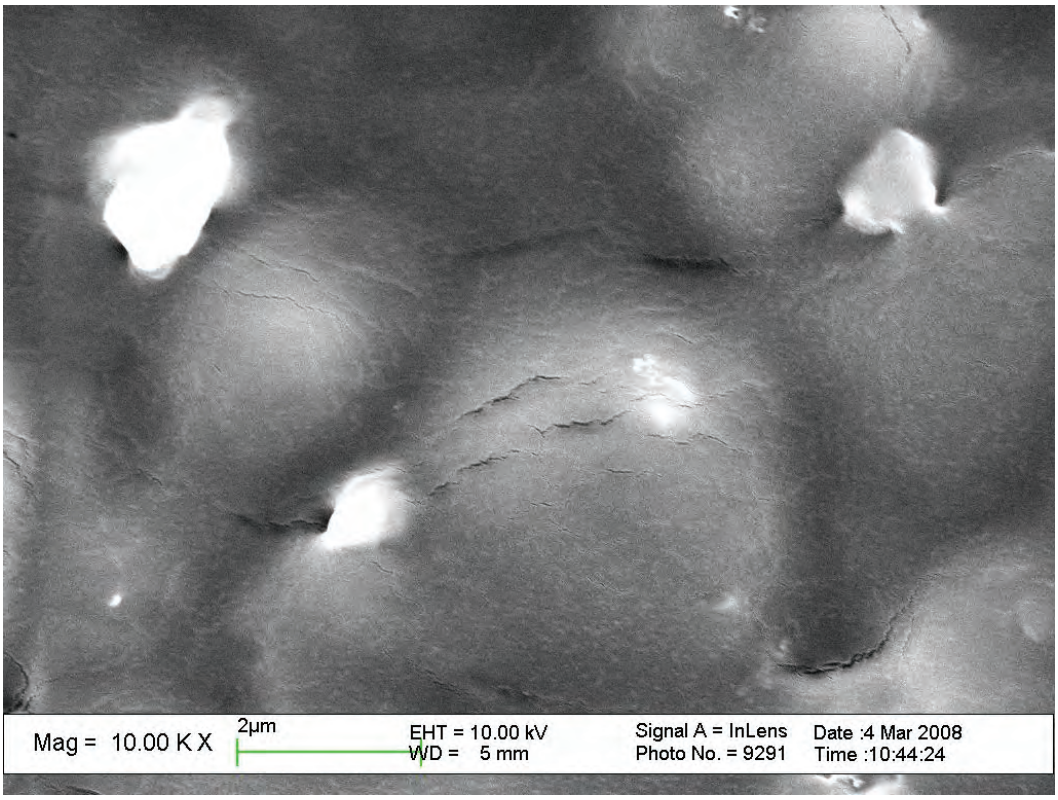

Figure 3. Scanning electron micrograph of the PCL based elastomer.

the electron beam bombardment for certain time after discussed with the SEM operator. It sounds reasonable.

It also should be highlighted that the phase morphology of polyurethane elastomers may be employed to analyze the differences of the mechanical properties of polyurethane elastomers. The differences in microstructure of three polyurethane elastomers could result in the different mechanical properties and abrasion resistances. The hard domains dispersed in that matrix act as the reinforcing carbon black in rubber, so that the polyurethane elastomer with higher microphase separation degree performed better mechanical properties and less abrasion loss than the sample with lower microphase separation degree.

3.3. Lnfluence of the Polyol Structure on the Thermal Stability of Polyurethane Elastomers

While a good combination of properties normally suggests toughness of the material, it does not ensure that parts made from such material will survive harsh conditions in the real application environment. As mentioned earlier, polyester based elastomers are generally considered much tougher than polyether based elastomers, however, because the ester linkage is susceptible to hydrolytic cleavage, polyester based elastomers break down rapidly in a hot environment. Therefore, besides general mechanical properties, one may need to carefully examine other factors, such as resistance to thermal degradation and abrasion, when selecting compounds for specific applications.

In **Table 3**, stress-strain and tear properties of the three polyurethane elastomers before and after aging in air at 120°C for168 hours are listed. It is evident from the data that PCL and PEA based elastomers retained their original stress-strain and tear properties after exposure to high temperature and oxidation, while the PTMG based elastomer lost 40% to 80% of its original properties under the same conditions. The results imply that PEA and PCL based elastomers are much more resistant to thermal degradation as compared to the PTMG based elastomer. However, there is no clear evidence that the PEA based elastomer are better than the PCL based elastomer in terms of resistance to thermal degradation, and vice versa.

3.4. Lnfluence of the Polyol Structure on the Abrasion Resistance of Polyurethane Elastomers

The abrasion resistance is highly important in applications such as rubber pads for tank track, conveyor belts, mining, pipeline pigs, squeegees, and industry wheels and tires [7,43,44]. **Table 4** shows Akron abrasion resistance of the three polyurethane elastomers. The data

Table 3. Tensile Strength and tear properties of elastomers aged at 120℃ for 168 hours.

Elastomers	Tensile Strength, Mpa		Elongation at break, %		Tear Strength, KN/m	
	Before	After	Before	After	Before	After
PEA-TDI	41.38	51.38	780	946	103.25	105.26
PCL-TDI	40.69	52.41	640	730	107.63	108.55
PTMG-TDI	37.24	7.07	570	200	98.16	56.88

Table 4. Abrasion resistance of polyurethane elastomers based on different backbones.

Elastomers	PEA-TDI	PCL-TDI	PTMG-TDI
abrasion loss, mg	17.9	16.8	66.8

indicated that elastomers based on PCL and PEA had similar abrasive resistance, and they are much better than that of the PTMG based elastomer.

3.5. Lnfluence of the Polyol Structure on the Dynamic Properties of Polyurethane Elastomers

One important application for polyurethane elastomers is tank track pads, road wheel & loading wheel flange, many sorts of tires, wheels, rollers and vibration- absorptive materials. In this application, polyurethane elastomers are constantly running at high-speed and under high-load. It is the intrinsic nature of virtually any material to build-up heat while running at high- speed and bearing high-load. Wheels, tires and rollers made from polyurethane elastomers generate heat when they are operating. The buildup of heat can cause failure of urethane parts by melting, tearing, or debonding. Depending on how much heat is generated and how fast the heat is dissipated to the environment, different polyurethane elastomers have different service lifetimes. To improve the service life of polyurethane elastomers in a dynamic environment, we need to improve the dissipation of the heat and select elastomers with improved dynamic properties that can generate less heat, thus run cool for extended time. While the former can be addressed by engineering design of wheels, tires and rollers, the latter has to be resolved from a formulation standpoint.

Dynamic properties of polyurethane elastomers can be analyzed using a Dynamic Mechanical Analyzer. The storage modulus and tanδ curves of the polyurethane elastomers based on different backbones are shown in **Figure 4 and 5**. A good compound for dynamic applications is generally represented by low tanδ values and constant modulus values over the working temperature range in which the parts will be utilized. As tanδ= E″/E′, where E″ is the loss modulus and E′ is the storage modulus, a lower tanδ value means that energy transferred to heat is much lower than energy stored. Therefore, lower heat buildup occurs in high-speed, high-load bearing applications. **Figure 5** shows tanδ value for the

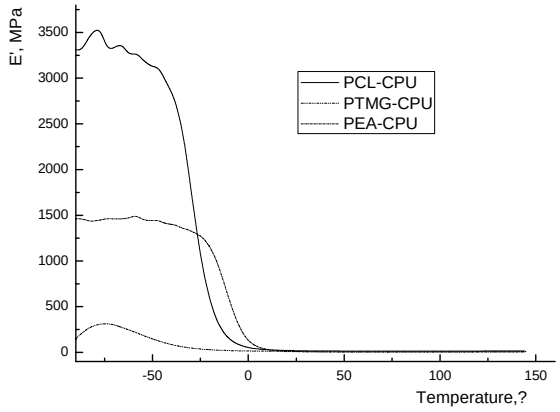

Figure 4. Storage modulus of the polyurethane elastomers based on different backbones.

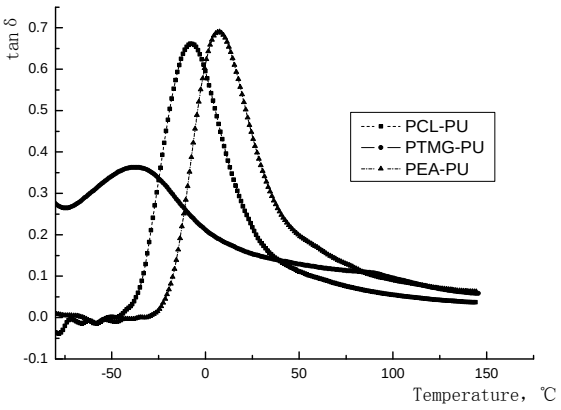

Figure 5. Tan δ curves of the polyurethane elastomers based on different backbones at temperature range from -80℃ to 160℃.

three polyurethane elastomers in a temperature range from –80 to 180℃. The tanδ curves show peaks at low temperature, which is attributed to the glass transition temperatures of the polyurethane elastomers. The tanδ peak of the PEA based elastomer locates in the higher temperature, this reason maybe the hindered cooperative motion of the polymer chains. The PCL based elastomer had higher tanδ value than the PTMG based elastomer at low temperature, but its tanδ value was the lowest one among the three polyurethane elastomers at higher temperature (**Figure 6**). This may stem from the microstructure of the PCL based elastomer. The dispersed phase formed by the hard phase and crystalline part of

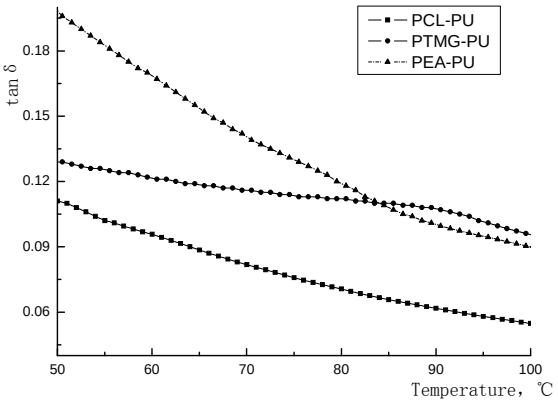

Figure 6. Tan δ curves of the polyurethane elastomers based on different backbones at operating temperature zone.

the soft phase reinforced the elastomer, and the strong interactions caused by lower degree of soft segment crystallinity and hydrogen bonds enable the motion of the polymer chains more synchronous with the load, which makes the heat build up lower at operating temperature. It is very important for dynamic application accompanied by heat build up that could possibly weaken materials, thus causing failure. Obviously, the PEA based elastomer might not be the best choice for dynamic applications if similar grades of PTMG and PCL based elastomers are readily available. As for PCL and PTMG based elastomers, though the PCL based elastomer has higher tanδ value at low temperature, some engineers believe that it is the tanδ value at higher temperature that really matters. The higher tanδ value at low temperature implies that a wheel made from the PCL based elastomer will build up heat faster than a wheel made from the PTMG based elastomer when the wheel is cold. However, as the temperature increases, tanδ value decreases. During use, the temperature of the wheel will stabilize at the temperature where heat generated is equal to the heat dissipated, and that will be the operating temperature of the wheel most of the time. This temperature for the PCL based elastomer wheel might be slightly higher than that of the PTMG based elastomer, depending on the engineering design of the wheels. On the other hand, the storage modulus of the PCL based elastomer is the highest one among the three elastomers, this is very helpful for high load application. However, considering the enhanced mechanical strength and resistance to thermal degradation of the PCL based elastomer over that of the PTMG based elastomer, the PCL based elastomer will perform better than the PTMG based elastomer in the field.

4. CONCLUSIONS

Three polyurethane elastomers based on different soft segments were prepared and their properties were compared side by side.

The PCL based elastomer exhibits the excellent tear and stress-strain properties that polyester based elastomers offer, while retaining superior compression set and resilience similar to polyether based elastomers.

The SEM results of all polyurethane samples showed the existing of the microphase separation structure. Particles of the dispersed phase formed by the hard phase and crystalline part of the soft phase grows bigger with the increasing crystallinity of the soft segments. The hard domains are irregular shapes and with the sizes of a few micrometers.

As polyester based polyurethane elastomers, PEA and PCL based elastomers are much more resistant to thermal degradation as compared to the PTMG based elastomer.

Polyurethane elastomers based on PCL and PEA had similar abrasive resistance, and they are much better than that of the PTMG based elastomer.

The tanδ value at operating temperature zone of the PCL based elastomer is lower than those of the PEA and PTMG based elastomers. And the PCL based elastomer had higher tanδ value than the PTMG based elastomer at the temperature around zero centidegree. Based on the time-temperature superposition principle, a conclusion can be made that the PCL based elastomer exhibits good wet skid resistance, low rolling resistance and outstanding dynamic application properties[45,46,47].

In a word, The PCL based elastomer possesses more balanced properties. It is a favorable choice for applications where a combination of engineering properties is desired.

5. ACKNOWLEDGEMENTS

This research is funded by the Polyurethane Department of GuangZhou SCUT Bestry Technology Joint-stock Co. Ltd. The authors are grateful to the teacher of National Engineering Research Center of Novel Equipment for Polymer Processing for their helpful advice.

REFERENCES

[1] S. R. Pajtas, (1990) Polyurethane non-pneumatic tire technology, Development and testing history, in SAE International Congress and Exposition. SAE, Warrendale, PA, USA: Detroit, MI, USA.

[2] L. Stokes and S. Pajtas, (1989) New non-pneumatic polyurethane tire based on innovative technology, Elastomerics, **121**, 19–23.

[3] T. M. Madkour and R. A. Azzam, (2002) Use of blowing catalysts for integral skin polyurethane applications in a controlled molecular architectural environment: Synthesis and impact on ultimate physical properties, Journal of Polymer Science Part A: Polymer Chemistry, **40**, 2526–2536.

[4] R. W. Fuest, (2002) Castable polyurethane elastomers-

Serving demanding engineering applications, Rubber World, **227(39).**

[5] C. Hooks, (2005) PU tyre runs cool, smooth, Urethanes Technology, **22(27)**.

[6] M. Furukawa, K. Ken, and S. Kugumiya, *et al*. (2008) Microphase separation of bulk and ultrathin films of polyurethane elastomers, Macromolecular Symposia, **267**, 9−15.

[7] I. R. Sare, J. I. Mardel, and A. J. Hill, (2001) Wear-resistant metallic and elastomeric materials in the mining and mineral processing industries: An overview, Wear, **250−251**, 1−10.

[8] Y. Jiang, Y. Shao, and Q. Zhang (1998) Preparation of tire chain of hot-plasticity type polyurethane elastomer, Fine Chemicals, **15**, 57−59.

[9] Z. Wirpsza, (1993) Polyurethanes: chemistry, technology, and applications, Ellis Horwood, London.

[10] V. L. Covolan, R. D. Ponzio and F. Chiellini, *et al*., (2004) Polyurethane based materials for the production of biomedical materials, Macromolecular Symposia, **218**, 273−282.

[11] S. Kutay, T. Tincer, and N. Hasirci, (1990) Polyurethanes as biomedical materials, British Polymer Journal, **23**, 267−272.

[12] S. M. Clift, (1991) Understanding the dynamic properties of polyurethane cast elastomers, Journal of Elastomers and Plastics, **23**, 66−84.

[13] A. Eceiza, M. D. Martin, and K. Caba, *et al*., (2008) Thermoplastic polyurethane elastomers based on polycarbonate diols with different soft segment molecular weight and chemical structure: Mechanical and thermal properties, Polymer Engineering and Science, **48**, 297−306.

[14] P. P. Barbara, P. Król, and S. Pikus, (2008) Supramolecular structure of crosslinked polyurethane elastomers based on well-defined prepolymers, Journal of Applied Polymer Science, **110**, 3292−3299.

[15] H. J. Kogelnik, H. H. Huang, and M. Barnes, *et al*., (1991) Comparison of the dynamic properties of solid polyurethane elastomers, Journal of Elastomers and Plastics, **23**, 314−344.

[16] G. Oertel, (1985) Polyurethane Handbook: Chemistry-Raw Materials-Processing-Application-Properties, 2ed *edition*, Hanser Publishers, New York.

[17] R. A. Assink, (1977) The study of domain structure in polyurethanes by nuclear magnetic resonance, Journal of Polymer Science: Polymer Physics Edition, **15**, 59−69.

[18] R. A. Assink and G. L. Wilkes, (1981) Study of domain structure in linear and crosslinked polyurethanes using pulsed proton NMR, Journal of Applied Polymer Science, **26**, 3689−3698.

[19] J. N. Gorce, J. W. Hellgeth, and T. C. Ward, (1993) Mechanical hysteresis of a polyether polyurethane thermoplastic elastomer, Polymer Engineering & Science, **33**, 1170−1176.

[20] D. J. Martin, G. F. Meijs, and G. M. Renwick, *et al*., (1996) Effect of soft-segment CH2/O ratio on morphology and properties of a series of polyurethane elastomers, Journal of Applied Polymer Science, **60**, 557−571.

[21] D. J. Martin, G. F. Meijs, and G. M. Renwick, *et al*., (1996) The effect of average soft segment length on morphology and properties of a series of polyurethane elastomers, I. Characterization of the series, Journal of Applied Polymer Science, **62**, 1377−1386.

[22] D. J. Martin, G. F. Meijs, and P. A. Gunatillake, *et al*., (1997) The effect of average soft segment length on morphology and properties of a series of polyurethane elastomers, II. SAXS-DSC annealing study, Journal of Applied Polymer Science, **64**, 803−817.

[23] H. D. Kim, J. H. Huh, and E. Y. Kim, (1998) Comparison of properties of thermoplastic polyurethane elastomers with two different soft segments, Journal of Applied Polymer Science, **69**, 1349−1355.

[24] K. S. Chen, T. L. Yu, and Y. H. Tseng, (1999) Effect of polyester zigzag structure on the phase segregation of polyester-based polyurethanes, Journal of polymer science, Part A, Polymer chemistry, **37**, 2095−2104.

[25] E. G. Bajsic, V. Rek, and A. Sendijarevic, *et al*., (2000) DSC study of morphological changes in segmented polyurethane elastomers. Journal of Elastomers and Plastics, **32**, 162−182.

[26] B. C. Chun, T. K. Cho, and Y. C. Chung, (2007) Blocking of soft segments with different chain lengths and its impact on the shape memory property of polyurethane copolymer, Journal of Applied Polymer Science, **103**, 1435−1441.

[27] P. Król, B. Pilch-Pitera, (2007) Phase structure and thermal stability of crosslinked polyurethane elastomers based on well-defined prepolymers, Journal of Applied Polymer Science, **104**, 1464−1474.

[28] K. Ken, S. Nakamura and, M. Furukawa, (2008) Effect of side groups of polymer glycol on microphase-separated structure and mechanical properties of polyurethane elastomers, Journal of Polymer Science Part B: Polymer Physics, **46**, 2054−2063.

[29] H. B. Zhang, Y. D. Chen, and Y. C. Zhang, *et al*., (2008) Synthesis and characterization of polyurethane elastomers, Journal of Elastomers and Plastics, **40**, 161−177.

[30] M. Furukawa, Y. Hamada, and K. Ken, (2003) Aggregation structure and mechanical properties of functionally graded polyurethane elastomers, Journal of Polymer Science Part B: Polymer Physics, **41**, 2355−2364.

[31] H. Goering, H. Krüger, and M. Bauer, (2000) Multimodal polymer networks: Design and characterisation of nanoheterogeneous PU elastomers, Macromolecular Materials and Engineering, **278**, 23−35.

[32] C. D. Eisenbach and W. Gronski, (1983) Hydrogen bonding and phase separation in segmented polyurethane elastomers as studied by 13C NMR magic angle spinning and FT-IR spectroscopy, Die Makromolekulare Chemie, Rapid Communications, **4**, 707−713.

[33] K. Madhavan and B. S. R. Reddy, (2006) Synthesis and characterization of poly (dimethylsiloxane-urethane) elastomers: Effect of hard segments of polyurethane on morphological and mechanical properties, Journal of Polymer Science Part A: Polymer Chemistry, **44**, 2980−2989.

[34] C. D. Eisenbach, T. Heinemann, and A. Ribbe, *et al*., (1992) Chain architecture and molecular self-organization of polyurethanes: Perspectives for thermoplastic

elastomers, Die Angewandte Makromolekulare Chemie, **202**, 221−241.

[35] H. S. Xia, M. Song, and Z. Y. Zhang, *et al*., (2007) Microphase separation, stress relaxation, and creep behavior of polyurethane nanocomposites, Journal of Applied Polymer Science, **103**, 2992−3002.

[36] H. C. Jung, S. J. Kang, and W. N. Kim, *et al*., (2000) Properties of crosslinked polyurethanes synthesized from 4, 4prime-diphenylmethane diisocyanate and polyester polyol, Journal of Applied Polymer Science, **78**, 624−630.

[37] L. Wu, X. Luo, and X. D. Wang, (2006) Influence of processing conditions on dual-phase continuous blend system of thermoplastic polyurethane with ethylene-propylene-diene monomer elastomer, Journal of Applied Polymer Science, **102**, 5472−5482.

[38] C. P. Christenson, M. A. Harthcock, and M. D. Meadows, *et al*., (1986) Model MDI/butanediol polyurethanes: Molecular structure, morphology, physical and mechanical properties, Journal of Polymer Science Part B: Polymer Physics, **24**, 1401−1439.

[39] R. R. Lagasse, (1977) Domain structure and time-dependent properties of a crosslinked urethane elastomer, Journal of Applied Polymer Science, **21**, 2489−2503.

[40] C. J. Ong and R. Saxon, (1976) Viscoelastic properties and heat generation in urethane elastomers. Journal of Applied Polymer Science, **20**, 1695−1710.

[41] T. O. Ahn, I. S. Choi, H. M. Jeong, *et al*., (1993) Thermal and mechanical properties of thermoplastic polyurethane elastomers from different polymerization methods, Polymer International, **31**, 329−333.

[42] S. Yamasaki, D. Nishiguchi, and K. Ken, *et al*., (2007) Effects of polymerization method on structure and properties of thermoplastic polyurethanes, Journal of Polymer Science Part B: Polymer Physics, **45**, 800−814.

[43] A. I. Hoodbhoy, (1976) Designing with plastics-cast solid-polyurethane industrial tires, Plastics Engineering, **32**, 37−38.

[44] I. S. Megna, (1986) Polyurethanes for roll covering, Rubber World, **194**, 20.

[45] R. Bond, G. F. Morton, and L. H. Krol, (1984) A tailor-made polymer for tyre applications, Polymer, **25**, 132−140.

[46] A. Lechtenboehmer, H. G. Moneypenny, and F. A. Mersch, (1990) Review of Polymer Interfaces in Tyre Technology, British Polymer Journal, **22**, 265−301.

[47] A. M. Shanmugharaj and A. K. Bhowmick, (2003) Dynamic mechanical properties of styrene-butadiene rubber vulcanizate filled with electron beam modified surface-treated dual-phase filler. Journal of Applied Polymer Science, **88**, 2992−3004.

J. Biomedical Science and Engineering, 2009, 2, 254-260 **JBiSE**
doi: 10.4236/jbise.2009.24039 Published Online August 2009 (http://www.SciRP.org/journal/jbise/).

Research on anti-seepage properties of geosynthetic clay lines in landfills

Xiao-Bo Xiong[1], Guo-Qing Gui[1], Shu-Zhi Ma[2]

[1]School of Engineering, Jinggangshan University, Ji'an, China; [2]School of Engineering, China University of Geosciences, Wuhan, China
Email: thongtao2006@163.com; JHBMSZ@163.com

Received 23 February 2009; revised 20 March 2009; accepted 26 March 2009.

ABSTRACT

In recent years, geosynthetic Clay liners (GCLs) are widely used in different kinds of anti-seepage projects and the anti-seepage availabilities of GCLs are regarded as increasingly important by engineers. Anti-seepage effectiveness of GCLs involves at least two aspects, such as Hydraulic conductivity of GCLs under engineering practice conditions, and Absorption ability of bentonite in GCLs in the course of liquid permeation. In this paper, Hydraulic conductivity tests are performed to obtain seepage coefficient of GCLs, taking liquids such as distilled, deioned water and landfill leachate, and solutions with single-species cation as the hydration and permeation liquid. The results Show that cation valence, cation concentration and hydration ionic radius in hydration and permeation liquids have influences on hydraulic conductivity of GCLs.

Keywords: Landfills; GCLs; Lines System; Lmpervious Barrier; Experimental Analysis

1. INTRODUCTION

Along with the rapid economic development and urbanization, the generation of municipal solid waste (MSW) increased drastically in China. Landfill is a primary method of ultimate disposition of municipal solid waste in many countries. The impervious barrier of cover system and lines system is the key to ensure that the landfills should not be the source of secondary pollution to the surrounding. Applications of geosynthetics, such as geotextile, geomembrance, GCLs, geonet (GN), geocomposite (GC) and geofoam (GF), etc., they are used to all aspects of landfill as liners and covers. With regard to GCLs as a new type material of seepage barrier, the authors present here some information on the composition of material, engineering characteristic, and make suggestion on the future development of this technology. It was investigated that the leakage prevention structures of 56 landfill sites for domestic wastes in China, and the results showed that leakage prevention structures were found designed improperly and leakages happened incidentally in landfills in China. Overseas experts have already acquired certain research on properties of GCLs, but research on this product is rare in our country. In this paper, we studied the properties of GCLs by means of testing, then points out that making use of GCLs is the trend of the applicable liner in future.

2. CURRENT STATUS AND PROSPECTS OF GCLs

The protection liners system of clay layer was widely used in USA before 1982. The new type of geosynthetics named GCLs come out in 1987 at a Germany company. In 1989, GCLs was widely applied in sanitary landfills in USA. And since 1995, the national code for the new type liner material was taken to draw up, which was finished in 1999 completely. Before 2000, only one document was found during the literature survey that discusses the performance of GCLs when installed as a single in-service liner (Lichtwardt and Comer, 1997).

Horace Moo-Young *et al*. (2004) reviews the state of the science and practice on the infiltration rate through compacted clay liner (CCL) for 149 sites and geosynthetic clay liner (GCL) for 1 site. The field hydraulic conductivities for natural clay liners range from 1×10^{-9}cm s^{-1} to 1×10^{-4}cm s^{-1}, with an average of 6.5×10^{-8}cm s^{-1}. There was limited information on GCL. For composite lined and geomembrane systems, the leak detection system flow rates were utilized. The average monthly flow rate for composite liners ranged from 0~32 l/hd for geomembrane and GCL systems. A GCL was installed on the bottom of a salinity-gradient solar pond in Texas in 1994. The pond has a surface area of approximately 1 acre (0.4 ha) and a water depth averaging 3.2 m. The GCL is a modified Gundseal, with a 30 mil (0.07cm) flexible polypropylene geomembrane backing with 0.5cm of bentonite clay bonded to one side. The performance of the GCL is presented as the variation in

hydraulic conductivity of the GCL over time for a 9-week period. The hydraulic conductivity remains fairly constant at 2×10^{-6} cm s^{-1}. This represents an increase over the initial conductivity, which was measured at 1×10^{-6} cm s^{-1}. In general, a GCL is most effective when placed under an effective overburden pressure where the minimum permeability can be obtained. This data set clearly indicates that additional research needs to be conducted to quantify the field infiltration rate of GCLs in landfills.

In China, Zhou Z. B. (2002) present the condition, mechanism and process of ion exchange between the ions of bentonite in the GCL and ions in leachate and their effects on GCL's impermeability, and some resolution methods. Yao Q. (2003) introduced design of impervious system of landfill and use of various impervious materials. Wang X. Q. (2004) analyzed the foreign application of geomembrane liner system and it is useful for landfill construction in China. Li Z. B. (2005) advanced a series of problems which needed to be deeply researched based on the research achievements by home and overseas scholars. Liu H. B. (2006) provided the background and basis for developing standard "Geosynthetic Clay Liner" and details product classification, test items and methods and performance index. LU H. Y. (2007) introduced the advantages of GCL serving as an anti-seepage system of hazardous waste landfill sites and demonstrates that the anti-seepage result of GCLs is better than CCLs. The study shows that all the indexes and benefits from this technique are much better than those from the traditional anti-seepage technique (**Table1**).

3. THE BASIC PROPERTIES OF GCLs

A GCL is a factory-manufactured, hydraulic barrier typically consisting of bentonite clay, supported by geotextiles and/or geomembranes held together by needling, stitching, or chemical adhesives. GCLs are typically used in areas where clay is not readily available or where conserving air space is an important factor. GCLs do not have the level of long-term field performance data that are available for GMs or CCLs because GCLs were developed recently (1986) and they are typically used with a GM in a composite liner system.

In recent years, GCLs is widely used in different kinds of anti-seepage projects, and the anti-seepage availabilities of GCLs are regarded as increasingly important by engineers. The four basic GCLs list as follows (see **Figure 1**), that is: two layer of GT/GM with bentonite and bonding agent(binder), two layer of GT/GM with bentonite and stitch fiber, two layer of GT/GM with bentonite and mending fiber, one layer of GT/GM(beneath the bentonite) with bentonite, etc.

Table 1. Statistics of anti-seepage engineering for man-made lake with GCLs in China.

Province	Numbers	Area/m^2	Province	Numbers	Area/m^2
Beijing	9	167398	Shanghai	37	95907
Zhejiang	28	138385	Jiangsu	22	77213
Tianjing	1	7000	Anhui	6	18395
Hubei	3	7280	Shanxi	1	6000
Guangdong	4	13240	Yunnan	3	18220
Guangxi	1	20000	Jiangxi	2	7254
Gansu	1	10000	Chongqing	1	15000
Neimenggu	1	25000	Hebei	1	50000

Anti-seepage effectiveness of GCLs involves at least three aspects: 1) Hydraulic conductivity of GCLs; 2) Absorption ability of bentonite in GCLs in the course of liquid permeation; 3) GCL internal shear strength while used in anti-seepage system.

The above aspects are so important that they could directly affect the factor of safety and effectiveness of anti-seepage project. Section of composite liner system landfill of MSW sanitary landfill (see **Figure 2**), Section of the cap of MSW sanitary landfill (see **Figure 3**).

In this paper, GCLs for indoors tests was made from the non-fabricated textile factory in Yixing city in jiangsu province, and two layer of GT/GM of bentonite (made by the CETCO Company, USA) with stitching in two geotextile fibers layer, it belongs to the type of Bentomat (see in **Figure 1**, the second graph). The total mass is 5.32kg/m^2 per unit area, with the lower GT is a kind of fabricated GT whose mass is 112g/m^2 per unit area, and with the upper GT is a kind of non-fabricated GT whose mass is 221g/m^2 per unit area.

Chemical components of Bentomat are: SiO_2 57.23%; Al_2O_3 18.45%; Fe_2O2.57%; FeO 1.19%; MgO 2.22%; CaO 1.53%; Na_2O 2.55%; K_2O 0.61%; H_2O^+4.30%; H_2O^- 7.9%; Cr_2O_3 0.0044%; ZnO 0.028%; NiO 0.0037%; Li_2O 0.003 8%; TiO_2 0.24%; P_2O_5 0.034%; Mn0.016%; Buring0.41%; Total 99.30%.

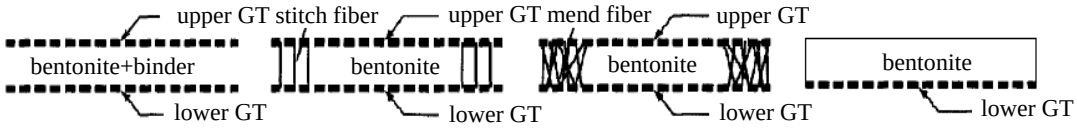

Figure 1. Sketch of four basic GCLs products.

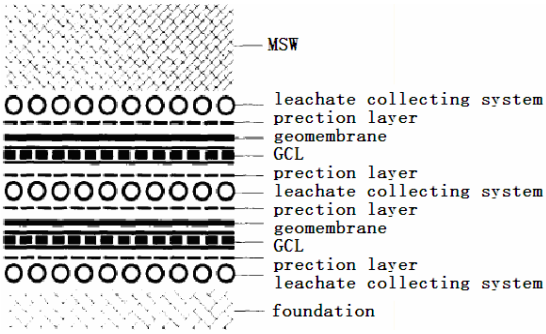

Figure 2. Section of composite liner.

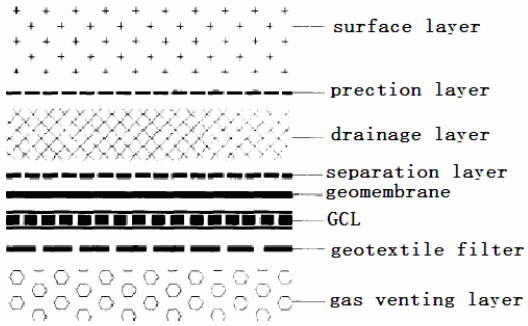

Figure 3. Section of the cap of landfill.

The swell stresses of a GCL, made by the CETCO Company, USA, were measured directly using a custom-made swell stress instrument under water-sorbed saturation conditions. The results show that in the test process, the variation of the swell stress curve with time can be divided into three segments. To characterize the mineralogical nature of the Nabentonite, six samples were studied by X-ray diffraction and results show a relatively homogeneous mineralogical composition. It consists of a complex mixture of different smectites, those of sodium nature clearly prevailing, with trace amounts of quartz, calcite and muscovite. This is determined by the fact that all the heated specimens collapse their main 001 spacing to 10 A ˚ and expand that same spacing to 16.5~16.8 A˚ upon treatment.

By comparison of the seepage coefficient curve of the two experimental conditions (see **Figure 4**), the seepage coefficient are approximate same when the vertical stress is less than 250kPa, otherwise, when the vertical stress is more than 250kPa, the seepage coefficient by

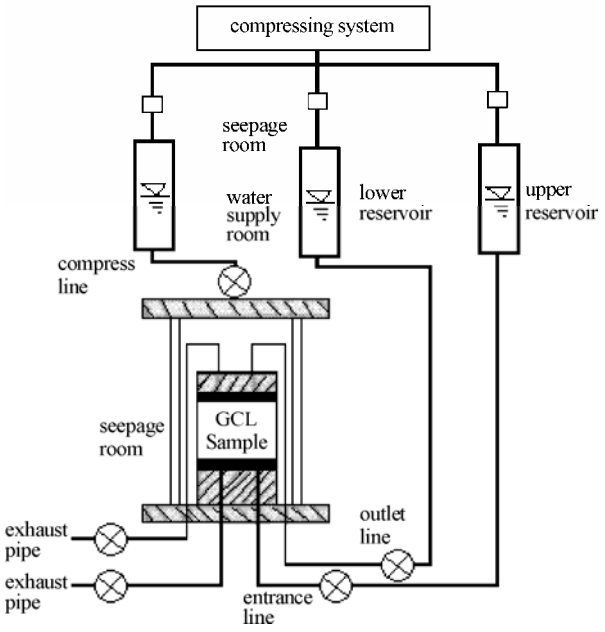

Figure 4. Seepage coefficient test apparatus.

Table 2. The results of hydrated swelling experiments of GCLs samples by main pressures. (Notes: MGCL is mass per unit area of GCLs.)

σ_w/kPa	M_{GCL}/kg/m^2	H_0/mm	H_σ/mm	H_w/mm	w/%	E_B
3	5.39	6.84	6.72	9.67	131.3	3.38
15	5.37	6.87	6.52	8.61	112.6	2.91
50	5.48	6.85	6.27	7.70	102.1	2.44
150	5.33	6.87	5.86	6.52	92.4	1.98
300	5.45	6.85	5.46	5.85	70.1	1.72
400	5.44	6.87	5.37	5.69	63.2	1.65

experiments under conditions of hydrate firstly and compress secondly (cw1) is lower than the seepage coefficient by experiments under conditions of compress firstly and hydrate secondly (wc2). That is, when the vertical stress is more than 250kPa, and the experiments under conditions of hydrate firstly and compress secondly, the thickness of GCLs is bigger, so that the seepage coefficient increase very slow.

The results of hydrated swelling experiments of GCLs samples by main stress list in **Table 2**, through the data of **Table 2**, firstly, the swelling deformation of GCLs increase very fast because of the properties of water absorption of bentonite, till the thickness of GCLs without change on the end. Under the series main stress such as 3kPa, 15kPa, 50kPa, 150kPa, 300kPa and 400kPa, the hydrated time list sequences as 12.8d, 9.8d, 8.3d, 6.0d, 5.0d and 5.0d (see **Figure 5**). When at a low main stress, the initial creep velocity is very high, and the total hydrated thickness is big, with increasing of σ_w, the thickness of GCLs decreasing, at the same time, the water content(w) and porosity ratio decreasing (show in **Table 2**).

From **Table 3**, we can find that the vertical pressure take much effect on the seepage properties, the seepage coefficient increases along with the increasing of the horizontal strain of GCLs, and when the horizontal strain is more than 6.0%, the velocity of the seepage coefficient increasing obviously. That is because, when the GCLs was taken horizontal tense, not only

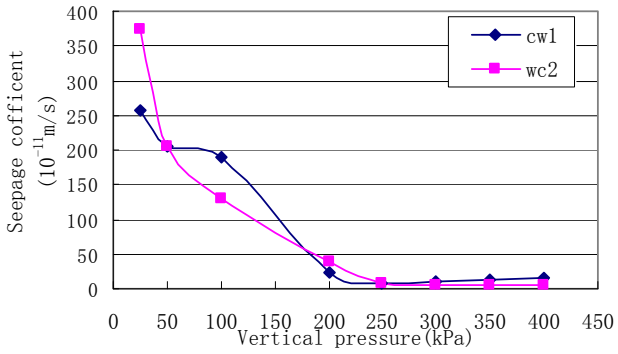

Figure 5. Seepage coefficient of GCLs under several conditions.

Table 3. Seepage coefficients by all grades Vertical pressure of GCLs under the condition of compress firstly and hydrated secondly or hydrate firstly and compress secondly.

Vertical pressure (kPa)	seepage coefficient (m/s)×10^{-10}		Vertical pressure (kPa)	seepage coefficient (m/s)×10^{-10}	
	Compress firstly	hydrate firstly		Compress firstly	Hydrate firstly
25	25.6	37.3	250	0.738	0.840
50	20.6	20.6	300	0.916	0.407
100	18.9	13.1	350	1.40	0.463
200	2.32	3.78	400	1.43	0.581

the upper and the low GT cause horizontal extension, and the bentonite stitched in the middle could be scattered by horizontal tension, at the same time, the porosity of the bentonite increases after water hydrated, then the seepage coefficient increases. When the horizontal strain is big (usually more than 6.0%), even when the horizontal strain attain to 16.0%, the bentonite grains decreasing, the thickness of some parts of the GCLs is very low, the seepage properties is very high, and the anti-seepage properties of GCLs vanish wholly. From the above statement, in practical anti-seepage engineering projects, the non-uniform settlement of should be calculated before construction, and the horizontal strain of GCLs is extremely controlled to 6.0%, thus, the anti-seepage properties of GCLs could be run ordinary.

In a newly built landfill facility, the lower most leachate barrier is composed of GCL strips; adjoining strips are not seamed and, instead, they partially overlap and are ‘‘sealed’’ by a layer of sodium bentonite powder. The performance of this Na-bentonite is the main object of investigation of the present study. In laboratory reconstructions, the mechanical and geotechnical behavior of the Na-bentonite placed in between adjoining GCL strips was evaluated, as it is in this situation that the Na-bentonite is less constrained physically and thus more prone to deformation and rupture. X-ray diffractometry was used to identify the minerals making up the clay powder; several laboratory tests were performed to geotechnically characterize the clay; and cakes with different water contents of sodium bentonite were submitted to pure shear deformation using an automated pure shear rig to evaluate its behavior when subject to load, and wetting and drying cycles. The results prompted the search for field evidence of clay rupture around the landfill facility by means of geophysical and geochemical investigations, together with a detailed structural study of the fracture network of the granite. The swelling behavior of the Na bentonite is highly dependent on the type of encapsulation between the cover and the carrier geotextiles and on the chemical composition of the fluids involved.

From the above, a reliable, easily handled and cheap waterproof roll liner material was designed, in which the Bentonite, a kind of clay soil with unusual self-sealing ability, was used as the protective barrier for containment of hazardous waste in landfills. On the basis of the materials’ choice, the permeability properties of this new-style synthetic liner under various conditions were tested. The permeability coefficient of Na^+-Bentonite was less than that of Ca^{2+}-Bentonite. The suitable adhesives can enhance the waterproof of Na^+-Bentonite. After Na^+-Bentonite and the new liner were pretreated by water and well maintained, they hardly changed their permeability when they met such leachates as inorganic acids/bases and organic solvent . The new liner presents good “welding” property even if it was damaged. The experimental results indicate that this kind of bentonite waterproof roll liner is very suitable for landfill.

When MSWL was taken as the hydrated liquid and seepage liquid, to analyze the chemical component of the liquid seeping from GCLs, and attain all kinds of single-species cation iron and Chemical Content of BOD_5, COD and NH_4-N of Leachate from landfills, from the data of **Table 4**, we can find that GCLs took effective absorption with all kinds of single-species cation iron and Chemical Content of BOD_5, COD and NH_4-N. The results show that GCLs has large absorption ability on the permeation liquids. But the ability is decreasing with increase of permeation volume, and the types of hydration liquids exercise great influence on the variation of GCLs absorption, and the content some single-species cation iron of the permeation liquids has no change, it shows that the absorption of GCls to cation iron is very low.

Table 4. Chemical Content of BOD_5, COD and NH_4-N of Leachate from landfills.

Flow of Porosity Volume	BOD_5/mg/l	COD/mg/l	NH_4-N/mg/l
0.50	800	6200	1059
1.25	900	6800	1538
2.09	1600	15800	1585
Original liquid	2500	16000	3426

A series of confined swell tests were conducted on a needle-punched GCLs with tap water as the hydration medium. The effects of the static confining stress on the swelling characteristics of GCLs and the hydration time under different confining stresses were explored. Increasing the static confining stress led to: shorter hydration time; smaller final GCL height; less final GCL bulk void ratio; smaller final bentonite moisture content.

4. DESIGN CALCULATOR-LEAKAGE RATE THROUGH GCLs

4.1. Problem Statement

This calculator computes the rate of leakage through defects in a composite liner, i.e. GCLs (see **Figure 6**). The thickness of a hydrated GCLs depends on the compressive stress applied during hydration. Typical values are between 5 and 10 mm. Field evaluation, sponsered by USEPA, of leakage rate for double-lined landfills indicates that GM/GCL composite liners outperform GM/ CCL liners (Othman *et al*., 1998.)

The rate of leakage through a GCL due to GCL permeability is negligible compared to the rate of leakage through defects in the GCL Hence, only leakage through defects will be considered. If there is a defect in the GCL, the liquid first passes through the defect, then it flows laterally some distance between the GCL and the low-permeability soil, and, finally it infiltrates in the low permeability soil.

Flow between GCL and low-permeability soil is called interface flow, and is highly dependent upon the quality of contact between the two components Contact conditions are defined as follows:

1) Good contact conditions correspond to a GCL installed, with as few wrinkles as possible, on top of a low-permeability soil layer that has been adequately compacted and has a smooth surface. Contact quality factor (C_{qo}) (circular, square, rectangular) is 0.21, Contact quality factor ($C_{q\infty}$) (infinite length) is 0.52.

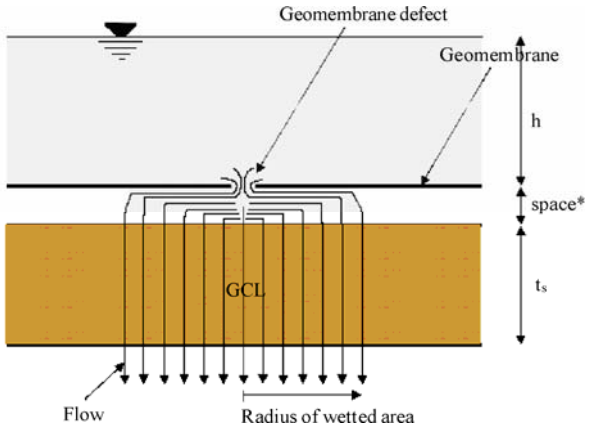

* Space exaggerated to show interface flow

Figure 6. Schematic diagram of GM/GCL calculation section.

Table 5. Representative installation defect densities.

Installation quality	Defect density (number per acre)	Frequency (percent)
Excellent	Up to 1	10
Good	1 to 4	40
Fair	4 to 10	40
Poor	10 to 20*	10

2) Poor contact conditions correspond to a GCL that has been installed with a certain number of wrinkles, and/or placed on a low-permeability soil that has not been well compacted and does not appear smooth. Contact quality factor (C_{qo}) (circular, square, rectangular) is 1.15, Contact quality factor ($C_{q\infty}$) (infinite length) is 1.22.

*Higher defect densities have been reported for older landfills with poor installation operations and materials; however, these high densities are not characteristic of modern practice.

The Help model provides guidance for estimating the defect densities. Some useful information on the Help model is given in the **Technical Note on Using HELP Model (ver 3.07)**. There are mainly two types of defects, manufacturing defects and installation defects. Typical geomembranes may have about 0.5 to 1 (1 to 2 per hectare) pinholes per acre from manufacturing defects (Pinholes are defects with a diameter equal or smaller than the geomembrane thickness. The density of installation defects is a function of the quality of installation, testing, materials, surface preparation, equipment, and QA/QC program. Representative installation defect densities as a function of the quality of installation are given in **Table 5** for landfills being built today with the state of the art in materials, equipment and QA/QC.

Studies by Giroud and Bonaparte have shown that for geomembrane liners installed, with strict construction quality assurance, could have one to two defects per acre (4000m^2) with a typical defect diameter of 2mm (i.e., a defect area of 3.14×10^{-6} m^2). Typical for liner performance evaluation one defect per acre (4000m^2) is considered with a defect area of 0.1 cm^2 (equivalent to defect diameter of 3.5 mm), for a conservative design a defect area of 1 cm^2 (equivalent defect diameter of 11 mm) can be considered.

4.2. Problem Solution

Different geomembrane defect shapes will be considered: Circular defect with diameter of d

$$\frac{Q}{A} = n \cdot 0.976 \cdot C_{qo} \cdot [1 + 0.1 \cdot (h/t_s)^{0.95}] \cdot d^{0.2} \cdot h^{0.9} \cdot k_S^{0.74}$$

Rectangular defect with width of b and length of B:

$$\frac{Q}{A} = n \cdot C_{qo} \cdot [1 + 0.1 \cdot (h/t_s)^{0.95}] \cdot b^{0.2} \cdot h^{0.9} \cdot k_S^{0.74}$$
$$+ n \cdot C_{q\infty} \cdot [1 + 0.2 \cdot (h/t_s)^{0.95}] \cdot (B-b)^{0.1} \cdot h^{0.45} \cdot k_S^{0.87}$$

Q-Leakage rate through the considered geomembrane defect (m^3/s);

Q*-Leakage rate per unit length of geomembrane defect ($m^3/s.m$);

A-Considered geomembrane area (m^2);

N-Number of defects per considered geomembrane area (A);

Co or $C_{q\infty}$-Contact quality factor (see **Table 6**);

H-Hydraulic head on top of the geomembrane (m);

t_s-Thickness of the low-permeability soil component of the composite liner (m);

D-Diameter of circular defect (m);

b-Width of defect (m);

B-Length of rectangular defect (m).

Limitation of the equations presented:

1) If the effect is circular, the defect diameter should be no less than 0.5 mm and not greater than 25 mm. In the case of the defects that are not circular, it is proposed to use these limitations for the defect width.

2) The liquid head on top of the geomembrane should be equal to or less than 3 m.

4.3. Input Values

Case 1: Geometry of circular defect

① Considered geomembrane area(A) is 4000m^2; ② Hydraulic head on top of the geomembrane(m) is 0.3m; ③ Thickness of the low-permeability soil(m) is 2m; ④ Permeability of the low-permeability soil(m/s) is 1.0×10^{-7}m/s.

Properties of circular defect

① Contact (good or poor) Good; ② Number of defects (n) is 1; ③ Diameter of defect (d) is 0.0002m.

Case 2: Geometry of Rectangular Defect

Properties of Rectangular Defect

Width of defect (b) is 0.002m; Length of defect (B) is 0.01m, the else conditions like **Case 1**.

5. CONCLUSIONS

In this paper, a series of research work including about the laboratory tests of GCLs is conducted and several valuable conclusions are obtained:

Table 6. Comparison between theoretical

Case number	Theoretical structure	Practical anti- seepage structure	Maximum flow, $m^3/(m^2.d)$
Case1	One layer GM, beneath high seepage layer	GM+ foundation with high permeability index or geocomposite (such as geotextile)	3.14×10^{-3}
Case2	One layer GM, beneath low seepage substituted layer	GM+geocomposite with low permeability index (such as GCL)	7.97×10^{-8}

1) A geosynthetic hydraulic conductivity device is designed to measure seepage coefficients of GCLs under constant normal stress conditions. Seepage coefficients of GCLs is measured for different hydrated and permeated liquids using the apparatus. Free swelling tests and hydration swelling tests of GCLs and bentonnite performed in order to research the swelling characteristics of GCLs and its influencing factors, including normal stress, loading-hydration sequence and hydration liquid. The results show that these factors have influences on GCLs swelling characteristics. Similar influencing laws can be obtained in the two tests.

2) Seepage coefficients tests are performed to obtain hydraulic conductivity of GCLs, taking liquids such as distilled, deioned water and landfill leachate, and solutions with single-species cation as the hydration and permeation liquid, the results show that cation valence, cation concentration and hydration ionic radius in hydration and permeation liquids have influences on hydraulic conductivity of GCLs. The influences of stress conditions and loading-hydration sequence on GCLs hydraulic conductivity are researched, the results Show that normal stress and horizontal strain, as well as loading-hydration sequence, all have influences on the variety of hydraulic conductivity.

3) Absorption ability of GCLs in the course of liquid permeation is studied, and its influencing factors are also discussed, including hydration liquid and permeation time. The results show that GCLs has large absorption ability on the permeation liquids. But the ability is decreasing with increase of permeation volume, and the types of hydration liquids exercise great influence on the variation of GCLs absorption.

4) Analysis are made to combine the conclusion obtained in this study with practical engineering projects, and proposals of building method of GCLs are advanced.

6. ACKNOWLEDGEMENTS

Some research results described in this paper were developed by the author in his graduate study between 1997 and 2000 in Nanjing University. The author gratefully acknowledges his teacher (Academician of Chinese Academy of Sciences Prof. Jun SUN) for his helpful direction and suggestion to the author during his studying in Tongji University. The authors would like to express their thanks to many teachers and staffs at the university of tongji university, nanjing university, and china university of geosciences, and jinggangshan university for the help in presenting some related experimental data.

REFERENCES

[1] J. Sun, *et al.*, (2005) Municipal environmental geotechnical engineering [M]. Shanghai: Shanghai Scientific and

Technical Publishers. (In Chinese).

[2] X. B. Xiong, (2000) Environmental geotechnical research on municipal sanitary landfill, Nanjing: Nanjing University.

[3] B. Shi, *et al*., (2003) Environmental geotechnical problems and their treatment of municipal sanitary landfills in the southeast of China, Journal of Disaster prevention and Mitigation Engineering, **23(4)**, 91−97.

[4] H. Y. Fang, (2000) Environmental geotechnology perspective in the 21st century, Chinese Journal of Geotechnical Engineering, **22(1)**, 1−11.

[5] Z. B. Li, (2007) Research on anti-seepage availability of geosynthetic clay liners and related mechanism analysis, Shanghai: Tongji University.

[6] J. He, C. H. Xia, and J. S. Hu, (2007) Equivalence analysis of GCL and CCL composite liner, Hydrogeology & Engineering Geology, **3**, 102−106.

[7] X. B. Xiong, B. Shi, *et al*., (2000) The recent development of geotechnical research on municipal waste sanitary landfill in foreign countries, Journal of Engineering Geology, **3**, 345−350.

[8] X. B. Xiong, B. Shi, *et al*. (2000) Current status and prospects of geotechnical research on the municipal solid Waste (MSW) disposal in China", Hydrogeology and Engineering geology, **3**, 25−29.

[9] X. B. Xiong, B. Shi, and W. He, (2000) The current development of geotechnical research on municipal sanitary landfill in China, Proceedings of the International Symposium on High Altitude & Sensitive Ecological Environmental Geotechnology, "Environmental Geotechnology," Nanjing University Press, 76−85.

[10] X. B. Xiong, G. Q. Gui, B. Shi, *et al*., (2008) Evaluation and discussion of liner system in sanitary landfills, Proceedings of the 9th International Symposium on Environmental Geotechnology and Global Sustainable Development, Hong Kong University.

[11] M. Y. Horace, *et al*., (2004) Characterization of infiltration rates from landfills supporting groundwater modeling efforts, Environmental Monitoring and Assessment, Springer Netherlands, ISSN 0167-6369 (Print) 1573−2959 (Online), **96(1−3)**, 283−311.

[12] A. Bouazza, (2002) Review article: Geosynthetic clay liners, Geotextiles and Geomembranes, **20**, 3−17.

[13] G. R. J. Browning, (1998) Geosynthetic clay liners: A review and evaluation, Trans. Inst. Min. Metall., Sect. B, **107**, 120−129.

[14] R. M. Koerner, (1994) Geosynthetic clay liners, Chapter 6, Designing with Geosynthetics, 3rd Edition, Prentice-Hall, Englewood Cliffs, N. J., 624−657.

[15] G. Heerten, (2002) Geosynthetic clay liner performance in geotechnical applications, In: Koerner and Gartung (Eds.), Clay geosynthetic barriers, 3−19.

[16] J. M. Southen and R. K. Rowe, (2005) Modeling of thermally induced desiccation of geosynthetic clay liners, Geotextiles and Geomembranes, **23**, 425−442.

J. Biomedical Science and Engineering, 2009, 2, 261-272 **JBiSE**
doi: 10.4236/jbise.2009.24040 Published Online August 2009 (http://www.SciRP.org/journal/jbise/).

Finger-vein image recognition combining modified hausdorff distance with minutiae feature matching

Cheng-Bo Yu, Hua-Feng Qin, Lian Zhang, Yan-Zhe Cui

Chongqing Institute of Technology, Chongqing 400050, China
Email: yuchengbo@cqit.edu.cn

Received 6 January 2009; revised 22 February 2009; accepted 26 February 2009.

ABSTRACT

In this paper, we propose a novel method for finger-vein recognition. We extract the features of the vein patterns for recognition. Then, the minutiae features included bifurcation points and ending points are extracted from these vein patterns. These feature points are used as a geometric representation of the vein patterns shape. Finally, the modified Hausdorff distance algorithm is provided to evaluate the identification ability among all possible relative positions of the vein patterns shape. This algorithm has been widely used for comparing point sets or edge maps since it does not require point correspondence. Experimental results show these minutiae feature points can be used to perform personal verification tasks as a geometric representation of the vein patterns shape. Furthermore, in this developed method. we can achieve robust image matching under different lighting conditions.

Keywords: Biometrics; Finger-Vein Verification; Gabor Enhancement; Minutiae Matching; Modified Hausdorff Distance

1. INTRODUCTION

Biometrics is the science of identifying a person using their physiological or behavioral features. Recently, vein pattern biometrics has attracted increasing interest from many research communities. Finger-vein recognition is a new biometrica identification technology using the fact that different person has a different finger-vein pattern [2,3,4,5]. Compared with fingerprint recognition, the advantages of the finger-vein recognition are [1]: 1) Do not need to consider the condition of the skin surface and can prevent the artificial finger; 2) Increase the forgery difficulty by using the invisible features inside the human body which only appears under the infrared light; 3) Non-contact recognition has no bad effect on public health. The properties of uniqueness, stability and strong immunity to forgery of the vein pattern make it become a potentially good biometric which offers secure and reliable for person identification. A typical vein pattern biometric system consists of five processing stages [5]: image acquisition, image enhancement, vein pattern segmentation, feature extraction and matching. During the image acquisition stage, vein patterns are usually obtained using infrared imaging technologies. One method is using a far-infrared camera to acquire the vein pattern images of finger-vein [1,2,6]. In order to get the shape representation of the pattern, after obtaining the images, vein pattern is separated and extracted from the background. Finally, a robust image similarity measurement is imperative for matching images under different conditions. There are a number of previous methods based on Hausdorff distance function for image matching [7,8,9,10,11]. One of the most distinguished benefits of Hausdorff distance is that it does not require point correspondences between two objects or two images. Dubuisson and Jain [12] developed several modified Hausdorff distances (MHD) for comparing the edge maps computed from the gray-scale images. Paumard proposed a censored Hausdorff distance (CHD) for comparing binary images [13]. Takacs introduced the neighborhood function and associated penalties to extend the MHD for face recognition [14,24,25]. Guo *et al*. proposed a new modified Hausdorff distance which is weighted by a function derived from the spatial information of human face [15]. Furthermore, Lin *et al*. proposed modified Hausdorff distances with spatial weighting determined by eigenface features [16]. The eigenface-based weighting function provides more weighting on important facial features, such as eyes, mouth, and face contour. Zhu *et al*. employed an improved Gabor filter for computing edge maps and applied a weighted modified Hausdorff distance (WMHD) in a circular Gabor feature space for comparing images [17]. LingyuWanga applied the modified Hausdorff distance based matching scheme to the interesting points for comparing images [6].

This research is motivated by P. L. Hawkes *et al* [6].

In this paper, we utilize the modified Hausdorff distance (MHD) to analyze the spatial similarity between the minutiae feature sets. Experimental results indicate that these minutiae feature points can be used to perform personal verification tasks as a geometric representation of the vein patterns shape. Furthermore we are able to achieve robust image matching under different lighting conditions.

2. PREPROCESSING OF INFRARED VEIN PATTERN IMAGES

2.1. Finger-Vein Pattern Database

Our finger-vein image capture device mainly consists of near-infrared light source, lens, cavum, light filter, image ingesting equipment. Vein patterns cannot be observed using normal, visible rays of light since they are beneath the skin's surface. However, vein patterns can be viewed through an image sensor which is sensitive to near-infrared light (wavelengths between 700 and 1000 nanometers), because near-infrared light passes through human body tissues and are blocked by pigments such as hemoglobin or melanin. As hemoglobin exists densely in blood vessels, near-infrared light shining through causes the veins to appear as dark shadow lines in the near-infrared image. To obtain a stable finger-vein pattern ,our light source adopts near-infrared light source with wavelength of 890 μm, the image ingesting part adopts near-infrared CCD camera with wavelength of 900 μm. our finger-vein database comprises of 50 distinct subjects, each subject having ten different images, taken at different times and obtained from middle finger in the right hand. The images are subject to variations such as lighting. All the images are taken at a dark homogeneous background and the finger is in upright, frontal position (with a tolerance for some side movement). The images are 256 grey levels per pixel and normalized to 328×376 pixels. In our analysis, no pre-processing of the images was conducted. Example image of five subjects are shown in **Figure 1(a)**.

2.2. The Lmage Normalization

The proportion of the vein area varies mostly at different time. And for the convenience in further study, the dimension size normalization is done in this paper. The vein image is defined as 64×96. That is to say the image zooming will be done. For the difference of acquisition time, light intensity and the personal palm thickness, the image gray scale distribution is different highly. If the image difference is great, the difficulty of image processing and matching will be increased. So the image must be normalized. All of the images must be converted to the standard image of the same mean and variance.

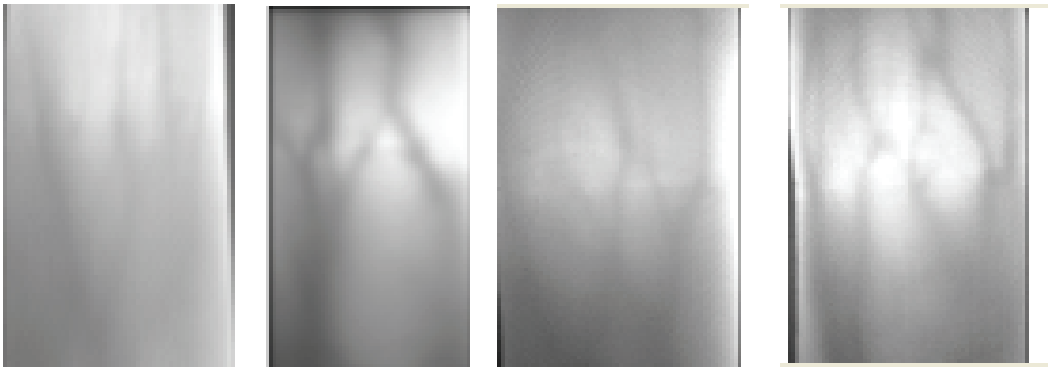

(a) Input image

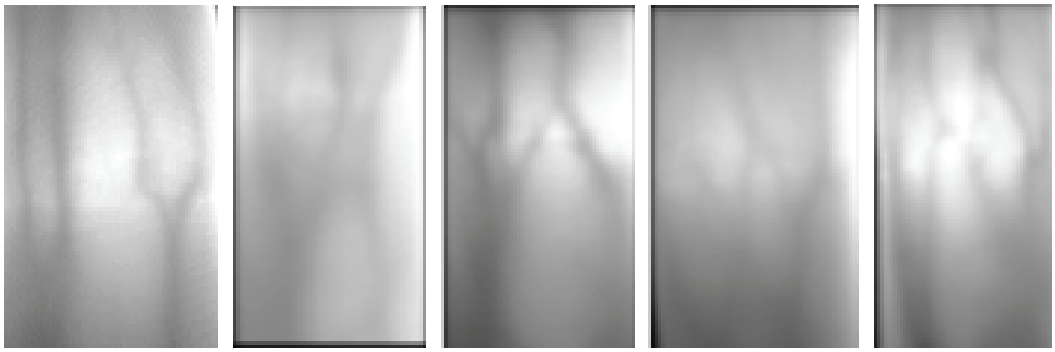

(b) Normalized image

Figure 1. The vein image.

For dispelling the illumination effect, a method of gray scale normalization is adopted.

$$p(i,j)=\frac{p'(i,j)-G_1}{G_2-G_1}\times 255 \quad (1)$$

where $p'(i,j)$ is the gray scale value of original image; $p(i,j)$ is the gray scale value after converted; G_1 is the minimum gray scale of original image; G_2 is the maximum gray scale of original image. **Figure 1(b)** shows the vein pattern image after enhancement with noise reduction and normalization.

2.3. Orientation Image

The orientation image represents an intrinsic property of the finger-vein images and defines invariant coordinates for ridges and valleys in a local neighborhood. A number of methods have been proposed to estimate the orientation field of fingerprint images [1,10,11,17]. Similarly, by viewing a finger-vein image as an oriented texture, we have improved orientation estimation algorithm. Given a normalized image f, the main steps of the algorithm are as follows:

1) Compute the gradients $\partial_x(i,j)$ and $\partial_y(i,j)$ at each pixel (i,j). Depending on the computational requirement, the gradient operator may vary from the simple Sobel operator to the more complex Marr-Hildreth operator.

2) Estimate the local orientation of each pixel (i,j).

a) Use the window $W\times W$ to slide in the original image, pixel gray value in the center of the window is $f(i,j)$.

b) Orientation of window $W\times W$ is estimated and is regarded as orientation of the pixel (i,j) in the center of the neighborhood (the size of the neighborhood is decided by the actual conditions). The equations using to estimate the local orientation is as follows:

$$V_x(i,j)=\sum_{u=i-\frac{W}{2}}^{i+\frac{W}{2}}\sum_{v=j-\frac{W}{2}}^{j+\frac{W}{2}}\left(2\partial_x(u,v)\partial_y(u,v)\right) \quad (2)$$

$$V_y(i,j)=\sum_{u=i-\frac{W}{2}}^{i+\frac{W}{2}}\sum_{v=j-\frac{W}{2}}^{j+\frac{W}{2}}\left(\partial_x^2(u,v)-\partial_y^2(u,v)\right) \quad (3)$$

$$\theta(i,j)=\frac{1}{2}\arctan\left(\frac{V_x(i,j)}{V_y(i,j)}\right) \quad (4)$$

where $\theta(i,j)$ is the least square estimate of the local ridge orientation at the block centered at pixel (i,j). Mathematically, it represents the direction which is orthogonal to the dominant direction of the Fourier spectrum of the $W\times W$ window.

c) If every point in the image is passed, namely orientation of all pixels are estimated, that is end. Otherwise, repeating above Step.

3) Due to the presence of noise, corrupted ridge and valley structures, minutiae, etc. in the input image, the estimated local ridge orientation, $\theta(i,j)$, may not always be correct. Since local ridge orientation varies slowly in a local neighborhood where no singular points appear, a low-pass filter can be used to modify the incorrect local ridge orientation. In order to perform the low-pass filtering, the orientation image needs to be converted into a continuous vector field, which is defined as follows:

$$\phi_x(i,j)=\cos(2\theta(i,j)) \quad (5)$$

and

$$\phi_y(i,j)=\cos(2\theta(i,j)) \quad (6)$$

where $\phi_x(i,j)$ and $\phi_y(i,j)$ are the x and y components of the vector field respectively. In the resulting vector field, the low-pass filtering can be performed as follows:

$$\phi_x'(i,j)=\sum_{u=i-\frac{W_\phi}{2}}^{i+\frac{W_\phi}{2}}\sum_{v=j-\frac{W_\phi}{2}}^{j+\frac{W_\phi}{2}}\left(h(u,v)\phi_x(i-u,j-v)\right) \quad (7)$$

and

$$\phi_y'(i,j)=\sum_{u=i-\frac{W_\phi}{2}}^{i+\frac{W_\phi}{2}}\sum_{v=j-\frac{W_\phi}{2}}^{j+\frac{W_\phi}{2}}\left(h(u,v)\phi_y(i-u,j-v)\right) \quad (8)$$

where h is a two-dimensional low-pass filter with unit integral and $W_\phi\times W_\phi$ specifies the size of the filter.

4) Compute the local ridge orientation at (i,j) using

$$O(i,j)=\frac{1}{2}\arctan\left(\frac{\phi_x'(i,j)}{\phi_y'(i,j)}\right) \quad (9)$$

With this algorithm, a fairly smooth orientation field estimate can be obtained. **Figure 2** shows the first example of the orientation image estimated with our algorithm in **Figure 1**.

2.4. Gabor Filter

The configurations of parallel ridges and valleys with well defined frequency and orientation in a Finger Vein image provide useful information which helps in removing undesired noise. The sinusoidal-shaped waves of

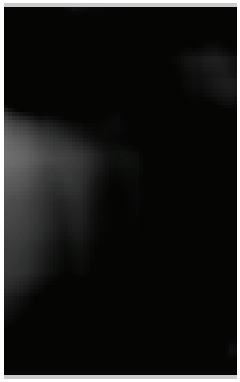

Figure 2. Orientation fields using and our method ($W = 20$ and $W_\phi = 10$).

ridges and valleys vary slowly in a local constant orientation. Therefore, a band pass filter is used to tune the corresponding frequency. Moreover, orientation can efficiently remove the undesired noise and preserve the true ridge and valley structures. Gabor filters have both frequency-selective and orientation-selective properties and have optimal joint resolution in both spatial and frequency domains. Therefore, it is appropriate to use Gabor filters as band pass filters to remove the noise and preserve true ridge/valley structures.

The circular Gabor filter is an effective tool for texture analysis [20], and has the following general form:

$$G(x,y,\theta,u,\sigma) = \frac{1}{2x\sigma^2}\exp\left\{-\frac{x^2+y^2}{2\sigma^2}\right\} \exp\{2\pi i(ux\cos\theta + uy\sin\theta)\} \quad (10)$$

where $i = \sqrt{-1}$, u is the frequency of the sinusoidal wave, θ controls the orientation of the function, and σ is the standard deviation of the Gaussian envelope. To make it more robust against brightness, a discrete Gabor filter, $G(x,y,\theta,u,\sigma)$, is turned to zero DC (direct current) with the application of the following formula:

$$\tilde{G}(s,y,\theta,u,\sigma) = G(x,y,\theta,u,\sigma) - \frac{\sum_{i=-n}^{n}\sum_{j=-n}^{n} G(x,y,\theta,u,\sigma)}{(2n+1)^2} \quad (11)$$

Here $(2n+1)^2$ is the size of the filter. In fact, the imaginary part of the Gabor filter automatically has zero DC because of odd symmetry. The adjusted Gabor filter is used to filter the preprocessed images. In our system, we applied a tuning process to optimize the selection of these three parameters $\theta = O$, $u = 1.5179$, $\sigma = 0.1116$.

2.5. The Vein Extraction

The image segmentation is very important in the whole process of finger vein recognition and it is very difficult. There are several image segmentation methods. The classic methods are threshold method [26], region growing method [27], relaxation method [28], edge detection method [29], split-merge algorithm [31] and so on. The modern methods are NN method [30], fuzzy clustering method [32] and so on. The different methods are adapted in the different application fields. There is no segmentation method fitting all images. So selecting the suitable segmentation method is very important. Therefore, we proposed a completely new method to segregate the vein image, the principle of the algorithm is as following:

Step 1: Convolution $Fgray(i)$ (i=1, 2, ---, 8) of each pixel within the 9×9 window in image were calculated by corresponding eight direction Operator (As shown in **Figure 3**). Then get the largest convolution $G\max$ in eight directions.

$$G\max = \underset{i}{Max}(Fgray(i)) \quad (12)$$

Then, maximum $G\max$ is gray value of the point

$$Gray(m,n) = G\max \quad (13)$$

Step 2 Threshold segmentation

Step 2.1 The first threshold segmentation

$$Gray(m,n) = \begin{cases} Gray(m,n) & if\ \ Gray(m,n) > 0 \\ 0 & otherwise \end{cases} \quad (14)$$

Step 2.2 The second threshold segmentation

$$Gmean = sum(Gray)/Num$$

$$Gray(m,n) = \begin{cases} Gmean & if\ \ Gray(m,n) > Gmean \\ Gray(m,n) & otherwise \end{cases} \quad (15)$$

$Gmean$ is the average of non-zero elements in the image. $sum(Gray)$ and Num expresse the sum and number of non-zero elements respectively.

Step 2.3 Fuzzy enhancement

After the previous twice segmentation, then range of the gray value is $[0, Gmean]$, pseudo-vein characteristics and noise are likely to exist in the region, cleared the fuzzy part by using fuzzy enhancement operator. This will further reduce the noise and removed pseudo-vein. The algorithm are as following:

1) Calculate the degree of membership, namely:

$$u_{mn} = G(Gray(m,n)) = \frac{Gray(m,n)}{K-1} \quad (16)$$

2) Calculate the means T_{mn} of all the elements within $(2p+1)\times(2p+1)$ window

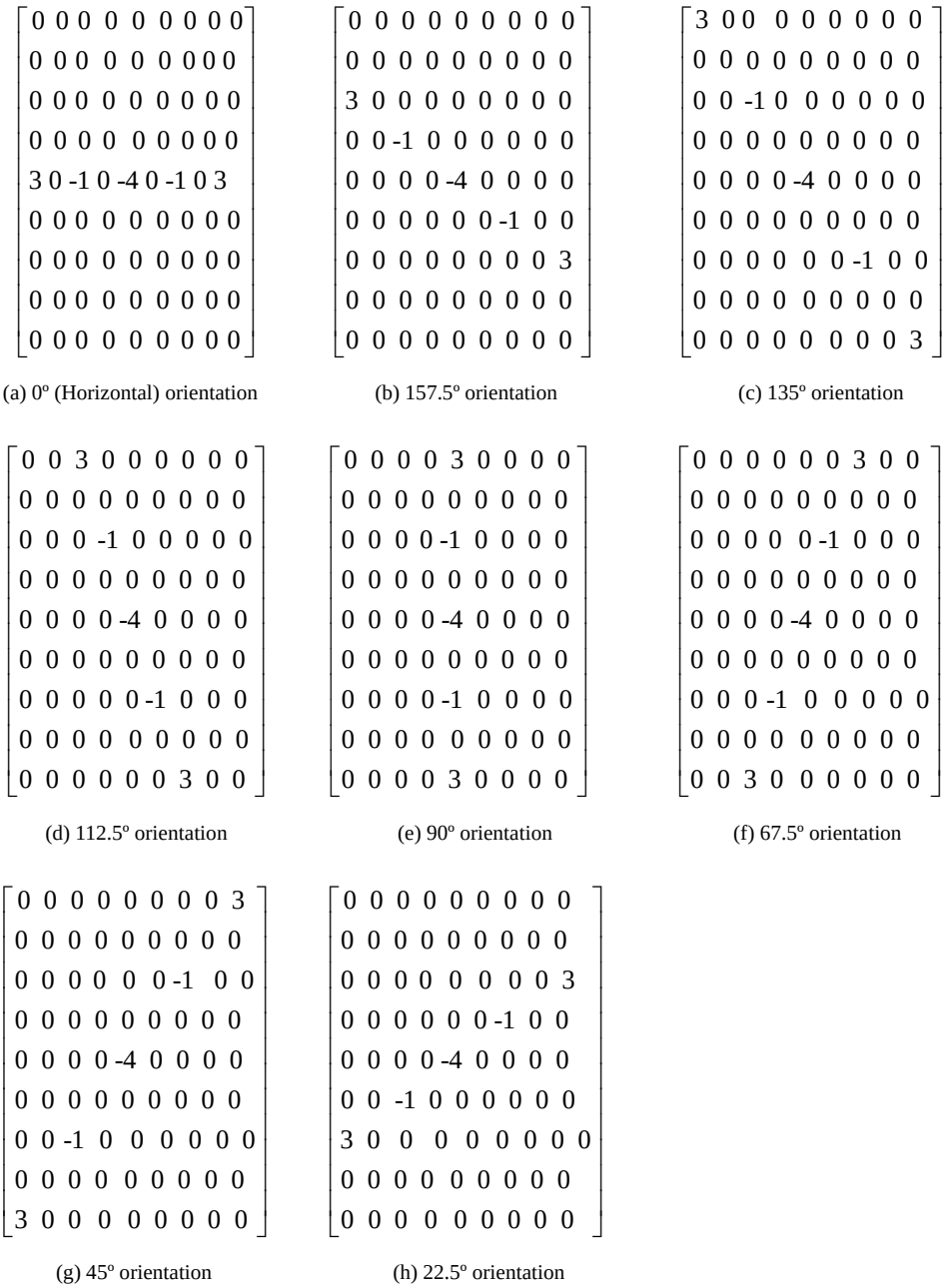

(a) 0º (Horizontal) orientation (b) 157.5º orientation (c) 135º orientation

(d) 112.5º orientation (e) 90º orientation (f) 67.5º orientation

(g) 45º orientation (h) 22.5º orientation

Figure 3. The direction of the operator.

3) Calculate pixel gray $Gray(m,n)'$ and gray degree of membership u'_{mn} adjusted within $(2p+1)\times(2p+1)$ window, its mathematical expression is

$$u'_{mn}=\begin{cases} u_{mn}\left(\dfrac{u_{mn}}{T_{mn}}\right)^{2^r} & if\ u_{mn}\le T_{mn} \\ 1-(1-u_{mn})\left(\dfrac{1-u_{mn}}{1-T_{mn}}\right)^{2^r} & if\ u_{mn}>T_{mn} \end{cases} \quad (17)$$

$$Gray(m,n)'=(K-1)u'_{mn}$$

Step 2.4 The third threshold segmentation

Use $(2p+1)\times(2p+1)$ window sliding in the original image, pixel gray value in the window center is $Gray(m,n)'$, then all the pixels within the window compose of a set as the following:

$$S(i,j)=\{f(m+k,n+l)|k,l=-p,\cdots,-1,0,1,\cdots,p\}$$

Obtained the average $Average(S(m,n))$ of all pixels in the window.

Formula as follows

$$Average(S(m,n)) = \frac{1}{(2p+1)(2p+1)} \sum_{m=-p}^{p} \sum_{n=-p}^{p} Gray(m,n)' \tag{18}$$

$$\sigma(m,n) = \sqrt{\frac{1}{(2p+1)(2p+1)} \sum_{m=-p}^{p} \sum_{n=-p}^{p} (Gray(m,n)' - Average(S(m,n)))^2} \tag{19}$$

$$T(m,n) = Average(S(m,n)) + \alpha \times \sigma(m,n) \tag{20}$$

So each pixel of images has a threshold value. The binary images obtained by the each respective threshold values are

$$Gray(m,n)' = \begin{cases} 1 & if\ Gray(m,n)' > T(m,n) \\ 0 & otherwise \end{cases} \tag{21}$$

Obtaining the final image $Gray(m,n)'$ only containing the vein characteristics.

It is obvious that the grain of the original image has been got as **Figure 4**. The effect is comparatively ideal. Median filtering method can eliminate burrs and make the borderline smooth. In addition, because the result of the new threshold dispose algorithm inducts massive noises, these noises are wiped off according to the size of them in this paper. The effect of filtering is as shown in **Figure 5**.

2.6. Lmage Thinning

In this paper, we thin the vein image using the combination method of general conditional thinning and templates. Get rid of the special un-single pixel point after the general conditional thinning.

a) The conditional thinning algorithm [22]

Region points are assumed to have value 1 and background points to have value 0. The method consists of successive passes of two basic steps applied to the contour points of the given region, where a contour point is any pixel with value 1 and having at least one 8-neighbor valued 0. With reference to 8-neighborhood notation shown in **Figure 6**, Step 1 flags a contour point p_1 for deletion if the following conditions are satisfied:

$$\begin{cases} (a) & 2 \le N(p_1) \le 6 \\ (b) & T(p_1) = 1 \\ (c) & p_2 \bullet p_4 \bullet p_6 = 0 \\ (d) & p_4 \bullet p_6 \bullet p_8 = 0 \end{cases} \tag{22}$$

where $N(p_1)$ is the number of nonzero neighbors of p_1, that is,

$$N(p_1) = p_2 + p_3 + \cdots + p_8 + p_9 \tag{23}$$

And $T(p_1)$ is the number of 0-1 transitions in the ordered sequence $p_2, p_3, \cdots, p_8, p_9, p_2$. For example, $N(p_1) = 4$, $T(p_1) = 3$ in **Figure 7**.

In step 2, conditions (a) and (b) remain the same, but conditions (c) and (d) are changed to

$$\begin{cases} (c') & p_2 \bullet p_4 \bullet p_6 = 0 \\ (d') & p_4 \bullet p_6 \bullet p_8 = 0 \end{cases} \tag{24}$$

Thus one iteration of the thinning algorithm consists of: 1) applying step 1 to flag the remaining border points for deletion; 2) deleting the flagged points; 3) applying step 2 to flag the remaining border points for deletion; (4) deleting the flagged points. This basic pro cedure is app-

p_9	p_2	p_3
p_8	p_1	p_4
p_7	p_6	p_5

Figure 6. Neighborhood arrangement used by the thinning algorithm.

0	0	1
1	p_1	0
1	0	1

Figure 7. Illustration of condition (a) and (b) in Eq.(22) (In this case, $N(p_1) = 4$, $T(p_1) = 3$).

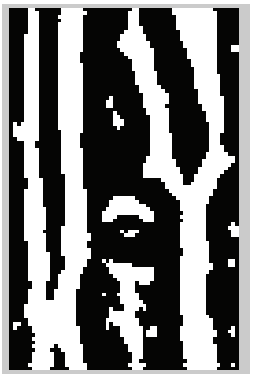

Figure 4. Segmentation.

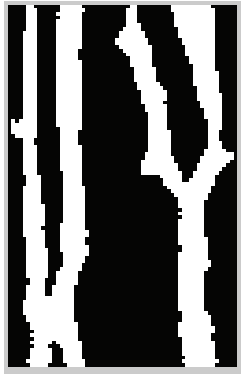

Figure 5. Filtering.

lied iteratively until no further points are deleted, at which time the algorithm terminates, yielding the skeleton of the region.

b) The improved thinning algorithm

The improved thinning algorithm is on the base of the conditional thinning. On the conditional thinning image, the template algorithm is added to get rid of the un-single pixel point in this paper.

For the case of **Figure 8**, the un-single pixel point is pointed by the red line. We must think of one method to get rid of the pixels point, because they are the superabundance points in the image. There are two methods to get rid of it. One is that the image can still be assured the connectivity after getting out of these points. These points can be deleted according to the connection of 4- neighborhood and 8-neighborhood. The other uses the method of templates. The templates are as follow **Figure 9**. The center of template is the reference point.

The center of template is the reference point *. "1" is the point of target image, "0"is the point of background image, the points of **Figure 6** which satisfy conditions will be dispelled by the templates Me, Mf, Mg, Mh. Do iteration based on the conditional thinning image until the un-single pixel points of the first class are dispelled completely.

c) Burr cutting

The noise and shadow of original finger vein image will produce "Burr" in the skeleton image, and it will affect the following processing. "Burr" can be dispelled by recording the amount of the un-single pixel points from each endpoint to the bifurcation points, and then select a threshold. The value of the un-single pixel points whose amount is less than threshold amounts 0, contrarily, the value keeps constant. Image thinning is shown in **Figure 10**.

3. EXTRACTION OF MINUTIAE POINTS

The branching points and the ending points in the vein pattern skeleton image are the two types of critical points to be extracted. To obtain the junction points from the skeleton of vein patterns, we run the following pixel-wise operation commonly known as the cross number concept [21]: For a 3×3 region (as follow **Figure 11**), If p_0 is 1, and the number of transition

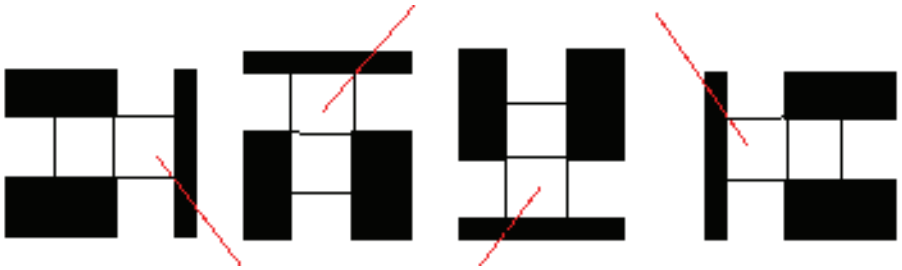

Figure 8. The un-single pixel points of the first kind.

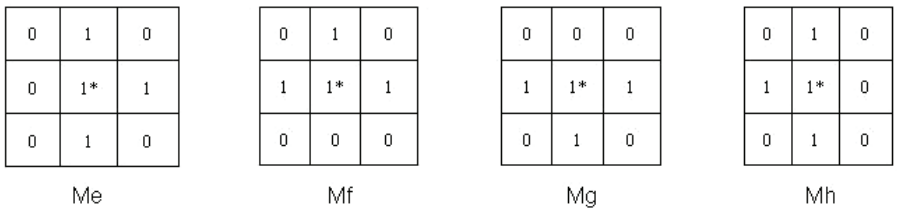

Figure 9. The un-single pixel point templates of the first kind.

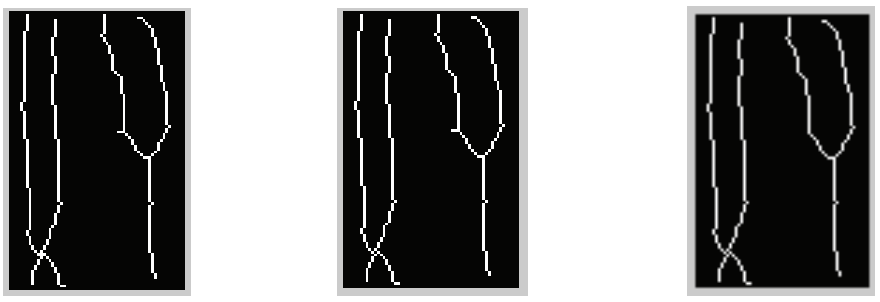

(a) General conditional thinning (b) Improved thinning algorithm (c) Burr cutting

Figure 10. Image Thinning.

p_1	p_2	p_3
p_8	p_0	p_4
p_7	p_6	p_5

Figure 11. 3×3 region.

N_{trans} between 0 and 1 (and vice versa) from p_1 to p_8 is greater than or equal to 6, then p_0 is a junction point. Mathematically, this can be expressed with the following equation:

$$N_{trans} = \sum_{i=1}^{8} \left| p_{i+1} - p_i \right| , \text{ where } \quad p_9 = p_1$$

A similar approach can be applied to find the ending points. The difference is that the number of transition N_{trans} for an ending point is now exactly 2. The flowchart of the fingerprint enhancement algorithm is shown in **Figure 12** and experimental process is shown in **Figure 13**.

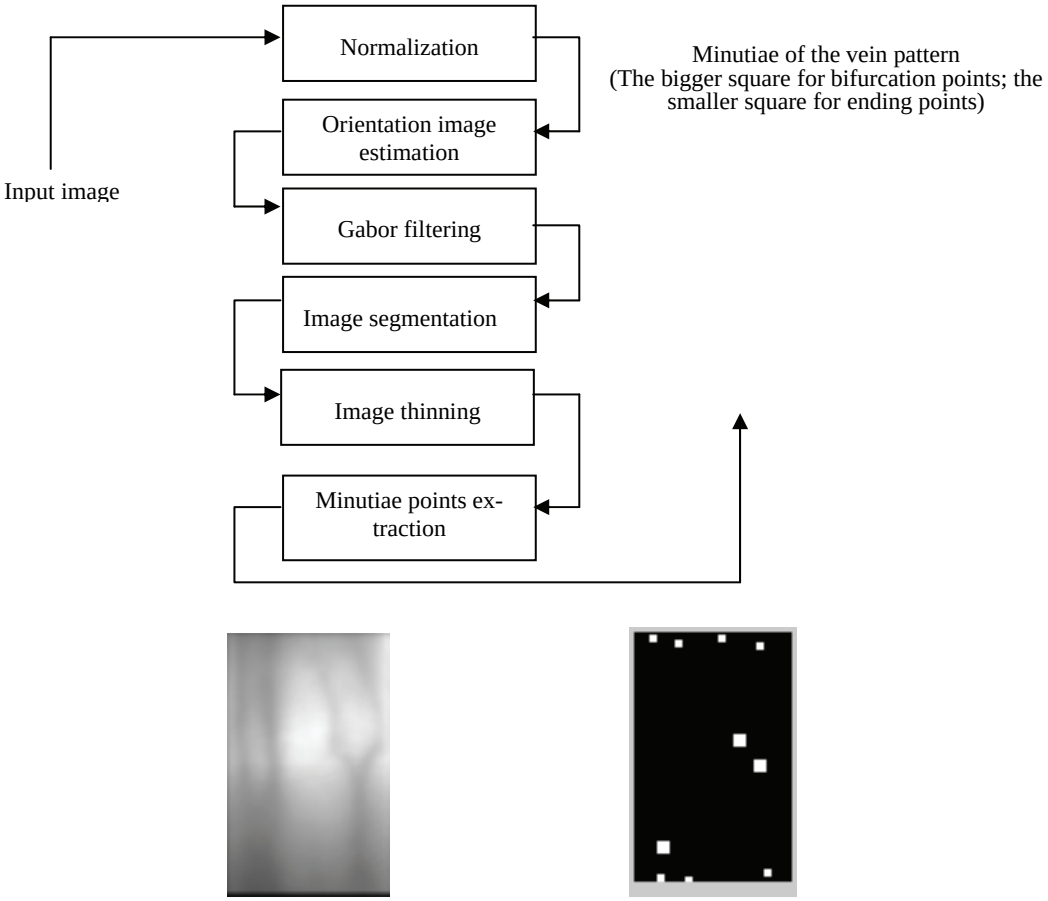

Figure 12. A Flowchart of the proposed finger-vein processing algorithm.

(a) (b) (c) (d) (e) (f) (g) (h) (i)

Figure 13. Outputs of different stages of the algorithm. (a) Input image (b) Orientation image estimation (c) Gabor filtering (d) Image segmentation (e) Filtering (f) General conditional thinning (g) Improved thinning algorithm (h) Burr cutting (i) Minutiae points extraction.

4. EXPERIMENT RESULT

Experiment on our finger-vein dataset: In this section, three experiments conducted to demonstrate the performance of the proposed method for object recognition. Our finger-vein database comprises of 50 distinct subjects, each subject having 10 different images, taken at different times. The images are subject to variations such as lighting. All the images are taken against a dark homogeneous background and the Finger are in upright, frontal position (with a tolerance for some side movement). The images are 256 grey levels per pixel and normalized to 328×376 pixels. These images are pre-processed by our method before matching experiment.

4.1. Verification Using MHD

Many techniques can be applied to the analysis of minutiae of vein pattern in a similar manner to those applied to fingerprint minutiae. However, due to the fact that the number of minutiae for the vein pattern is relatively small compared to those for fingerprints, analysis based on geometrical information is preferred to statistical features. Since the vein pattern is represented as a set of two-dimensional points, matching of a pair of such pattern can be achieved by measuring the Hausdorff distance between the two minutiae sets.

The original Hausdorff distance was proposed for comparing two binary images by Huttenlocher et al. [23]. The computation of Hausdorff distance does not require point correspondences between the two point sets. They proposed efficient computational algorithms for speeding up the process of finding similar patterns in an image by searching the regions with the smallest Hausdorff distances in the image [6]. For two point sets $X=\{x_1,x_2,x_3,\cdots,x_{N_x}\}$ and $Y=\{y_1,y_2,y_3,\cdots,y_{N_y}\}$, Eqs. (25) and (26) give the definition for a Hausdorff distance, where HD and h are the undirected and directed Hausdorff distance for the two point sets, respectively. The smaller the value of HD, the more similar the two point sets are

$$HD(X,Y)=\max\left(d(X,Y),d(Y,X)\right) \tag{25}$$

$$d(X,Y)=\max_{x_i\in X}\min_{y_j\in Y}\left\|x_i-y_j\right\| \tag{26}$$

However, the original Hausdorff distance method is sensitive to small perturbations in point locations for shape alignment. To overcome the weakness of the Hausdorff distance, the modified Hausdorff distance (MHD) [12] for matching two objects is developed and has the following desirable properties: 1) its value increases monotonically as the amount of difference between the two sets of points increases, and 2) it is robust to outlier points that might result from segmentation errors. Unlike the original form, the undirected MHD is defined as in Eq. (27)

$$d(X,Y)=\frac{1}{N_X}\sum_{x_i\in X}\min_{x_i\in Y}\left\|x_i-y_i\right\| \tag{27}$$

Figure 13 shows the false acceptance rate (FAR) and false rejection rate (FRR) curves, from which it can be seen that when the threshold value for the distance measure HD is 0.52, the equal error rate (EER) is approximately 14.51%. An experiment with the MHD was carried out on the same data set, and the algorithm achieves 0.761% EER (as shown in **Figure 14**).

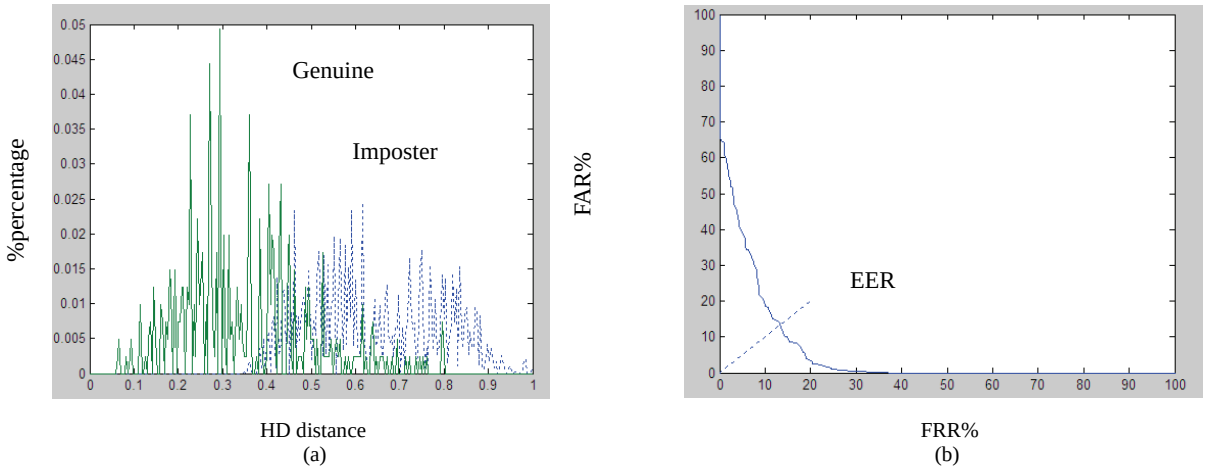

Figure 13. Verification test results. (a) Genuine and imposter distributions and (b) Error rate for minutiae recognition using the original form of Hausdorff distance (EER = 14.51% where the threshold is observed to be 0.52)

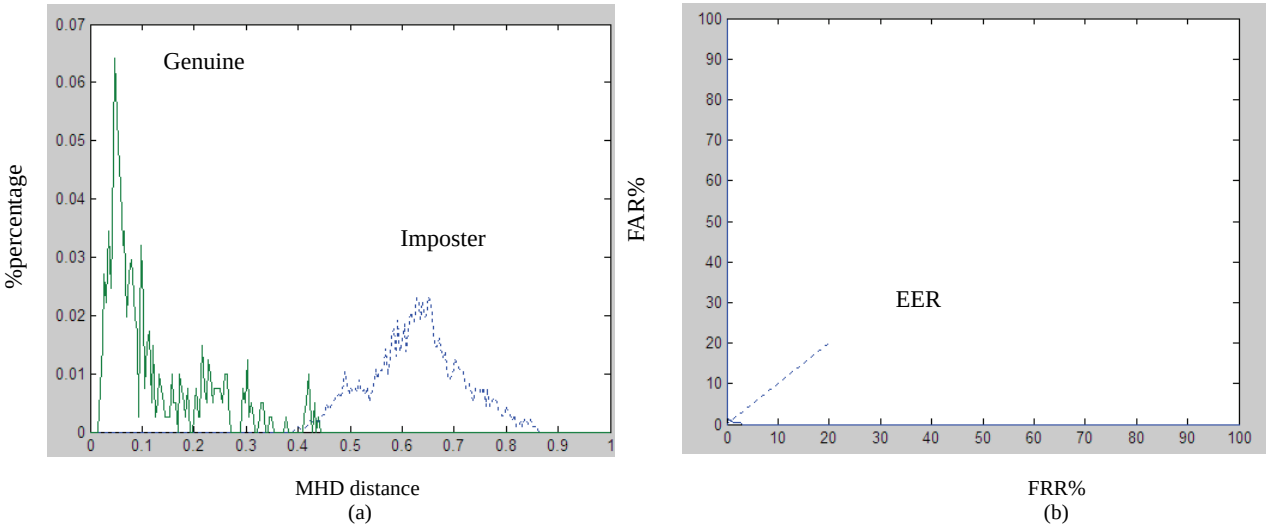

(a) Genuine and imposter distributions and (b)Error rate for minutiae recognition using MHD (EER = 0.761% where the threshold is observed to be 0.43)

Figure 14. Verification test results.

4.2. Verification Using Shape of the Vein Patterns

To verify that minutiae points can best represent the shape of the vein patterns for vein recognition, in the following, we show some experimental results of applying the proposed robust image matching algorithm to the skeleton representation of the vein pattern. The experiments utilize the same MHD to measure the similarity. **Figure 15** shows FAR and FRR curves, from which it can be seen that when the threshold value for the distance measure HD is 0.41, the equal error rate (EER) is approximately 7%. **Table 1** contains the results for the evaluation, which shows that while the shape of the vein patterns can reach relatively high recognition accuracy, the minutiae can further increase the accuracy and require less time.

4.3. Two Types of Minutiae

To evaluate the usefulness of the two types of minutiae, namely bifurcation and ending points, we carried out three sets of personal verification experiments: firstly with the bifurcation points only, and then with ending points only, and finally the combination of the two minutiae types. The three sets of experiments utilize the same MHD to measure the similarity. **Table 2** contains the results for the evaluation, which shows that while the bifurcation and ending points can reach relatively high recognition accuracy, the combination of the two minutiae can further increase the accuracy, which is advantage especially when high feature discriminating power is desired for a large population group.

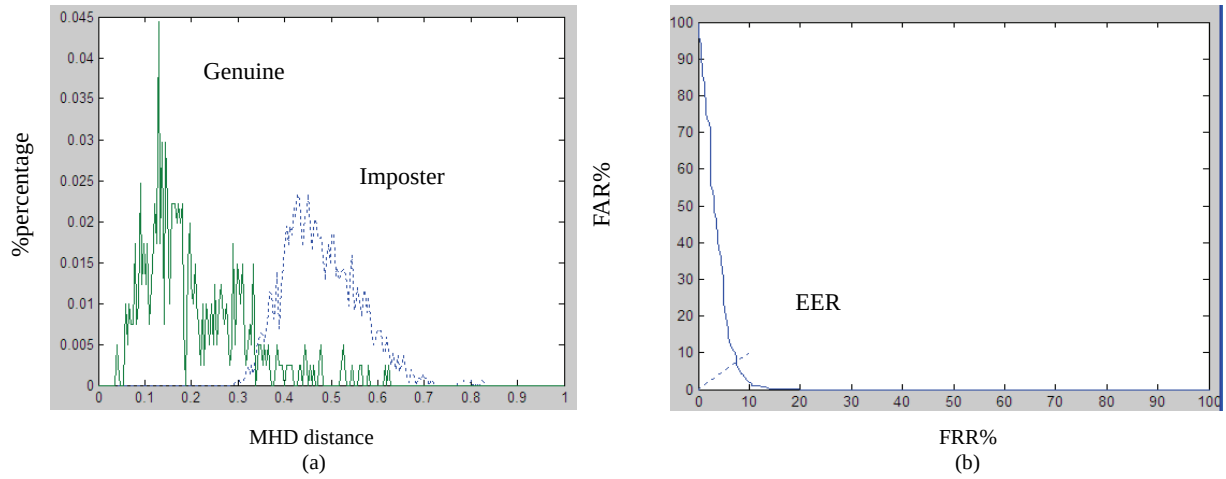

Figure 15. Error rate curves for minutiae recognition using MHD (EER = 7% where the threshold is observed to be 0.41).

Table 1. Minutiae and shape of the vein patterns evaluation using MHD.

	Equal error rate (%)	Threshold value	Time(s)
Shape of the vein patterns	7	0.41	6.5
Combination of both minutiae	0.761	0.43	2.2

Table 2. Minutiae evaluation using MHD.

	Equal error rate (%)	Threshold value
Bifurcation points only	9.20	0.48
Ending points only	8.89	0.46
Combination of both minutiae	0.761	0.43

5. CONCLUSIONS

This paper proposes a novel method applicable to finger-vein recognition. Firstly, we extract the features of the vein patterns for recognition. Secondly, the minutiae features are extracted from the vein patterns for recognition, which include bifurcation points and ending points. These feature points are used as a geometric representation of the shape of vein patterns. Finally, the modified Hausdorff distance algorithm is proposed to evaluate the discriminating between all possible relative positions of the shape of vein patterns. Experimental results show the equal error rate (EER) reaches 0.761% where the threshold value for the distance measure HD is observed to be 0.43. This result indicates the minutiae features in the vein patterns can be used as a feature sets in the personal verification applications efficiently.

Though the current database is relatively small and it is not adequate to draw any firm conclusion on the discriminating power of vein patterns for a large population (in terms of millions of users) group, the experiments do show the potential of the minutiae of the vein patterns as a biometric feature for personal verification applications in a reasonable sized user group. The results presented here indicate, as a new identity authentication technology, the vein recognition has a better long term potential, need to be studied further, and can be applied to the lives of people better.

6. ACKNOWLEDGMENTS

This article belongs to science and technology research item of Chongqing education committee (KJ070620). The authors are also most grateful for the constructive advice and comments from the anonymous reviewers.

REFERENCES

[1] Z. B. Zhang, S. L. Ma, and X. Han, (2006) Multiscale feature extraction of finger-vein patterns based on curvelets and local interconnection structure neural network, The 18th International Conference on Pattern Recognition (ICPR'06).

[2] K. Kanagawa, (2006) Finger vein authentication technology and its future junichi hashimoto, Information & Telecommunication Systems Group, Japan IEEE.

[3] A. Jain, R. M. Bolle, and S. Pankanti, (1999) Biometrics: Personal identification in networked society, Kluwer Academic Publishers, Dordrecht.

[4] P. MacGregor and R. Welford, (1991) Veincheck: Imaging for security and personnel identification, Adv. Imaging **6 (7),** 52–56.

[5] P. L. Hawkes and D. O. Clayden, (1993) Veincheck research for automatic identification of people, in: Presented at the Hand and Fingerprint Seminar at NPL.

[6] L.Y. Wanga, G. Leedhamb, and D. S. Y. Choa, (2007) Minutiae feature analysis for infrared hand vein pattern biometrics, Pattern Recognition Society, Published by Elsevier Ltd, All rights reserved.

[7] J. A. Gualtieri, J. L. Moigne, and C. V. Packer, (1992) Distance between images, Fourth Symposium on the Frontiers of Massively Parallel Computation, 216–223.

[8] J. You, E. Pissaloux, J. L. Hellec, and P. Bonnin, (1994) A guided image matching approach using Hausdorff distance with interesting points detection, Proceedings of the IEEE International Conference on Image Processing, **1**, 968–972.

[9] V. D. Gesù and V. Starovoitov, (1999) Distance-based functions for image comparison, Pattern Recognition Lett, **20 (2)**, 207–214.

[10] A. Ghafoor, R. N. Iqbal and S. Khan, (2003) Robust image matching algorithm, Proceedings of the Fourth EURASIP Conference Focused on Video/Image Processing and Multimedia Communications, 155–160.

[11] V. Perlibakas, (2004) Distance measures for PCA-based face recognition, Pattern Recognition Lett, **25(6)**, 711–724.

[12] M. P. Dubuisson and A. K. Jain, (1994) A modified Hausdorff distance for object matching, Proceedings of the 12th IAPR International Conference on Pattern Recognition, **1**, 566–568.

[13] J. Paumard, (1997) Robust comparison of binary images, Pattern Recognition Lett, **18(10)**, 1057–1063.

[14] B. Takács (1998), Comparing face images using the modified Hausdorff distance, Pattern Recognition, **31(12)**, 1873–1881.

[15] B. Guo, K.-M. Lam, K.-H. Lin, and W. C. Siu, (2003) Human face recognition based on spatially weighted Hausdorff distance, Pattern Recognition Lett, **24(1–3)**, 499–507.

[16] K.-H. Lin, K.-M. Lam, and W. C. Siu, (2003) Spatially eigen-weighted Hausdorff distances for human face recognition, Pattern Recognition, **36(8)**, 1827–1834.

[17] Z. Zhu, M. Tang, and H. Lu, (2004) A new robust circular Gabor based object matching by using weighted

Hausdorff distance, Pattern Recognition Lett, **25(4)**, 515−523.

[18] L. Hong, Y.F. Wan, and A. Jain, (1998) Fingerprint image enhancement: algorithm and performance evaluation, IEEE Transactions on Pattern Analysis and Machine Intelligence, **20(8)**.

[19] D. Marr, (1982) Vision, San Francisco, Calif.: W. H. Freeman.

[20] J. G. Daugman, (1993) High confidence visual recognition of persons by a test of statistical independence, IEEE Trans, Pattern Analysis and Machine Intelligence, **15(11)**, 1148−1161.

[21] U. Halici, L. C. Jain, and A. Erol, (1999) An introduction to fingerprint recognition, in: L. C. Jain, U. Halici, I. Hayashi, S. B. Lee, S. Tsutsui (Eds.), Intelligent Biometric Techniques in Fingerprint and Face Recognition, CRC Press, Boca Raton, FL, 3−34.

[22] R. C. Gonzalez, (2005) Digital Image Processing, Publishing House of Electronics Industry, Beijing.

[23] D. P. Huttenlocher, G. A. Klanderman, and W. J. Rucklidge, (1993) Comparing images using the Hausdorff distance, IEEE Trans. Pattern Anal. Mach. Intell, **15(9)**, 850−863.

[24] E. P. Vivek and N. Sudha, (2007) Robust Hausdorff distance measure for face recognition, Pattern Recognition, Elsevier, **40(2)**, 431−442.

[25] E. P. Vivek and N. Sudha, (2006) Gray Hausdorff distance measure for comparing face images, IEEE Transactions on Information, Forensics and Security, **1(3)**, 342−349.

[26] M. Sezgin and B. Sankur, (2004) Survey over image thresholding techniques and quantitative performance evaluation [J], Journal of Electronic Imaging, **11**.

[27] S. Lachance, R. Bauer, and A. Warkentin, (2004) Application of region growing method to evaluate the surface condition of grinding wheels, International Journal of Machine Tools and Manufacture, **44(7−8)**, 823−829.

[28] R. Saurel, F. Petitpas, and R. A. Berry, (2009) Simple and efficient relaxation methods for interfaces separating compressible fluids, cavitating flows and shocks in multiphase mixtures, Journal of Computational Physics, **228(5)**, 20 March, 1678−1712.

[29] C. C. Kang and W. J. Wang, (2007) A novel edge detection method based on the maximizing objective function, Pattern Recognition, **40(2)**, 609−618.

[30] Z. B. Zhang, D. Y. Wu, S. L. Ma, and J. Ma, (2005) Multiscale feature extraction of finger-vein patterns based on wavelet and local interconnection structure neural networks and brain,. ICNN&B'05, **2(13−15)**, 1081−1084.

[31] V. Barra, (2006) Robust segmentation and analysis of DNA microarray spots using an adaptative split and merge algorithm, Computer Methods and Programs in Biomedicine, **81(2)**, 174−180.

[32] J. M. Lu, X. Yuan, and T Yahagi, (2006) A method of face recognition based on fuzzy clustering and parallel neural networks, Signal Processing, **86(8)**, 2026−2039.

J. Biomedical Science and Engineering, 2009, 2, 273-279 **JBiSE**
doi: 10.4236/jbise.2009.24041 Published Online August 2009 (http://www.SciRP.org/journal/jbise/).

Determination of inter- and intra-subtype/species variations in polymerase acidic protein from influenza A virus using amino-acid pair predictability

Shaomin Yan[1], Guang Wu[2]*

[1]National Engineering Research Center for Non-food Biorefinery, Guangxi Academy of Sciences, 98 Daling Road, Nanning, Guangxi, 530007, China; [2]Computational Mutation Project, DreamSciTech Consulting, 301, Building 12, Nanyou A-zone, Jiannan Road, Shenzhen, Guangdong Province 518054, China.
Email: hongguanglishibahao@yahoo.com

Received 23 March 2009; revised 15 April 2009; accepted 28 April 2009.

ABSTRACT

The polymerase acidic protein is an important family of proteins from influenza A virus, which is classified as many different subtypes or species. Thus, an important question is if these classifications are numerically distinguishable with respect to the polymerase acidic protein. The amino-acid pair predictability was used to transfer 2432 polymerase acidic proteins into 2432 scalar data. The one-way ANOVA found these polymerase acidic proteins distinguishable in terms of subtypes and species. However, the large residuals in ANOVA suggested a possible large intra-subtype/species variation. Therefore, the inter- and intra-subtype/species variations were studied using the model II ANOVA. The results showed that the intra-subtype/species variations accounted most of variation, which was 100% in total for both inter- and intra- subtype/species variations. Our analysis threw lights on the issue of how to determine a wide variety of patterns of antigenic variation across space and time, and within and between subtypes as well as hosts.

Keywords: Amino-Acid Pair; Influenza A Virus; Inter- and Intra-; Model II ANOVA; Polymerase Acidic Protein; Species; Subtype; Variation

1. INTRODUCTION

The unpredictable mutations in proteins from influenza A virus threaten the humans with possible pandemics or epidemics, therefore it is considered important to accurately, precisely and reliably predict the mutations. In this way, the new vaccines, which would be more effective against the influenza A virus, could be manufactured [1,2,3,4,5,6].

Currently, the manufactured vaccines are designed to target the influenza A virus according to their subtypes, for example, the focus in recent year would be the H5N1 subtype of influenza A virus [7,8,9,10,11,12,13,14], and anti-flu drugs are designed to target neuraminidases and M2 protein [15,16]. It would be understandable that proteins should be different from one subtype to another. Otherwise, there would be no classification of subtype. Moreover, the proteins under the same subtype should be different one another, otherwise a single subtype would contain only a single protein. The same holds for proteins classified according to species, where the sample was obtained.

Here, an important question is if these classifications are numerically distinguishable, say, if a protein is different from species to species and from subtype to subtype in number. This is the base for prediction of mutation using mathematical modeling.

However this work has yet to be done, because the difference between proteins is different in terms of letters, which represent the amino acids in proteins. It is difficult to use any statistical method to determine these differences cross a protein family.

For this aim, it needs to transfer a protein into a datum that should be different from protein to protein. Then it would be possible to conduct an ANOVA statistics to answer the question above.

Actually there are quite a few methods, which can transfer a protein sequence into a series of numerical codes or numerical sequence for predicting its various attributes (see, e.g., [17,18,19,20,21,22,23,24,25]).

Since 1999, we have developed three approaches to transfer each amino acid in a protein as well as a whole protein (for reviews, see [26,27,28]) into either a single datum or numerical sequence, which resulted in many studies on proteins.

Afterward, another question would be the inter- and intra-subtype/species variations. This issue is important because the vaccines and anti-flu drugs manufactured based on subtype would be more efficient and effective if the difference within subtype/species would be smaller

than that between subtypes/species.

Influenza viruses replicate and transcribe their segmented negative-sense single-stranded RNA genome in the nucleus of the infected host cell. All RNA synthesizing activities associated with influenza virus are performed by the virally encoded RNA-dependent RNA polymerase that consists of three subunits, polymerase acidic protein (PA), polymerase basic proteins 1 and 2 [29]. The PA subunit is involved for the conversion of RNA polymerase from transcriptase to replicase [30] and contains the endonuclease active site. A recent study strongly implicates the viral RNA polymerase complex as a major determinant of the pathogenicity of the 1918 pandemic virus [31].

Many studies have indicated that sequence-based prediction approaches, such as protein subcellular location prediction [32,33,34], protein quaternary attribute prediction [25,35], identification of membrane proteins and their types [36,37], identification of enzymes and their functional classes [38], identification of GPCR and their types [24,39,40], identification of proteases and their types [41,42], protein cleavage site prediction [43,44,45], signal peptide prediction [46,47], and protein 3D structure prediction based on sequence alignment [48], can timely provide very useful information and insights for both basic research and drug design.

The present study was attempted to use the model II ANOVA to investigate the inter- and intra- subtype/species variations in polymerase acidic protein from influenza A virus in hope to shed lights on helping find effective drugs against influenza A virus.

2. MATERIALS AND METHODS

2.1. Data

A total of 5165 full-length PA sequences of influenza A virus sampled from 1918 to 2008 was obtained from the influenza virus resources [49]. After excluded identical sequences, 2432 PA proteins were used in this study.

2.2. Transferring Symbolized PA Proteins into Scalar Data

Among these methods developed by us, the amino-acid pair predictability is the simplest, which was thus used in this study. According to the permutation, the adjacent amino-acid pairs in a protein can be classified as predictable and unpredictable, which provided a measure to distinguish protein one another and was used in many our previous studies (for example 2008, [28,50,51,52,53,54]).

For example, there was an avian influenza virus (strain A/quail/Hong Kong/1721-20/99(H6N1)) and its PA was composed of 716 amino acids (accession number CAC84865). The first and second amino acids could be counted as an amino-acid pair, the second and third as another amino-acid pairs, the third and fourth, until the 715th and 716th, thus there were 715 amino-acid pairs. Then, how many amino-acid pairs can be explained by the permutation or random mechanism in this PA? This can be determined using the percentage of predictable and unpredictable amino-acid pairs.

There were 37 aspartic acids "D" and 76 glutamic acids "E" in CAC84865 PA. If the permutation could explain the appearance of amino-acid pair DE, it could appear four times in this PA (37/716×76/715×715=3.927). Actually there were 4 DEs in this PA. Thus, the appearance of DE could be explained by permutation or predicted by random mechanism. By clear contrast, there were 50 isoleucines "I" in the PA. If the permutation could explain the appearance of IE, it could appear five times (50/716×76/715×715=5.307). However, it appeared 12 times in realty, which could not be explained by permutation or randomly unpredictable. In this way, all amino-acid pairs in this PA could be classified as predictable and unpredictable. For this particular PA, its predictable and unpredictable portions were 25.45% and 74.55%.

Taking another PA (accession number CAC84866) as example, this PA had only one amino acid different from CAC84865 PA at position 437. However, its predictable and unpredictable portions were 25.59% and 74.41%. Thus, the amino-acid pair predictability distinguished the difference between different PA proteins as a very sensitive measure.

2.3. Difference among Subtypes/Species

Influenza A viruses are classified by the serological subtypes of the primary viral surface proteins. Currently, there are 16 haemagglutinin subtypes from H1 to H16 and 9 neuraminidase subtypes from N1 to N9 [55]. Also, influenza A viruses can be classified according to their host.

After computation of 2432 PA proteins, the predictable portions of PA proteins were grouped according to their classifications of subtypes and species.

As there were more than two subtypes and two species, and the number of PA proteins was highly different from subtype to subtype, and from species to species, the one-way ANOVA followed by the Holm-Sidak's comparison test was used to compare the difference among and between subtypes/species using the SigmaStat software [56]. $P < 0.05$ was considered statistically significant.

2.4. Inter- and Intra-Subtype Variation

The single classification model II ANOVA with unequal sample sizes [57] was used to determine the inter- and intra-subtype/species variations.

3. RESULTS AND DISCUSSION

The one-way ANOVA showed that there were statistically significant difference among HA subtypes (**Figure 1**), NA subtypes (**Figure 2**) and species (**Figure 3**). Even the statistical difference was found between subtypes and between species. The detailed results were listed in Supplementary results.

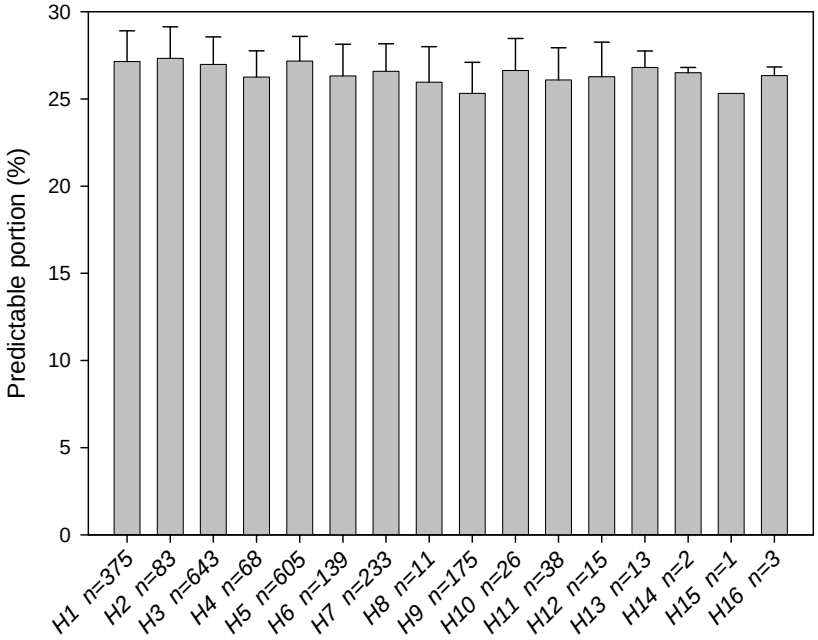

Figure 1. HA subtype comparison of PA proteins from influenza A viruses. The one-way ANOVA indicated a statistically significant difference ($P < 0.001$) among sixteen subtypes, and the Holm-Sidak's comparison test indicated the statistical difference between two subtypes as follows: H5 versus H9, H1 versus H9, H3 versus H9, H2 versus H9, H7 versus H9, H5 versus H6, H6 versus H9, H1 versus H6, H5 versus H7, H2 versus H6, H5 versus H4, H3 versus H6, H1 versus H4, H1 versus H7, H2 versus H4, H4 versus H9, H5 versus H11, H2 versus H11, H10 versus H9, H1 versus H11, H2 versus H7, H3 versus H4, H3 versus H11, H13 versus H9, H3 versus H7, H11 versus H9, H2 versus H8, H5 versus H8, H1 versus H8, H2 versus H12, H12 versus H9, H5 versus H12, H5 versus H3, H3 versus H8, and H1 versus H12.

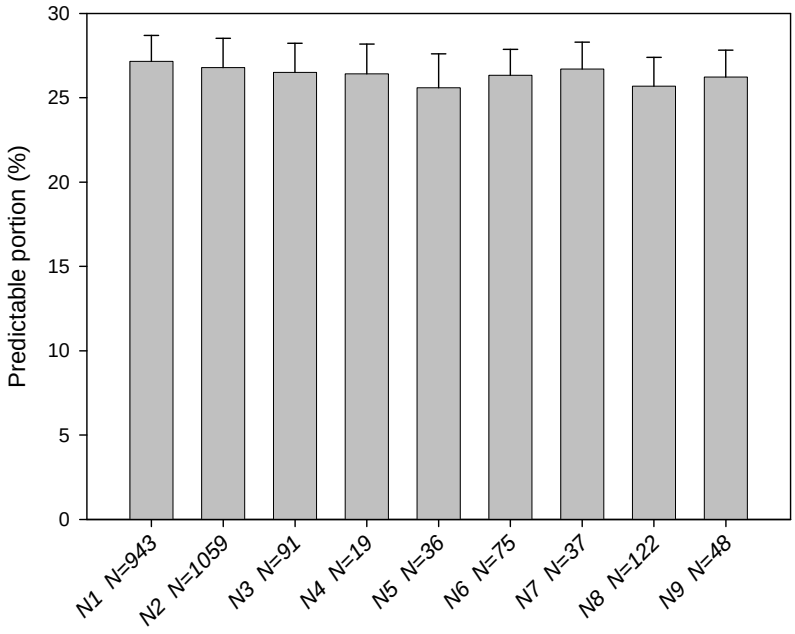

Figure 2. NA subtype comparison of PA proteins from influenza A viruses. The one-way ANOVA indicated a statistically significant difference ($P < 0.001$) among nine subtypes, and the Holm-Sidak's comparison test indicated the statistical difference between two subtypes as follows: N1 versus N8, N2 versus N8, N1 versus N5, N1 versus N2, N2 versus N5, N1 versus N6, N1 versus N9, N1 versus N3, N3 versus N8, N7 versus N8, N7 versus N5, N3 versus N5, N6 versus N8, N2 versus N6, N2 versus N9 and N6 versus N5.

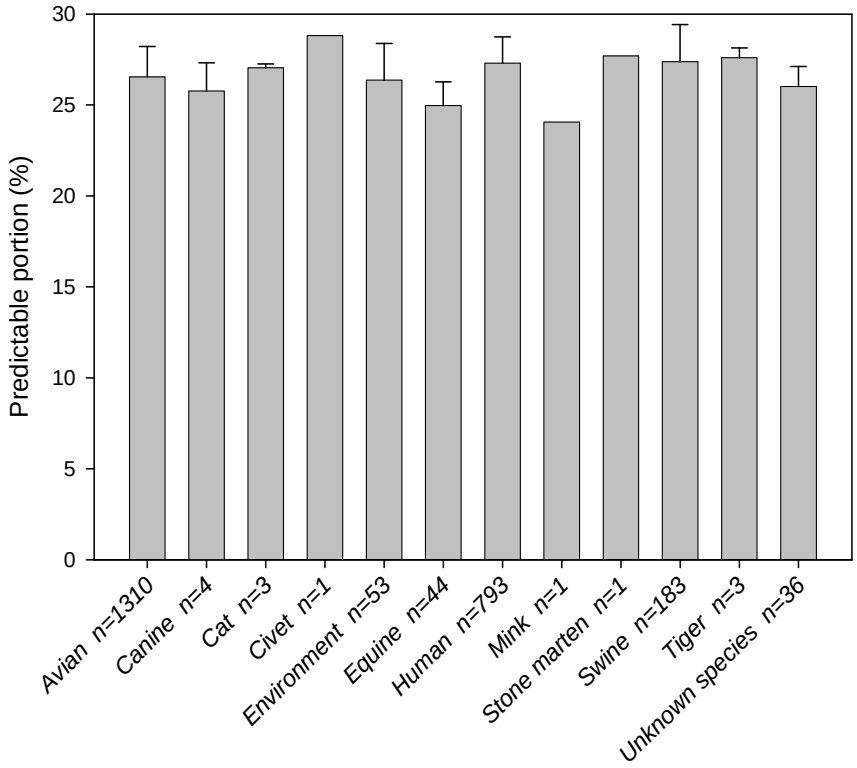

Figure 3. Species comparison of PA proteins from influenza A viruses. The one-way ANOVA indicated a statistically significant difference ($P < 0.001$) among ten species, and the Holm-Sidak's comparison test indicated the statistical difference between two species as follows: human versus avian, human versus equine, swine versus equine, swine versus avian, avian versus equine, human versus unknown, swine versus unknown, environment versus equine, human versus environment, swine versus environment, unknown versus equine, tiger versus equine, civet versus equine, cat versus equine, civet versus mink, swine versus mink, human versus mink, and swine versus canine.

During the one-way ANOVA test, a particular phenomenon got our attention, i.e. the residual was very large in standard ANOVA table. For example, the sum of squares (SS) was 668.97 and 6293.13 for between groups and residual under HA subtype (**Table 1**).

Table 1 suggested that there were very large variations in PA proteins within each subtype or species, which further suggested that the model II ANOVA was in need to determine the inter- and intra-subtype/species variations.

Table 2 listed the inter- and intra-subtype/species variations. The model II ANOVA defined the total variation as 100%, which was further divided into inter- and intra-subtype/species variations. As seen in **Table 2**, the intra-subtype/species variation is far much larger than the inter-subtype/species variation. For example, the inter-subtype HA variation was 10.71% while the intra-subtype HA variation was 89.28%.

Table 1. Standard ANOVA table regarding HA subtype, NA subtype and species of PA proteins from influenza A viruses.

	Source of variation	Degree of freedom	Sum of Squares	Mean Square	F
HA subtype	Between groups	16	668.97	41.81	16.05
	Residual	2415	6293.13	2.61	
	Total	2431	6962.10		
NA subtype	Between groups	9	377.13	41.90	15.41
	Residual	2422	6584.97	2.72	
	Total	2431	6962.10		
Species	Between groups	11	547.64	49.79	18.78
	Residual	2420	6414.46	2.65	
	Total	2431	6962.10		

Table 2. Inter- and intra-subtype/species variations of PA proteins from influenza A viruses.

Classification	Inter-subtype/ species variation	Intra-subtype/ species variation
HA subtype	10.71%	89.28%
NA subtype	7.54%	92.46%
Species	11.88%	88.12%

At this point, one might wonder why the statistical difference was found among subtypes and species while there were so large variations within subtype and species. These results in fact were very reasonable. In plain words, there would be statistical difference between males and females in performing a sport, for example, however the difference between male sportsman and ordinary male would be also huge, thus it could be possible this variation would be larger than that between males and females.

In fact, the single classification model II ANOVA has many important applications although this method is less familiar with most researchers [58,59]. For example, it is better to know the inter- and intra-patient variations before planning clinical experiments, say, if an experimental design should include two parallel groups (inter- patients) or a two-part crossover design (intra-patients).

In the context of this study, generally, a small intra-subtype/species variation suggested a cost-effective way in collecting of samples, it said, not many samples for a particular subtype/species were in need, by clear contrast, many samples were in need regarding a particular subtype/species if there was a large intra- subtype/species variation.

Actually, the inter- and intra-subtype/species variations were the mutations occurred in the same subtype or species, and occurred cross subtypes or species. There was a wide variety of patterns of antigenic variation across space and time, and within and between subtypes as well as hosts and we did not yet understand the determinants of these different patterns [60]. Our analysis could shed lights on this issue.

The far much large intra-subtype/species variation found in this study suggested: 1) much more PA proteins belonging to the same subtype/species were needed in order to better understand the mutation pattern in the same subtype/species, and 2) the current classification was based on the surface proteins from influenza A virus, while under the same subtype, the PA mutations were quite large.

On the other hand, the statistically significant difference between subtypes suggested the current classification valid even for the PA, which was an internal protein. The most important requirement for producing vaccines against viruses displaying antigenic diversity is a method of measuring antigenic distances between strains and developing an understanding of how these distances relate to cross-protection [61]. The current results supported the idea to develop vaccines and anti-flu drugs that generate effective heterosubtypic immunity based on immune recognition of influenza A virus antigens conserved across all viral strains [62,63].

4. ACKNOWLEDGEMENTS

This study was partly supported by International Science & Technology Cooperation Projects (2008DFA30710), Guangxi Science Foundation (No. 0630003A2 and 0991080), and Guangxi Academy of Sciences (project No. 09YJ17 SW07).

REFERENCES

[1] I. Capuaa and D. J. Alexander, (2008) Avian influenza vaccines and vaccination in birds, Vaccine, **26(4)**, D70−D73.

[2] N. Hehme, T. Colegate, B Palache, and L. Hessel, (2008) Influenza vaccine supply: Building long-term sustainability, Vaccine, **26(4)**, D23−D26.

[3] M. Hoelscher, S. Gangappa, W. Zhong, L. Jayashankar, and S. Sambhara, (2008) Vaccines against epidemic and pandemic influenza, Expert Opin. Drug Deliv., **5**, 1139 −1157.

[4] B. Palache, (2008) New vaccine approaches for seasonal and pandemic influenza, Vaccine, **26**, 6232−6236.

[5] J. C. Tilburt, P. S. Mueller, A. L. Ottenberg, G. A. Poland, and B. A. Kioenig, (2008) Facing the challenges of influenza in healthcare settings: The ethical rationale for mandatory seasonal influenza vaccination and its implications for future pandemics, Vaccine, **26(4)**, D27−D30.

[6] M. Peyre, G. Fusheng, S. Desvaux, and F. Roger, (2009) Avian influenza vaccines: A practical review in relation to their application in the field with a focus on the Asian experience, Epidemiol. Infect., **137**, 1−21.

[7] A. W. Hampson, (2008) Vaccines for pandemic influenza: The history of our current vaccines, their limitations and the requirements to deal with a pandemic threat, Ann. Acad. Med. Singapore, **37**, 510−517.

[8] N. Skeik and F. I. Jabr, (2008) Influenza viruses and the evolution of avian influenza virus H5N1, Int. J. Infect. Dis., **12**, 233−238.

[9] D. Q. Wei, Q. S. Du, H. Sun, and K. C. Chou, (2006) Insights from modeling the 3D structure of H5N1 influenza virus neuraminidase and its binding interactions with ligands, Biochem. Biophys. Res. Commun., **344**, 1048−1055.

[10] S. Q. Wang, Q. S. Du, and K. C. Chou, (2007) Study of drug resistance of chicken influenza A virus (H5N1) from homology-modeled 3D structures of neuraminidases, Biochem. Biophys. Res. Commun., **354**, 634−640.

[11] Q. S. Du, S. Q. Wang, and K. C. Chou, (2007) Analogue inhibitors by modifying oseltamivir based on the crystal neuraminidase structure for treating drug-resistant H5N1 virus, Biochem. Biophys. Res. Commun., **362**, 525−531.

[12] X. L. Guo, L. Li, D. Q. Wei, Y. S. Zhu, and K. C. Chou,

(2008) Cleavage mechanism of the H5N1 hemagglutinin by trypsin and furin. Amino Acids, **35**, 375−382.

[13] R. B. Huang, Q. S. Du, C. H. Wang, and K. C. Chou, (2008) An in-depth analysis of the biological functional studies based on the NMR M2 channel structure of influenza A virus, Biochem. Biophys. Res. Comm., **377**, 1243−1247.

[14] Q. S. Du, R. B. Huang, C. H. Wang, X. M. Li, and K. C. Chou, (2009) Energetic analysis of the two controversial drug binding sites of the M2 proton channel in influenza A virus, J. Theoret. Biol., doi:10.1016/j.jtbi.2009.1003. 1003.

[15] J. R. Schnell, and J. J. Chou, (2008) Structure and mechanism of the M2 proton channel of influenza A virus, Nature, **451**, 591−595.

[16] R. M. Pielak, J. R. Jason, R. Schnell, and J. J. Chou, (2009) Mechanism of drug inhibition and drug resistance of influenza A M2 channel, Proc. Natl. Acad. Sci. USA, www. pnas.org cgi doi 10.1073 pnas.0902548106.

[17] K. C. Chou, (2001) Prediction of protein cellular attributes using pseudo amino acid composition, PROTEINS: Structure, Function, and Genetics (Erratum: ibid., 2001, Vol.44, 60), **43**, 246−255.

[18] K. C. Chou, (2005) Using amphiphilic pseudo amino acid composition to predict enzyme subfamily classes, Bioinformatics, **21**, 10−19.

[19] X. Xiao, S. H. Shao, Z. D. Huang, and K. C. Chou, (2006) Using pseudo amino acid composition to predict protein structural classes: Approached with complexity measure factor, J. Comput. Chem., **27**, 478−482.

[20] X. Xiao, S. Shao, Y. Ding, Z. Huang, Y. Huang, and K. C. Chou, (2005) Using complexity measure factor to predict protein subcellular location, Amino Acids, **28**, 57−61.

[21] X. Xiao and K. C. Chou, (2007) Digital coding of amino acids based on hydrophobic index, Protein Pept. Lett., **14**, 871−875.

[22] X. Xiao, W. Z. Lin, and K. C. Chou, (2008) Using grey dynamic modeling and pseudo amino acid composition to predict protein structural classes, J. Comput. Chem., **29**, 2018−2024.

[23] X. Xiao, P. Wang, and K. C. Chou, (2008) Predicting protein structural classes with pseudo amino acid composition: An approach using geometric moments of cellular automaton image, J. Theoret. Biol., **254**, 691−696.

[24] X. Xiao, P. Wang, and K. C. Chou, (2008) GPCR-CA: A cellular automaton image approach for predicting G- protein-coupled receptor functional classes, J. Comput. Chem., DOI 10.1002/jcc.21163.

[25] X. Xiao, P. Wang, and K. C. Chou, (2009) Predicting protein quaternary structural attribute by hybridizing functional domain composition and pseudo amino acid composition, J. Appl. Crystallogr., **42**, 169−173.

[26] G. Wu and S. Yan, (2002) Randomness in the primary structure of protein: Methods and implications, Mol. Biol. Today, **3**, 55−69.

[27] G. Wu and S. Yan, (2006) Mutation trend of hemagglutinin of influenza A virus: a review from computational mutation viewpoint, Acta Pharmacol. Sin., **27**, 513−526.

[28] G. Wu and S. Yan, (2008) Lecture notes on computational mutation, Nova Science Publishers, New York.

[29] O. G. Engelhardt and E. Fodor, (2006) Functional association between viral and cellular transcription during influenza virus infection, Rev. Med. Virol., **16**, 329−345.

[30] A. Honda and A. Ishihama, (1997) The molecular anatomy of influenza virus RNA polymerase, Biol. Chem., **378**, 483−488.

[31] T. Watanabe, S. Watanabe, K. Shinya, J. H. Kim, M. Hatta, and Y. Kawaoka, (2009) Viral RNA polymerase complex promotes optimal growth of 1918 virus in the lower respiratory tract of ferrets, Proc. Natl. Acad. Sci. USA, **106**, 588−592.

[32] K. C. Chou and H. B. Shen, (2008) Cell-PLoc: A package of web-servers for predicting subcellular localization of proteins in various organisms, Nature Prot., **3**, 153−162.

[33] K. C. Chou and H. B. Shen, (2007) Review: Recent progresses in protein subcellular location prediction, Analyt. Biochem., **370**, 1−16.

[34] K. C. Chou and H. B. Shen, (2007) Euk-mPLoc: A fusion classifier for large-scale eukaryotic protein subcellular location prediction by incorporating multiple sites, J. Proteome Res., **6**, 1728−1734.

[35] H. B. Shen and K. C. Chou, (2009) QuatIdent: A web server for identifying protein quaternary structural attribute by fusing functional domain and sequential evolution information, J. Proteome Res., **8**, 1577−1584.

[36] K. C. Chou and H. B. Shen, (2007) MemType-2L: A Web server for predicting membrane proteins and their types by incorporating evolution information through Pse-PSSM, Biochem. Biophys. Res. Commun., **360**, 339−345.

[37] T. Wang, J. Yang, H. B. Shen, and K. C. Chou, (2008) Predicting membrane protein types by the LLDA algorithm, Protein Pept. Lett., **15**, 915−921.

[38] H. B. Shen and K. C. Chou. (2007) EzyPred: A top-down approach for predicting enzyme functional classes and subclasses, Biochem. Biophys. Res. Commun., 364, 53−59.

[39] K. C. Chou and D. W. Elrod, (2002) Bioinformatical analysis of G-protein-coupled receptors, J. Proteome Res., **1**, 429−433.

[40] K. C. Chou, (2005) Prediction of G-protein-coupled receptor classes, J. Proteome Res., **4**, 1413−1418.

[41] K. C. Chou and H. B. Shen, (2008) ProtIdent: A web server for identifying proteases and their types by fusing functional domain and sequential evolution information, Biochem. Biophys, Res. Comm., **376**, 321−325.

[42] H. B. Shen and K. C. Chou. (2009) Identification of proteases and their types, Analyt. Biochem., **385**, 153−160.

[43] K. C. Chou, (1993) A vectorized sequence-coupling model for predicting HIV protease cleavage sites in proteins, J. Biol. Chem., **268**, 16938−16948.

[44] K. C. Chou, (1996) Review: Prediction of HIV protease cleavage sites in proteins, Analyt. Biochem., **233**, 1−14.

[45] H. B. Shen and K. C. Chou, (2008) HIVcleave: a web-server for predicting HIV protease cleavage sites in proteins, Analyt. Biochem., **375**, 388−390.

[46] K. C. Chou and H. B. Shen, (2007) Signal-CF: A subsite-coupled and window-fusing approach for predicting signal peptides, Biochem. Biophys. Res. Commun., **357**, 633−640.

[47] H. B. Shen and K. C. Chou, (2007) Signal-3L: A 3-layer approach for predicting signal peptide, Biochem. Biophys. Res. Commun., **363**, 297−303.
[48] K. C. Chou, (2004) Review: Structure bioinformatics and its impact to biomedical science, Curr. Med. Chem., **11**, 2105−2134.
[49] R. Apweiler, A. Bairoch and C. H. Wu. (2005) Protein sequence databases, Curr. Opin. Chem. Biol., **8**, 76−80.
[50] G. Wu and S. Yan, (2008) Prediction of mutations engineered by randomness in H5N1 neuraminidases from influenza A virus, Amino Acids, **34**, 81−90.
[51] G. Wu and S. Yan, (2008) Prediction of mutations initiated by internal power in H3N2 hemagglutinins of influenza A virus from North America, Int. J. Pept. Res. Ther., **14**, 41−51.
[52] G. Wu and S. Yan, (2008) Prediction of mutation in H3N2 hemagglutinins of influenza A virus from North America based on different datasets, Protein Pept. Lett., **15**, 144−152.
[53] G. Wu and S. Yan, (2008) Three sampling strategies to predict mutations in H5N1 hemagglutinins from influenza A virus, Protein Pept. Lett., **15**, 731−738.
[54] G. Wu and S. Yan. (2008) Prediction of mutations engineered by randomness in H5N1 hemagglutinins of influenza A virus, Amino Acids, **35**, 365−373.
[55] E. Spackman, (2008) A brief introduction to the avian influenza virus, Methods Mol. Biol., **436**, 1−6.
[56] SPSS Inc. (1992-2003) SigmaStat for windows version 3.00.
[57] R. R. Sokal and F. J. Rohlf, (1995) Biometry: The principles and practices of statistics in biological research, 2nd ed, W. H. Freeman, New York, 203−218.
[58] G, Wu, M. Baraldo, and M. Furlanut, (1999) Inter-patient and intra-patient variations in the baseline tapping test in patients with Parkinson's disease, Acta Neurol. Belg., **99**, 182−184.
[59] M. Furlanut, G. Wu, and E. Perucca, (2001) Variability in the metabolism of levodopa and clinical implications, In: Interindividual Variability in Drug Metabolism in Man. eds. by Pacifici GM, Pelkonen O, Tayler & Francis, London and New York, Chapter 7, 181−227.
[60] M. Lipsitch and J. J. O'Hagan, (2007) Patterns of antigenic diversity and the mechanisms that maintain them, J. R. Soc. Interface, **4**, 787−802.
[61] J. A. Mumford, (2007) Vaccines and viral antigenic diversity, Rev. Sci. Tech., **26**, 69-90.
[62] F. Carrat and A. Flahault, (2007) Influenza vaccine: The challenge of antigenic drift, Vaccine, **25**, 6852−6862.
[63] K. M. Grebe, J. W. Yewdell, and J. R. Bennink, (2008) Heterosubtypic immunity to influenza A virus, where do we stand? Microbes. Infect., **10**, 1024−1029.

J. Biomedical Science and Engineering, 2009, 2, 280-286 **JBiSE**
doi: 10.4236/jbise.2009.24042 Published Online August 2009 (http://www.SciRP.org/journal/jbise/).

A hybrid wavelet and time plane based method for QT interval measurement in ECG signals

Swanirbhar Majumder[1], Saurabh Pal[2], Sidhartha Dhar[1], Abhijit Sinha[1], Abhijit Roy[1]

[1]Department of ECE, NERIST (Deemed University), Arunachal Pradesh, India; [2]Haldia Institute of Technology, Haldia, West Bengal, India.
Email: swanirbhar@gmail.com, spal76@gmail.com, siddhar2911@gmail.com, rush2abhi_ec@yahoo.com, c4abhi@yahoo.co.in

Received 29 March 2009; revised 25 April 2009; accepted 6 May 2009.

ABSTRACT

Here we present a method of QT interval measurement for Physionet's online QT Challenge ECG database using the combination of wavelet and time plane feature extraction mechanisms. For this we mainly combined two previous works one done using the Daubechies 6 wavelet and one time plane based with modifications in their algorithms and inclusion of two more wavelets (Daubechies 8 and Symlet 6). But found that out of these three wavelets Daubechies 6 and 8 gives the best output and when averaged with the interval of time plane feature extraction method it gives least percentage of error with respect to the median reference QT interval as specified by Physionet. Our modified time plane feature extraction scheme along with the wavelet method together produces best results for automated QT wave measurement as its regular verification is important for analyzing cardiac health. For the V2 chest lead particularly whose QT wave is of tremendous significance we have tested on 530 recordings of Physionet. This is because delay in cardiac repolarization causes ventricular tachyarrhythmias as well as Torsade de pointes (TdP). A feature of TdP is pronounced prolongation of the QT interval in the supraventricular beat preceding the arrhythmia. TdP can degenerate into ventricular fibrillation, leading to sudden death.

Keywords: ECG; QT; Physionet; TdP

1. INTRODUCTION

The QT interval is measured as the time interval between the onset of the QRS complex and the end of the T wave. At the end of the T wave repolarisation is completed and the T wave voltage amplitude returns to the baseline [1]. The QT interval is thus a measure of the duration of the ventricular depolarisation and repolarization. Some error may introduce in the QT interval measurement due to the fact that it may not return back to the base line or it may go below the base line along with the onset of U wave occasionally.

Many drugs prolong cardiac repolarization which in turn increases the QT interval. This might lead to ventricular arrhythmia as severe as torsade de pointes (TdP) in some critical cases [2,3]. Hence accurate measurement of the QT interval is very important for intensive cardiac care and also for pharmaceutical industry. A statistically significant increase in the mean QT interval (corrected for heart rate) as small as 6 milliseconds between baseline and maximal drug effect may be important as a signal of repolarization abnormality [4]. QT intervals can be detected manually, but these are not so accurate as well as not repeatable in general. Still we compare our results with the 'gold standard' reference QT measurements taken from the Physionet challenge 2006 because these were very precisely taken to build the database for the challenge so that the participants could compare their algorithms with the manual methods. Rather automatic QT interval measurement techniques are more accurate and reproducible, except for the experience of the physician/doctor giving some extra suggestions which may be beneficial in some particular special cases on neglecting the time factor [5,6]. Moreover if a bit of adaptiveness can be added to it via trained neural network it might be a great effort. Many researchers have performed several fundamental works on determination of QT interval along with other characteristic waves. Yan Sun *et al*. have proposed a multiscale morphological derivative (MMD) transform-based singularity detector for the detection of fiducial points in ECG signal, where these points are related to the characteristic waves such as the QRS complex, P wave and T wave [7]. Laguna P, Jane R, Caminal P have developed a method where the intervals of clinical importance can be detected by a multilead QRS detector that locates each beat, using a differentiated and low-pass filtered ECG signal as input and the waveform boundaries are located in each lead.

Later in their wavelet based method of QT interval measurement Mahmoodabadi *et al.* [8] evaluated the MIT-BIH database using the multiresolution wavelet for the modified lead II (MLII) and found that Daubechies 6 works the best. Here a slightly modified wavelet algorithm was applied on the V2 chest lead specifically, for 530 recording of the Physionet database using wavelets daubechies 6 and 8 as well as symlet 6. The choices of these wavelets were based on a huge amount of trial and error carried out on the group of inbuilt wavelets present under MATLAB® and comparing their mean square error with those of 'gold standard'. Later we found that Daubechies 6 gives the least error of the three and for the time plane features we found that using our modified time plane feature detection [9] method we have approximately similar percentage of error as the Daubechies 6 but in the opposite direction. So averaging both of these methods and combining we have less than 1% error in total while for the case of individual data the error percentage is within +10% to -7% from the adjusted reference herewith.

2. WAVELET FEATURE EXTRACTION

The flowchart for the wavelet analysis is shown in **Figure 1**. Here, we have used the technique devised by Mahmoodabadi *et al.* [8], for the automated feature extraction of the ECG Signals using Wavelet Domain. The algorithms are applied directly at one run over the whole digitized ECG signal which are saved as .mat files provided by Physionet as in **Figure 2**.

There are actually four separate algorithms, each of which is designated to extract certain features of the ECG signal. The description of the ECG feature extraction algorithm is shown in the **Figure 2**. First, the peak of the QRS complex with its high dominated amplitude in the signal is detected. Then Q and S waves are detected. The Zero voltage level of the signal is found next. The last step includes the calculation of the onset and offset of the P wave.

Peak of the R waves in signals from the lead have the largest amplitudes among other leads. In order to detect the peaks, specific details of the signal were selected. Details D3-D5 were kept and all the other details were removed. This procedure removes low frequencies and high frequencies. The attained signal samples were then squared. High amplitude transitions of the signal were then more noticeable, even if R peaks are deformed.

Then a practically lower limit is applied on the signal to remove unrelated noisy peaks. Because no subsequent beats happen less than 25 second, pseudo-beats are also removed. Detection of R peaks is very important because they define the cardiac beats and the exactness of all forthcoming detections is dependent on this.

Q and S peaks occur about the R peak with in 0.1 second. In order to make the peaks noticeable, all the details of the signal were removed up to detail D5. The approximation signal remained, was searched for extremum points about the R peaks formerly detected. The left point denoted the Q peak and the right one denotes the S peak. A normal QRS complex indicates that the electrical impulse has progressed normally from the bundle of His to the Purkinje network through the right and left bundle branches and that normal depolarization of the right and left ventricles has occurred.

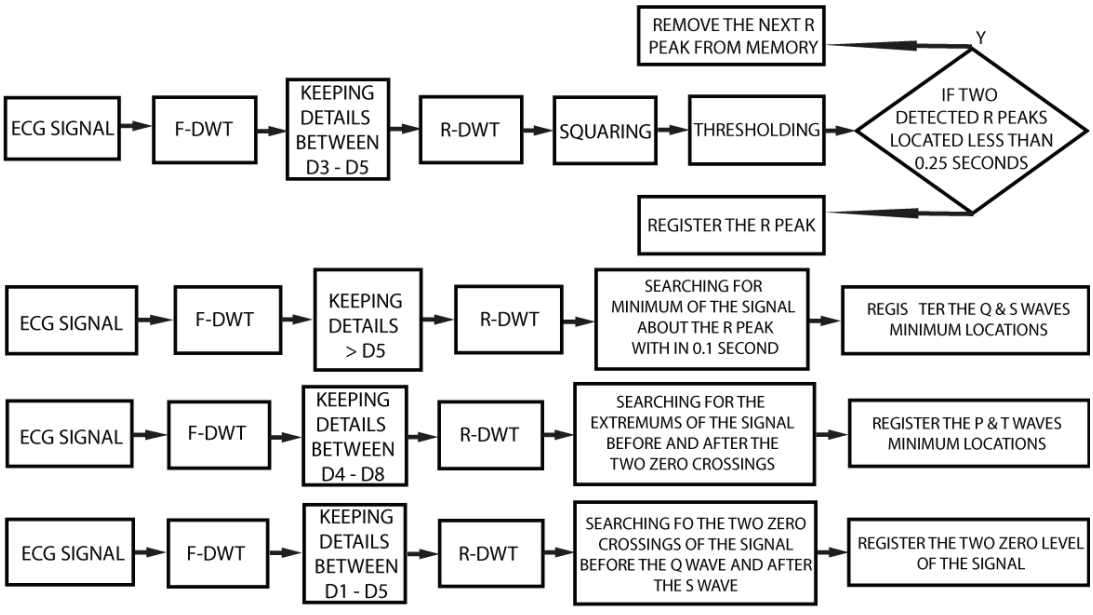

Figure 1. Wavelet feature extraction method.

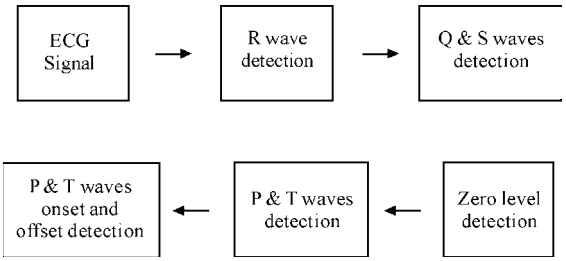

Figure 2. ECG feature extraction algorithm.

Although one might think that the electrocardiograph machines for recording electrocardiograms could determine when no current is flowing around the heart. However, many stray currents exist in the body, such as currents resulting from skin potentials and from differences in ionic concentrations in different parts of the body. These stray currents make it impossible for one to predetermine the exact zero reference level in the electrocardiogram. At the end of the QRS complex, no current is flowing around the heart. Even the current of injury disappears at this point and the potential of the electrocardiogram at this instant is zero.

This point is known as the J point. Most people, however, are conditioned to consider the TP segment of the electrocardiogram as the reference level rather than the J point which is much easier to be found correctly. By experiment we found that the voltage at this level is closely equal to the zero crossing of the approximation signal, keeping details D1-D5, before the Q peak. There is another zero crossing after the S peak. Comparing these two points is essential for detecting current of injury and ST segment shift.

These waves are more noticeable when keeping details D4-D8. At these levels, lower frequencies and high frequency ripples of the signal are removed. The extremes of the signal before and after the zero crossings about each R peak which are formerly detected denote P and T peaks. Zero crossings of the signal about the P and T peaks which were detected are the onset and offset points of the waves, respectively.

3. TIME PLANE FEATURE EXTRACTION

The flowchart for the time plane analysis is shown below. Here, we have used the techniques devised by Mitra M, Pal S and Majumder S [2], for the automated feature extraction of the ECG Signals using time domain analysis after some amount of modification in their algorithm which was not robust. The algorithms are applied directly at one run over the whole digitized ECG signal which are saved as. mat files provided by Physionet. Like the Wavelet Analysis here also we have four different steps for the different features for extraction. The flow diagrams of the steps are given in **Figure 3**. So we take one feature at a time to go for the extraction.

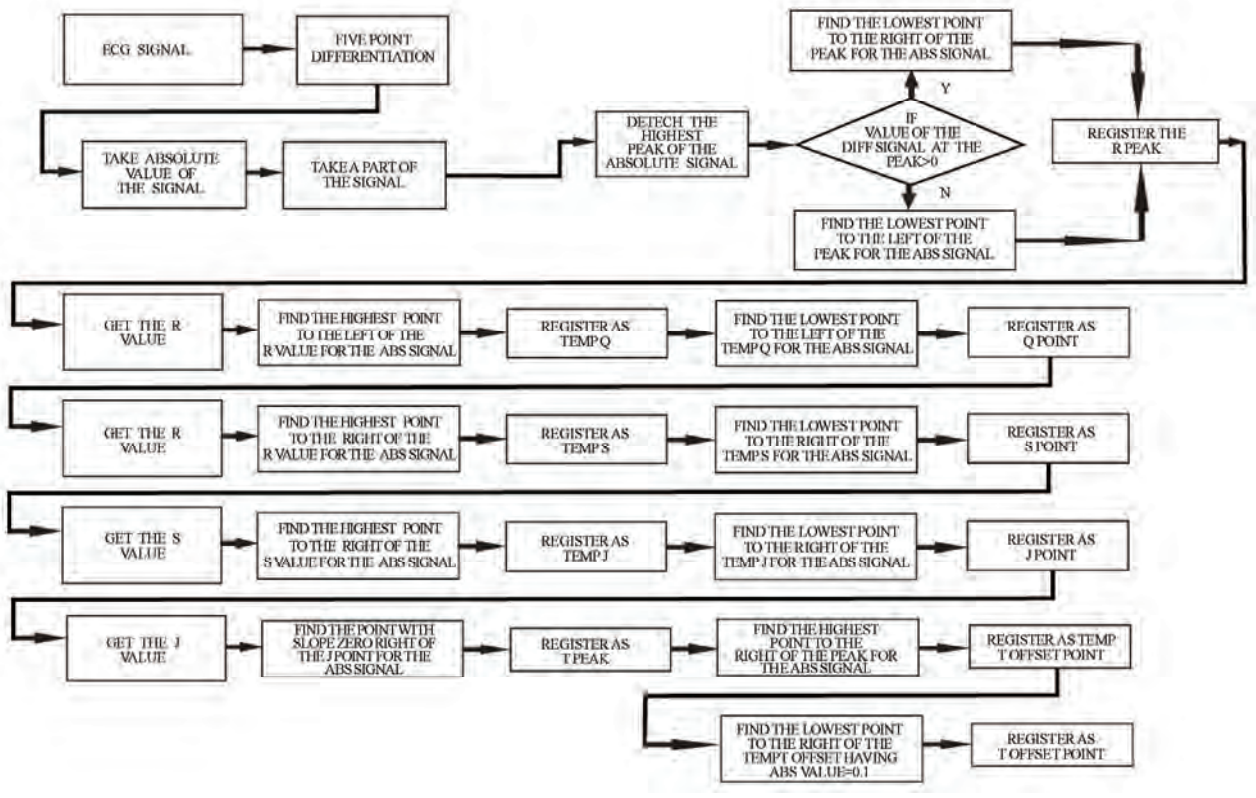

Figure 3. Time plane based feature extraction method.

The R wave detection step is the first and the most important step of the entire analysis procedure. First from the many R peaks available one in the middle has to be detected. For this a part of the absolute differentiated wave [12,13] is taken and the maximum point in that interval is calculated using the MATLAB® sorting. Here for differentiation we use the fivepoint differentiation equation given in Equation (1). The interval should be chosen such that it is smaller than the value of the RR interval. The corresponding value of the differentiated wave at this point is calculated and a conditional loop is initiated to find out whether it is negative or positive. This step is the very important as the rest of the analysis depends on it. Depending upon what the value comes out to be, the lowest point to the left or to the right of the peak is calculated. This point is the R point.

$$f'(x) \approx \frac{-f(x+2h)+8f(x+h)-8f(x-h)+f(x-2h)}{12h} \quad (1)$$

Then we go for the detection of the Q point. The proper detection of the R peak above step is very important here. After getting the R peak point, the highest point to the left of the R value in the absolute differentiated wave is found out. This point is stored in the memory as the temporary Q point. From this point as a reference the lowest point to the left of this point is again calculated. This point is the Q point.

For the detection of the S point on the wave the procedure is the same as that for the Q wave detection. Here too the proper detection of the R peak is very important. After getting the R peak point, the highest point to the right of the R value in the absolute differentiated wave is found out. This point is stored in the memory as temporary S point. From this point as a reference the lowest point to the right of this point is again calculated. This point is the S point.

The final step is the detection of the T wave peak and the T wave offset points. For this step to be successful, the correct S point detection is a must. Taking the S point detected above, the highest point on the differentiated wave to the right of the signal is calculated. This point is marked as the T wave peak point. To get the point of T peak offset, the value of the differentiated wave at each point to the right of the T peak point is found out and that point where the value becomes less than 0.1 is taken as the T peak offset point.

4. SIMULATION OF THE METHODS

Both the methods of wavelet and time plane based were programmatically linked with a GUI (**Figure 4**) where

Figure 4. Graphical User Interface (GUI).

for wavelet analysis we can select the wavelet and then get the values of the intervals of RR and QT.

Later using Eqs. (2) and (3) get QTc from QT interval and the heart rate from RR interval. Here firstly the "Load Data" button presents the user with a dialog to select the appropriate signal from the database. The "Clear Data" Button clears the cache after the execution of the program is complete. After the data is loaded the control can be passed to either the Wavelet or the Time Analysis. The Wavelet part contains additional buttons for selecting the different wavelet families "db6" for Daubechies 6, "db8" for Daubechies 8 and "sym6" for Symlet 6. Pressing any one of them starts the analysis procedure and after the completion of the analysis the original waveform is displayed.

To get the value of the QT Interval the button "QT Interval" is pressed. The QT waveform is displayed and the value of the interval is made available at the corresponding text box. The "QTc Interval" button displays the value of the modified QT according to the regression based approach.

The exact method which has been implemented here is that developed by Sagie *et al*., [14] as given in Eq. (2) below.

$$QTc = QT + 0.154(1 - RR) \quad (2)$$

The RR Interval which is important in the sense that it defines the cardiac beat cycle can be obtained by pressing the "RR Interval" button on the GUI which displays the R to R waveform. Along with that the value of the interval is displayed in the corresponding text box of wavelet based or time plane based side as per the technique selected. To get the heart rate of the patient the button "Heart Rate" is pressed and the calculated value of the heart rate of the patient is displayed in the corresponding text box using Eq. (3) [15] below.

$$Heart\ Rate = \frac{60}{\sqrt{RR}} \quad (3)$$

The final button is the "Full Wave Graph" display button. This button displays the entire ECG wave over a full cardiac cycle.

5. RESULTS ANALYSIS

Of the huge amount of database (530 recordings) analyzed for result part we hereby provide only the details of 24 patients selected arbitrarily as providing whole data set will cover up a huge amount of article area. Here our primary motive is to first select the wavelet family which we would be using for the wavelet analysis so based on **Table 1**. Here we have the QT

Table 1. QT interval for the different Patients.

SL	Physionet Patient ID	Adjusted QT Ref. (in secs)	Wavelet based QT detected (in secs)			TIME based QT (in secs)
			DB6	DB8	SYM6	
1	s0500_re	0.3971	0.3390	0.3400	0.3360	0.4430
2	s0499_re	0.3438	0.3470	0.3270	0.3370	0.3430
3	s0497_re	0.3993	0.3730	0.3560	0.3650	0.3440
4	s0496_re	0.3460	0.3080	0.2920	0.3020	0.3790
5	s0491_re	0.3840	0.3490	0.3400	0.3180	0.4190
6	s0487_re	0.4018	0.3820	0.3310	0.3450	0.4120
7	s0486_re	0.3645	0.3270	0.3310	0.3450	0.4110
8	s0481_re	0.3735	0.3450	0.3580	0.3370	0.4370
9	s0480_re	0.3714	0.3260	0.3160	0.3150	0.3910
10	s0479_re	0.3809	0.3770	0.3720	0.3670	0.4180
11	s0474_re	0.3528	0.3420	0.3470	0.3270	0.3960
12	s0473_re	0.3439	0.3120	0.3210	0.3040	0.4000
13	s0472_re	0.3137	0.3260	0.3110	0.3190	0.3480
14	s0471_re	0.3563	0.3190	0.3140	0.3370	0.4120
15	s0468_re	0.3507	0.3430	0.3520	0.3310	0.3380
16	s0467_re	0.3429	0.3190	0.3360	0.3300	0.3930
17	s0466_re	0.3587	0.3310	0.3270	0.3240	0.4070
18	s0465_re	0.3785	0.3270	0.3070	0.3180	0.4080
19	s0464_re	0.4098	0.3360	0.3420	0.3550	0.4040
20	s0463_re	0.4109	0.3810	0.3420	0.3530	0.4280
21	s0462_re	0.4022	0.3460	0.3430	0.3610	0.4330
22	s0461_re	0.3753	0.3130	0.3280	0.3450	0.4210
23	s0460_re	0.4243	0.3300	0.3740	0.3740	0.4270
24	s0452_re	0.4249	0.3860	0.4250	0.1090	0.4430

interval for 24 patients as detected by the three wavelets and the time plane. As per error calculations we found that the average error with respect to the adjusted reference [11] we have for “db6” 8.8%, “db8” 9.51%, for “sym6” 12.23% and for “time” -7.43% as per the data of 24 patients given in **Table 1** while for the whole set of 530 patients we have for “db6”, “db8”, “sym6” and “time” error percentages 8.7483%, 8.9034%, 10.7794% and -7.157% respectively. Thus among the wavelet family “db6” gives least error strengthening findings of Mahmoodabadi *et al* along with it is “db8” but inspite of the nearby percentage of error as its type 6 variant still the fluctuations are more in this case as it can be viewed from the graphical representation. But the main important part of the analysis of **Table 1** is that the time plane error and db6/db8 error complement each other very well so we average them and use the value.

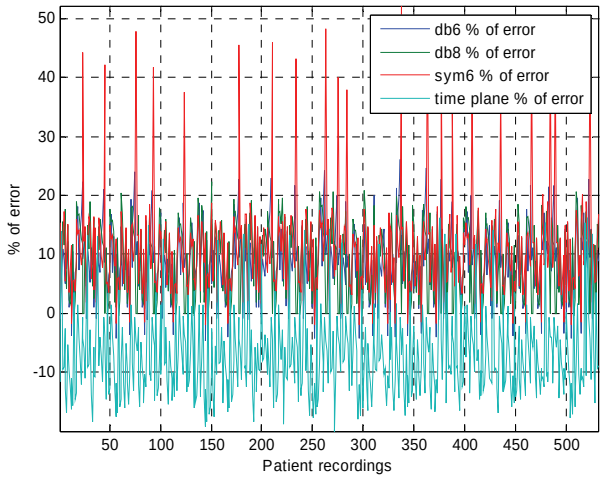

Figure 5. QT interval Percentage of error for the different techniques employed.

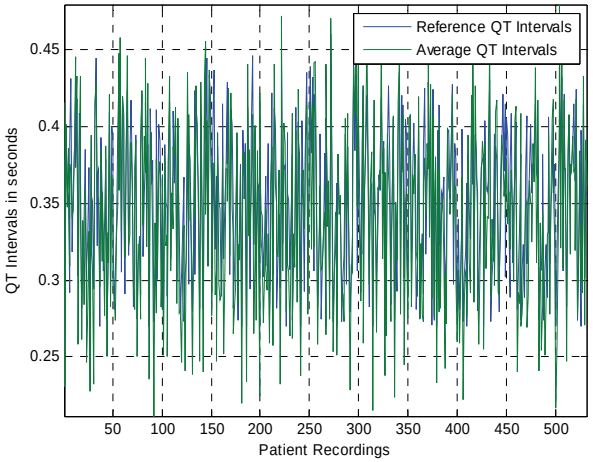

Figure 6. Reference QT interval and averaged QT interval of wavelet (db6) and time plane method.

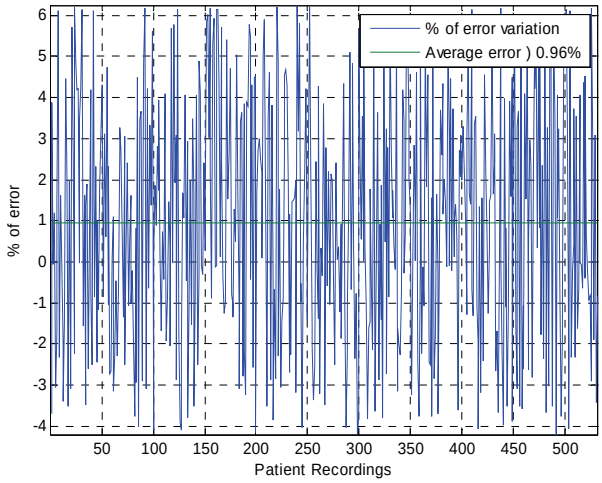

Figure 7. Percentage of error variation for the averaged Time and Wavelet based methods.

The error percentages for extended set of 530 readings similar to the 24 data as in **Table 1** are plotted in **Figure 5**. When we plot the averaged time and wavelet (db6) based QT intervals with the adjusted reference as in **Figure 6** we see that we are having about 0.96% of average error in total with variation from 6.2487% to -4.2% for the given data but except for some skewed cases it lies within ±5% for the whole data analyzed.

But on taking the whole data into account we have total average error as only 0.72%. The percentage of error variation for the averaged wavelet and time plane based QT interval data and total average of 0.96% are shown in **Figure 7**.

The Daubechies 8 “db8” based results were also good but not as good as Daubechies 6 “db6” while the sym6 results were up to the mark except for some special cases where the Symlet “sym6” regularly gave some fluctuations when compared with the measured values. Thus as it can be seen from the **Figure 5** we have some high peaks (30-50%) errors in case of Symlet “sym6”.

6. CONCLUSIONS

In this paper, therefore proves that Daubechies 6 is the best wavelet for wavelet based QT interval detection supporting Mahmoodabadi *et al*. and the clubbing together of a novel time plane based method [9] along with the wavelet based method [8] has hereby produced considerably better results compared to the wavelet and time plane based method when used separately. Moreover this is an extension of our work [16] where we have increased the data set on which the algorithm has been tested.

REFERENCES

[1] A. J. Moss, *et al*., (2001) ISHNE guidelines for electrocardiographic evaluation of drug-related QT prolongation and other alterations in ventricular repolarisation: Task force summary, Ann Noninvasive Electrocardiol.

[2] R. J. Myerburg, *et al.*, (2001) Cardiac arrest and sudden death, In: Peter Libby., editor. Braunwald's Heart Disease: A Textbook of Cardiovascular Disease. 6. Saunders (W. B.) Co Ltd, 899−900.

[3] Haverkamp *et al*., (2000) The potential for QT prolongation and proarrhythmia by non-antiarrhythmic drugs: Clinical and regulatory implications, European Heart Journal.

[4] C. M. Pratt, *et al.*, (1996) Dose response relation between terfenidine and the QTc interval on the scalar electrocardiogram: Distinguishing a drug effect from spontaneous variability, American Heart Journal.

[5] I. Salvelieva, *et al.*, (1998) Agreement and reproducibility of automatic versus manual measurement of QT interval and QT dispersion, Ame J Cardiol., **81**, 471−477.

[6] J. Kautzner, *et al*., (1994) Short and long-term reproducibility of QT, QTc and QT dispersion measurements in healthy subjects, PACE Pacing and Clinical Electrophysiology, **17**, 928−940.

[7] Y. Sun, *et al*, Characteristic wave detection in ECG signal using morphological transform, BMC Cardiovascular Disorder, **5**, 2005.

[8] Mahmoodabadi, *et al*., ECG feature extraction using Daubechies wavelets, Proceedings of fifth IASTED International Conference on Visualization, Imaging and Image Processing, Spain.

[9] M. Mitra *et al*, ECG signal processing for analysis of abnormalities based on QT interval-A novel approach, Proceedings of AMSE International Conference on Modeling and Simulation MS'07, Kolkata, India, 216−218.

[10] S. Majumder, *et al* Wavelet and time plane based feature extraction of ECG signal, *Proceedings* of National Conference on Communication & Networking (NCCN'08) Punjab, India, 99−103.

[11] Reference txt, (2006) Reference QT interval measurements used as the basis for calculating final scores in the PhysioNet/Computers in Cardiology Challenge, http://www.physionet.org.

[12] P. Laguna *et al.*, (1994) Automatic detection of wave boundaries in multilead ECG signals: validation with the CSE database, Comput Biomed Res, Feb, **27(1)**, 45−60.

[13] F. B. Hilderbrand, Introduction to numerical analysis, TMH edn, 82−84.

[14] A. Sagie, *et al*., An improved method for adjusting the QT interval for heart rate (the Framingham Heart Study), Am J Cardiol, **70 (7)**.

[15] G. S. Wagner, Marriott's Practical ECG, 10th Edition, Copyright ©2001 Lippincott Williams & Wilkins.

[16] (2008) A hybrid wavelet and time plane based method for QT interval measurement in ECG dignals, 9th International Conference on Signal Processing, Publication Date: 26−29 Oct., 2120−2123, Location: Beijing, China, ISBN: 978-1-4244-2178-7, DOI: 10.1109/ICSP.4697564.

Call for Papers

The 4th International Conference on Bioinformatics and Biomedical Engineering (iCBBE 2010)

June 18-20, 2010 Chengdu, China

The 4th International Conference on Bioinformatics and Biomedical Engineering (iCBBE 2010) will be held from June 18th to 20th, 2010 in Chengdu, China. You are welcome to share your recent advances and achievements in all aspects of bioinformatics and biomedical engineering on the conference. **And all accepted papers in iCBBE 2010 will be published by IEEE and indexed by Ei Compendex and ISTP.**

Topics

Bioinformatics and Computational Biology

- Protein structure, function and sequence analysis
- Protein interactions, docking and function
- Computational proteomics
- DNA and RNA structure, function and sequence analysis
- Gene regulation, expression, identification and network
- Structural, functional and comparative genomics
- Computer aided drug design
- Data acquisition, analysis and visualization
- Algorithms, software, and tools in Bioinformatics
- Any novel approaches to bioinformatics problems

Biomedical Engineering

- Biomedical imaging, image processing & visualization
- Bioelectrical and neural engineering
- Biomechanics and bio-transport
- Methods and biology effects of NMR/CT/ECG technology
- Biomedical devices, sensors and artificial organs
- Biochemical, cellular, molecular and tissue engineering
- Biomedical robotics and mechanics
- Rehabilitation engineering and clinical engineering
- Health monitoring systems and wearable system
- Bio-signal processing and analysis
- Biometric and bio-measurement
- Biomaterial and biomedical optics
- Other topics related to biomedical engineering

Special Sessions

Biomedical imaging
Biostatistics and biometry
The information technology in bioinformatics
Environmental pollution & public health

Sponsors

IEEE Eng. in Medicine and Biology Society, USA
Gordon Life Science Institute, USA
University of Lowa, USA
Wuhan University, China
Sichuan University, China
Journal of Biomedical Science and Engineering, USA

Important Dates

Paper Due: Oct.30, 2009
Acceptance Notification: Dec.31, 2009
Conference: June 18-20, 2010

Contact Information

Website:http://www.icbbe.org/2010/
E-mail: submit@icbbe.org

Call for Papers

Journal of Biomedical Science and Engineering (JBiSE)

www. scirp. org/journal/jbise

JBiSE, an international journal, publishes research and review articles in all important aspects of biology, medicine, engineering, and their intersection. Both experimental and theoretical papers are acceptable provided they report important findings, novel insights, or useful techniques in these areas. All manuscripts must be prepared in English, and are subject to a rigorous and fair peer-review process. Accepted papers will immediately appear online followed by printed in hard copy.

Subject Coverage

Bioelectrical and neural engineering

Bioinformatics

Medical applications of computer modeling

Biomedical modeling

Biomedical image processing & visualization

Real-time health monitoring systems

Biomechanics and bio-transport

Patten recognition and medical diagnosis

Biomedical effects of electromagnetic radiation

Safety of wireless communication devices

Biomedical devices, sensors, and nano technologies

NMR/CT/ECG technologies and EM field simulation

Physiological signal processing

Medical data mining

Other related topics

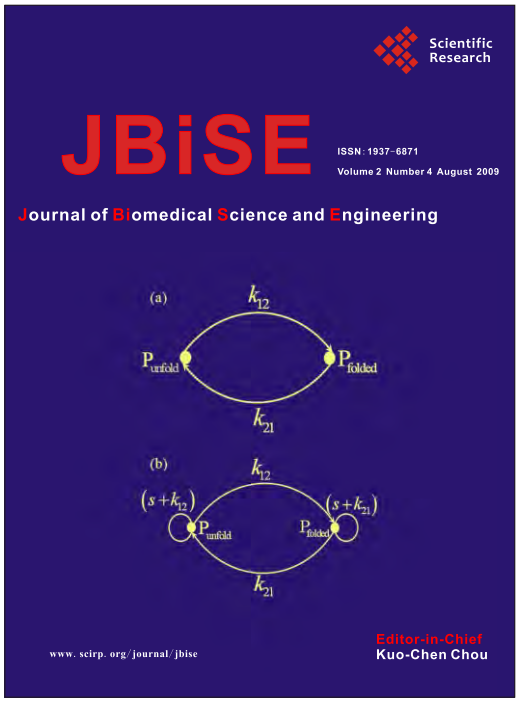

Editor–in–Chief

Editorial Board

Notes for Intending Authors

Submitted papers should not have been previously published nor be currently under consideration for publication elsewhere. Paper submission will be handled electronically through the website. All papers are refereed through a peer review process. For more details about the submissions, please access the website.

Website and E-Mail

www. scirp. org/journal/jbise

Email: jbise@scirp.org

ISSN 1937-6871 (Print), 1937-688X (Online)

Journal of Biomedical Science and Engineering, 2009, 2.
Published Online August 2009 in SciRes (http://www.scirp.org/journal/jbise).

TABLE OF CONTENTS

Volume 2, Number 4, August 2009

977193768700107